PONTIFÍCIA UNIVERSIDADE CATÓLICA
DO RIO DE JANEIRO

Annita da Costa Fidalgo

Modelling of TiO$_2$ properties for the band gap prediction using Artificial Neural Networks

Dissertação de Mestrado

Thesis presented to the Programa de Pós–graduação em Engenharia de Materiais e de Processos Químicos e Metalúrgicos, do Departamento de Engenharia Química e de Materiais da PUC-Rio in partial fulfillment of the requirements for the degree of Mestre em Engenharia de Materiais e de Processos Químicos e Metalúrgicos.

Advisor   : Prof. Brunno Ferreira dos Santos
Co-advisor: Prof. Sonia Letichevsky

Rio de Janeiro
April 2020

Annita da Costa Fidalgo

Modelling of TiO$_2$ properties for the band gap prediction using Artificial Neural Networks

Thesis presented to the Programa de Pós–graduação em Engenharia de Materiais e de Processos Químicos e Metalúrgicos da PUC-Rio in partial fulfillment of the requirements for the degree of Mestre em Engenharia de Materiais e de Processos Químicos e Metalúrgicos. Approved by the Examination Committee:

Prof. Brunno Ferreira dos Santos
Advisor
Departamento de Engenharia Química e de Materiais – PUC-Rio

Prof. Sonia Letichevsky
Co-advisor
Departamento de Engenharia Química e de Materiais – PUC-Rio

Dr. Maurício Bezerra de Souza Junior
UFRJ

Prof. Roberto Ribeiro de Avillez
Departamento de Engenharia Química e de Materiais – PUC-Rio

Rio de Janeiro, April the 29th, 2020

Annita da Costa Fidalgo

Bachelor's degree in **Materials and Nanotechnology Engineering** at Pontifical Catholic University of Rio de Janeiro (Rio de Janeiro, Brazil).

Ficha Catalográfica

Acknowledgments

The financial supports of Coordination for the Improvement of Higher Education Personnel (Capes) and National Council for Scientific and Technological Development (CNPq) are truly appreciated.

I also wish to express my sincere appreciation to my beloved Carlos Mesquita for all emotional support.

To my all LaMAC co-workers, specially Professor Amanda Lemette, Artur Serpa, Caio Grossi, Isabelle Valim and my brother João Neto for all day by day support and coffee moments.

To Professors Roberto de Avillez and Eduardo Brocchi, who have encouraged me to do the Master's degree and have always been willing to support me.

To my family that made me flourish.

To my friends Richard Magalhães and Fernanda Gonçalves for all help.

The last, but not the least, my advisor Brunno Santos, for all trust, support, patience and expertise. And to my co-advisor Sonia Letichevsky for all assistance, chiefly in the most critical moment of this path. They have my eternal gratitude.

Abstract

Fidalgo, Annita; Ferreira dos Santos, Brunno; Letichevsky, Sonia. **Modelling of TiO$_2$ properties for the band gap prediction using Artificial Neural Networks**. Rio de Janeiro, 2020. 122p. Masters Dissertation – Department of Chemical and Materials Engineering, Pontifical Catholic University of Rio de Janeiro.

Titanium dioxide has been widely applied by industry and scientific research as a photocatalyst, whose main drawback still has been the application under visible light. Properties such as phases amount, crystallite size, specific surface area, pore volume, and band gap value (Eg) have been explored by synthesis methods to improve TiO$_2$'s performance. However, they are empirically adjusted. The present work was carried out to describe an analytical relation between those properties for photocatalysis, using Artificial Neural Networks (ANNs) as a statistical tool. Aiming the most representative set, 53 literature papers were used for the database. Eg was considered the measurement which evaluates the photocatalytic performance, namely the network's output variable. Two blocks A and B, which are distinguished by input variables, were arranged into groups to investigate the variables pair influences, using 257 and 220 photocatalysts vectors for each, respectively. Modelling attempts examined different training algorithms (based on Backpropagation), types of networks (Feedforward, Cascade forward and Elman), transfer functions, number of hidden neurons, and multilayer network. The developed models were evaluated by the sum of squared error (SSE), the correlation coefficient (R^2) of regression for both training and test data, the prediction behaviour of the dataset, and the regression diagram of predicted and observed values. The block A results suggest the variables do not have an apparent relationship. Multilayers models on block B revealed an increase of network identification performance. The result with the highest coefficient showed 4-4-6-1 topology; corresponding, respectively, to input, first hidden, second hidden and output layers. It had R^2 of 84 % for training and to 50 % for test, with SSE of 2.24. This result suggests this network is not able to predict the Eg, but it can be improved. The structural properties should be reviewed, according to standards of characterization and statistical data. Hence, the model could be well fitted, optimized, and used for photocatalysis improvement.

Keywords

Resumo

Fidalgo, Annita; Ferreira dos Santos, Brunno (Orientador); Letichevsky, Sonia (Co-Advisor). **Modelagem das propriedades do TiO₂ na previsão do band gap utilizando Redes Neurais Artificiais**. Rio de Janeiro, 2020. 122p. Dissertação de mestrado – Departamento de Engenharia Química e de Materiais, Pontifícia Universidade Católica do Rio de Janeiro.

O dióxido de titânio é amplamente utilizado pela indústria e pesquisa como fotocatalisador, cuja principal desvantagem ainda é sua aplicação sob luz visível. Propriedades como quantidade de fases, tamanho do cristalito, área de superfície específica, volume de poros e valor da banda proibida (Eg) são explorados por métodos de síntese para aprimorar a performance do TiO₂. No entanto, elas são ajustadas empiracamente. O presente trabalho foi realizado a fim de descrever uma relação analítica entre essas propriedades para a fotocatálise, usando Redes Neurais Artificiais (RNAs) como ferramente estatística. A fim de ter o banco de dados mais representativo, foram usados 53 artigos. O Eg foi considerado a medida a qual avalia a performance fotocatalítica, sendo o parâmetro de saída da rede. Dois blocos A e B, distintos pelas variáveis de entrada, foram arranjados em grupos para investigar a influência das variáveis em pares, com 257 e 220 fotocatalisadores para cada, respectivamente. Exploraram-se diferentes algoritmos de treinamento (baseados em Retropropagação), tipos de redes (Feedforward, Cascade forward e Elman), funções de transferência, número de neurônios e rede multicamadas. Avaliaram-se os modelos pela Soma dos Erros Quadráticos (SSE), pelo coeficiente de correlação de regressão (R^2) tanto para o treinamento e quanto para o teste, pelo comportamento de predição do banco de dados e pelo diagrama de regressão dos valores preditos pelos observados. Os resultados do bloco A sugerem que as variáveis não aparentam ter uma relação. Os modelos de múltiplas camadas no bloco B revelaram um aumento no desempenho. O resultado de maior coeficiente teve topologia de 4-4-6-1, correspondendo a camada de entrada, primeira camada oculta, segunda camada oculta e camda de saída, respectivamente. Obteve-se R^2 de 84 % para o treinamento e 50 % para o teste, com SSE de 2.24. Esse resultado sugere que a rede não é capaz de prever o Eg, mas ela pode ser aprimorada. Os parâmetros estruturais devem ser revisados, de acordo com padrões de caracterizações e dados estatísticos. Consequentemente, o modelo pode ser bem ajustado, otimizado e usado na melhoria da fotocatálise.

Palavras-chave

Dióxido de titânio;   Fotocatalisador;   Retropropagação Feedforward; Retropropagação Cascade forward;   Retropropagação Elman.

Summary

List of figures

List of tables

Nomenclature

e^- Electron

E_F Energy of Fermi level

h^+ Hole

%A   Percentage of anatase phase

%B   Percentage of brookite phase

%R   Percentage of rutile phase

α momentum term

TiO_2 Titanium dioxide

η learning rate

λ Wavelength

Alg.   Training algorithm

ANN   Artificial Neural Network

c   Speed of light in a vacuum inertial frame

CB   Conduction Band

CF   Cascade Backpropagation Network

CP   Band gap correspondent phase

dA   Crystallite size of anatase phase in nanometers

dB   Crystallite size of brookite phase in nanometers

dP   Pore diameter in nanometers

dR   Crystallite size of rutile phase in nanometers

DRS   Diffuse Reflection Spectroscopy technique

Eg   Band gap value in electronvolt

ELM   Elman Backpropagation Network

F1   Transfer function of the first hidden layer

F2   Transfer function of the second hidden layer

F3   Transfer function of the third hidden layer

FF   Feedforward Backpropagation Network

Fy   Transfer function of the output hidden layer

h   Planck constant

logsig Logistic sigmoidal function

N1   Number of neurons on the first hidden layer

N2   Number of neurons on the second hidden layer

N3   Number of neurons on the third hidden layer

purelin Linear function

R^2 correlation coefficients

Ref   Reference number

S   Specific surface area in m^2/g

SSE   Sum of Squared Error

tansig Hyperbolic tangent sigmoid function algorithm

trainbr Levenberg-Marquardt backpropagation with Bayesian Regularisation algorithm

traingdx Gradient descent backpropagation algorithm

trainlm Levenberg-Marquardt backpropagation algorithm

trainoss One-step secant backpropagation algorithm

TT   Transition type of Band gap

UV   Ultra Violet

VB   Valence Band

Vis   Visible

Vol   Pore volume in cm^3/g

XRD   X-Ray Diffraction technique

E agora, José?

Carlos Drummond de Andrade, *Poesias.*

1
Introduction

Titanium dioxide was the key for photocatalysis progress. The singularity of TiO_2 is due to its high stability, efficient photoactivity, low cost and huge potential for many applications [1, 2, 3, 4]. However, TiO_2 can only work under ultraviolet light, which is its main drawback.

The solar radiation is the most abundant light source [1, 5], of which photoreactions could be strongly benefit. The UV-light corresponds only of 5 % of that source, the visible light 43 % and the infrared 52 %. Therefore, the TiO_2 performance is very limited when solar radiation is applied.

Many strategies have been investigated to improve TiO_2 performance enabling it to work under visible light, such as heterojunction formation and metal dopping. The modifications are strongly explored on synthesis routes and they have been reported through the crystalline structure, surface area and band gap evaluation by literature. [5, 6]

The modifications are always carried out in order to get a better performance of the catalyst in the studied reaction. The performance can be assessed by the band gap measurement or an experimental process. For example, the hydrogen production rate or the concentration of dye removal. For optimization of catalytic tests, computational intelligence has been strongly applied [7, 8, 9, 10, 11].

Artificial Neural Networks (ANN) is a technique of computational intelligence for modelling. It works based on biological neurons, where an information is given, processed and concluded. Not only this information is passed forward but also the system learns from it, improving itself. Then, ANNs are used as a tool for prediction, identification and controlling. [12]

On Scopus platform, ANN has been used for chemical, process and materials engineer in addition to photocatalysis application since 2015. These studies are interconnected by their title, abstract or keywords, as shown on Figure 1.1. The focus is on catalysis keyword, with 14 keywords directly connected. The size of each circle corresponds to each influence (or strength) and each colour corresponds to each subject cluster found by the program. Thus, ANN studies are connect to titanium dioxide and photocatalysis, and all are from a different cluster of knowledge, symbolized by colours.

Figure 1.1: Articles from Scopus with keywords: ANN, Photocatalysis and Engineers - chemical, materials and process from 2015 to 2019 by VOSviewer 1.6.15.

ANN modelling has been well succeed for complex systems implementation. Besides that, each model is unique according to its application and its methodology development. [12, 13]

For instance in photocatalysis, Owolabi, T. et al. [14] used neural models to predict the band gap of doped titanium dioxide from crystal lattice distortion. This investigation helps to understand the mechanism, properties and their mathematical relationships.

The present work assessed TiO_2 properties contemplating Materials Science fundamentals in an emerging area of Computational tools. This study attempted to establish a unique model and it aimed the construction of a large database from literature, exploring different types of ANN.

This work is arranged in 8 chapters. The chapter 2 presents general and specific objectives. The next chapter is a literature review of TiO_2, characterization techniques and ANNs. Furthermore, there is presented a correlation with them and photocatalysis. The chapter 4 shows data acquisition and ANN development within the methodology. The next chapter presents and discusses the results. The chapter 6 is a conclusion of this study. The chapter 7 has suggestions for future research and the chapter 8 has supplementary information such as the code, additional data and weights and biases.

2
Objective

General objective   was to develop a model for prediction of the band gap as a direct variable of photocatalysis using data from the literature and analysing it carefully. Therefore, to be able to generalize predictions for different scenarios and estimate the effects of variables.

Specific objectives

- Use only TiO_2 photocatalysts;
- Build a large database, exploring and analysing literature reports;
- Nominate the most relevant characteristics studied, establishing the variables;
- Use ANN as a tool to obtain a relationship between titanium dioxide characteristics;
- Implement different types of ANN: Feedforward, Cascade forward and Elman Backpropagation;
- Develop and validate ANN models;
- Discuss its impact on photocatalysis.

3
Literature Review

This chapter reviews important subjects for the comprehension and discussion of this study. The following sections are the Titanium dioxide, Characterization techniques and Artificial Neural Network. In the end of each one, articles are compared with the present work goals.

3.1
Titanium dioxide

The titanium dioxide (TiO_2) assumes three stable crystalline structures, namely anatase, rutile, and brookite (Figure 3.1). The latter has an orthorhombic structure and the other two, tetragonal. The brookite phase is barely studied because it is metastable and because of its synthesis conditions. [15]

| 3.1(a): Anatase | 3.1(b): Rutile | 3.1(c): Brookite |
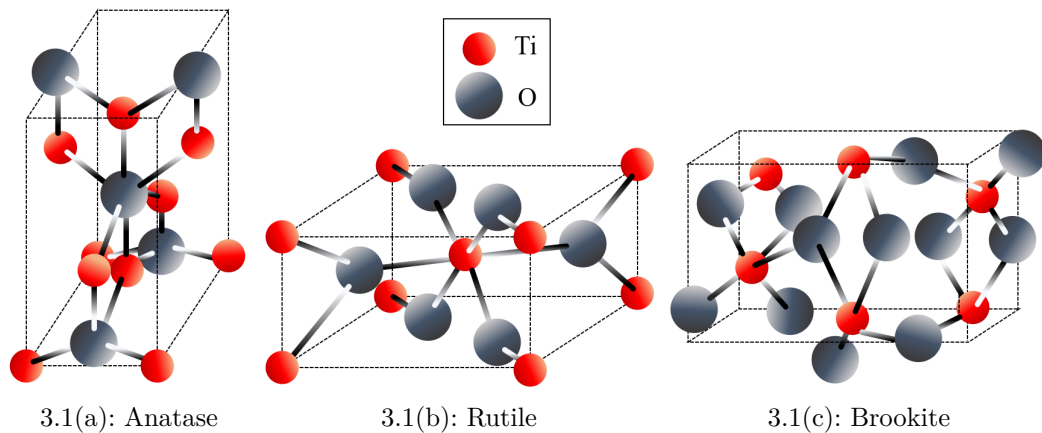
Figure 3.1: Illustration of crystalline structures of TiO_2. Adapted from Costa (2018).

The rutile is the stablest thermodynamic phase. However, for nanometric dimensions, the anatase is more propitious to occur according to its lower Surface Free Energy than rutile. Then, the anatase phase can be synthesized at low temperatures and have an irreversible phase transformation for rutile at high temperatures. [3, 16]

3.1.1
Band theory

The TiO_2 is heavily used as a photocatalyst because of its semiconductor properties, as a consequence of its band structure. When atoms or molecules make a chemical bond, their orbitals overlap, increasing its total energy. The energy is discrete due to its electronic structure, according to the Pauli exclusion principle. In a solid-state, where the crystalline system is a periodic lattice of a unit cell, the energy levels highly increase and get too nearer, assuming a block form called a band. [17, 18]

As a consequence of orbital and wave functions theory, there are at least two peaks (minimum and maximum) that are, for the band theory, namely Valence Band (VB), the occupied energy level, and Conduction Band (CB), the non occupied one. In addition, Homo is the highest occupied molecular orbital and Lumo, the lowest unoccupied molecular orbital. The energy difference between them is the band gap value (Eg). The Figure 3.2 exemplifies the band theory [17].

Semiconductors have narrow band gaps that include their thermodynamic equilibrium, or also known as the Fermi level (E_F) with zero energy. It is worth mentioning that it is a convention in physics for an atom resting in the infinite, without interaction. Hence, an electron (e^-) from VB is easily excited to CB, generating a hole (h^+) in its place, also known as pair electron-hole. Therefore, the energy difference is the band gap value. [17]
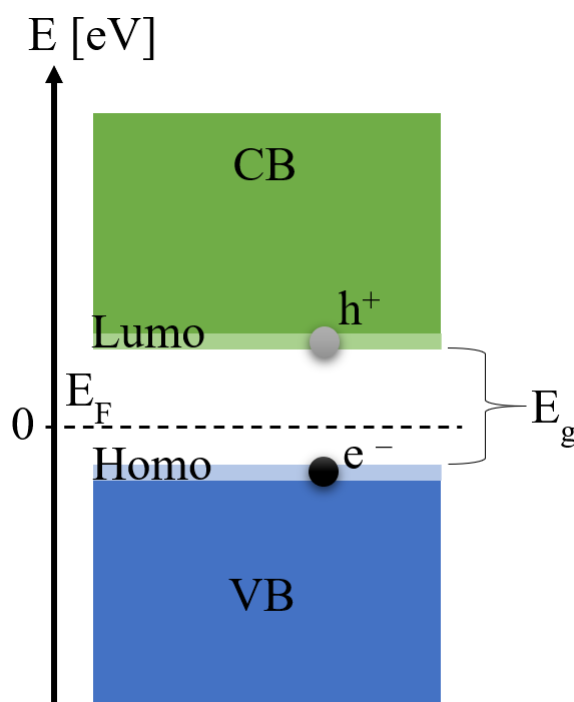
Figure 3.2: Illustration of Band theory. Adapted from Kittel (1976).

3.1.2
Photocatalysis

In photocatalysis, incident photon on the catalyst surface must an energy equal or larger than the catalyst band gap. As in catalysis, the pair electron-hole does not participate in the global reaction, but in the mechanism. Thus, each application, each photocatalyst, and each crystalline structure has a specific mechanism.

The TiO_2 phases have different band gap values. Anatase is reported to have 3.2 eV and Rutile 3.0 eV [5]. Moreover, they have different transitions types, that is how the pair electron-hole occurs. Whereas anatase has an indirect transition, rutile and brookite have a direct one. The transition type refers to the distance between the bands, considering the first Brillouin zone, that is, the first magnitude of reciprocal space [17]. If both Homo and Lumo are in the same wave vector, it is a direct transition. Otherwise, it is an indirect transition, because a phonon is also needed to preserve the conservation of momentum and energy (Figure 3.3). [17, 19]

3.3(a): Direct 3.3(b): Indirect
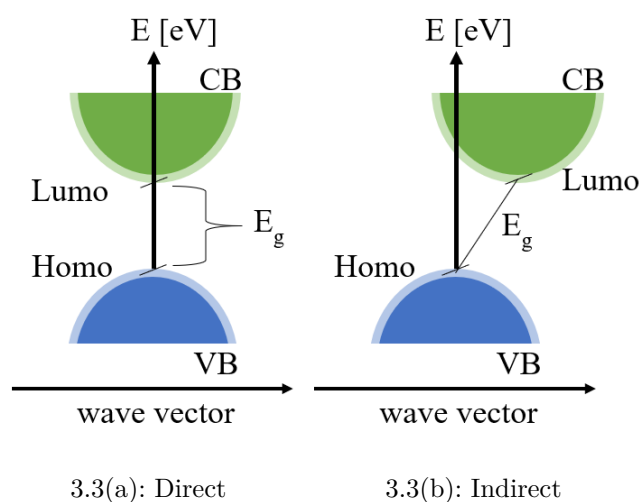
Figure 3.3: Illustration of transition types. Adapted from Kittel (1976).

The photon energy is classified according to the spectrum of the wavelength as ultra-violet (UV - until 400 nm), visible (Vis 400 - 750 nm) and infrared (over 750 nm). Despite the fact that TiO_2 can be observed in three different crystalline phases with its own band gaps, all of them work under UV light. This is a disadvantage for the photocatalyst performance because UV light is an expensive resource. Furthermore, there are more abundance light sources, that is, 95 % of solar spectrum is over UV-light wavelength range.

The band gap energy is one of the main characteristic of materials that have been explored for a higher photocatalytic performance [16, 20]. Then,

strategies have been explored, such as doping and heterojunction. In general, the improvement of photocatalysis can be splitted into the modification of photocatalysts and external conditions, according to Kou et al. 2017 [6]. Each system has a specific light source, temperature and chemical solution. On the other hand, the same photocatalyst can have different shape, band gap or surface effect.

For instance, a commercial TiO_2 widely employed, Evonik P25, is a mixture of anatase and rutile that ranges around 65-80:35-20 wt% [3, 21] for a better catalytic performance [22, 23]. Besides, it is a nanometric powder. However, neither the reason of its outstanding photocatalytic performance under UV light nor quantitative relation of this mixture is well known.

3.1.3
Applications

The TiO_2 applications are typically for hydrogen production [5, 24, 25, 26, 27, 28, 29, 30], decomposition of organic molecules [7, 8, 31, 32] and decomposition of pollution [5, 33, 34].

The photocatalytic water splitting (Figure 3.4) is a classical application scenario, where the mechanism is initialized with a photon incidence on TiO_2 surface, generating a pair electron-hole. It involves two major reactions of reduction–oxidation (redox), for water protonation and hydrogen formation. [4, 5]
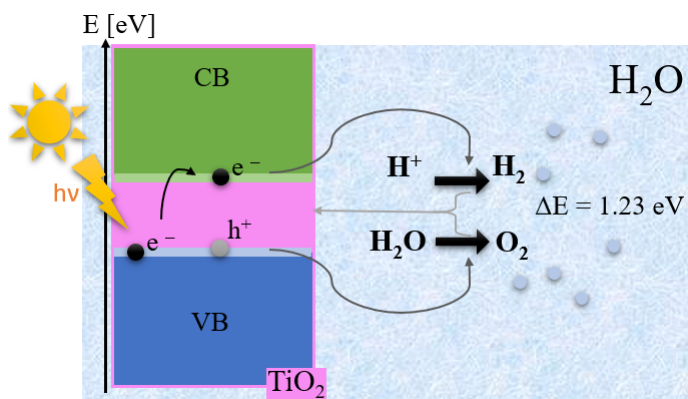
Figure 3.4: Illustration of water splitting mechanism. Adapted from Jafari (2016).

Considering the Pourbaix Diagram, the standard potential energy of redox is null for hydrogen formation and 1.23 V for oxygen formation from water (Equation 3-1). Thus, the minimum energy for photocatalysis is $\Delta E = 1.23$ eV. [5].

$$
\begin{array}{lll}
2H^+ + 2e^- \longrightarrow H_2 & E^0_{red} = 0 & V \\
H_2O + 2h^+ \longrightarrow 2H^+ + \frac{1}{2}O_2 & E^0_{ox} = -1.23 & V \\
\hline
H_2O \longrightarrow H_2 + \frac{1}{2}O_2 & \Delta E = 1.23 & eV
\end{array}
\tag{3-1}
$$
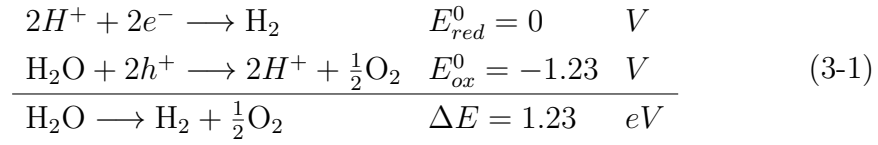
In the case of pollutant degradation, Carbajo et al. [34] explored the application of TiO_2 synthesized via sol-gel, carrying out to control the crystallite size and the phase transitions of anatase-rutile. The authors studied these properties because they affect the photocatalytic performance, which is the same consideration of this present work. They also suggested the photocatalytic performance description should use photocatalyst properties. Unlike most of the related literature, the results of Cabajo et al. [34] refuted the optimum point of anatase-rutile mixture, due to the highest photodegradation rate be a 100 % anatase sample in their studies. Besides the idea of having an optimized TiO_2 photocatalyst, they did not quantify the influences on the catalytic performance, that is, a mathematical relationship that explains the best (or worst) performance.

3.2
Characterization techniques

A few characterization techniques are here briefly reviewed, namely X-Ray Diffraction, UV-Vis Diffuse Reflectance Spectroscopy and Nitrogen Physisorption. They are commonly used in photocatalyst studies to measure the crystalline phases, the crystallite size, the specific surface area, the pore diameter, the pore volume and the band gap value.

3.2.1
X-Ray Diffraction

The X-Ray Diffraction (XRD) is the main technique for crystalline structure determination. It is based on the light scattering and interference. The Bragg's law determines the angles for a constructive interference of incident X-ray photons. The Equation 3-2 describes it, where $\mathbf{d}$ is the interplanar distance, θ is the angle of incidence, $\mathbf{n}$ is a positive integer and λ is the wavelength of the incident wave. Copper radiation is most frequently used and it has λ_{Cu} = 1.5418 Å.

$$2dsin\theta = n\lambda \tag{3-2}$$

Hence, materials and phases can be identified and quantitatively evaluated. For example, the mean crystallite size can be evaluated by either the Scherrer equation application to a single peak or from Rietveld refinement that fits all the peaks of the pattern and apply the full width at half maximum (FWHM – Scherrer equation) or Voigt Integral Breadth (LVolIB). [23, 35, 36].

3.2.2
UV-Vis Diffuse Reflectance Spectroscopy

The Diffuse Reflectance Spectroscopy (DRS) is a technique used for optical constants, thickness and transitions investigation. It is highly applied on semiconductors, especially for photocatalysis purpose. The band gap measurement is based on the reflection coefficient of the photocatalyst surface by an incident light, according to the scattering condition.

The qualitative evaluation of this technique requires mathematical methods that depends on sample preparation, such as, the particle size and sample packaging. For example, the Kubelka-Munk theory for the band gap calculation. It is obtained by the straight-line fit intersection of the respective reflectance function, considering the proper band gap transition, and the irradiation energy, according to Equation 3-3 where $\mathbf{R}$ is the diffuse reflectance, $\mathbf{S}$

the scattered light factor, ϵ the molar absorption coefficient and **C** the sample concentration. [16, 37, 38].

$$F(R) = \frac{(1-R)^2}{2R} = \frac{\epsilon C}{S} \tag{3-3}$$

Moreover, this theory has been improved. The Tauc plot method employs a modified Kubelka-Munk according to equation Equation 3-4. The modified function is obtained after applying an energy **hν** (Planck's constant and light frequency, respectively) according to an electronic transition **n**.

$$(F(R) \times h\nu)^{1/n} \tag{3-4}$$

Through the Kubelka-Munk plot $F(R) \times E$, the Tauc method estimates the band gap value and transition type according to Equation 3-5, where α is the extinction coefficient and **A** the absorption constant.

$$\alpha \times (h\nu) \approx A((h\nu) - E_g)^n \tag{3-5}$$

The transition type usually appears named as Kubelka-Munk modified for $F(R)^{1/n}$ and as Tauc Plot for $\alpha \times (h\nu)^{1/n}$. The value of **n** is 1/2 for a direct allowed transition, 2 for an indirect allowed, 3/2 for a direct forbidden and 3 for an indirect forbidden. [38]

Another approach is the direct use of radiation absorption. The straight-line fit intersection of absorbance coefficient and wavelength gives the band gap value, using the Planck–Einstein relation (equation 3-6 where E is the energy of a photon, h the Planck constant, ν the frequency, c the speed of light, λ the wavelength).

$$E = h\nu = h\frac{c}{\lambda} \tag{3-6}$$

All evaluations types may result in different band gap values, illustrated in Figure 3.5 for a generic material, adapted from TiO_2 measurements of López and Gómes, 2012 [38].
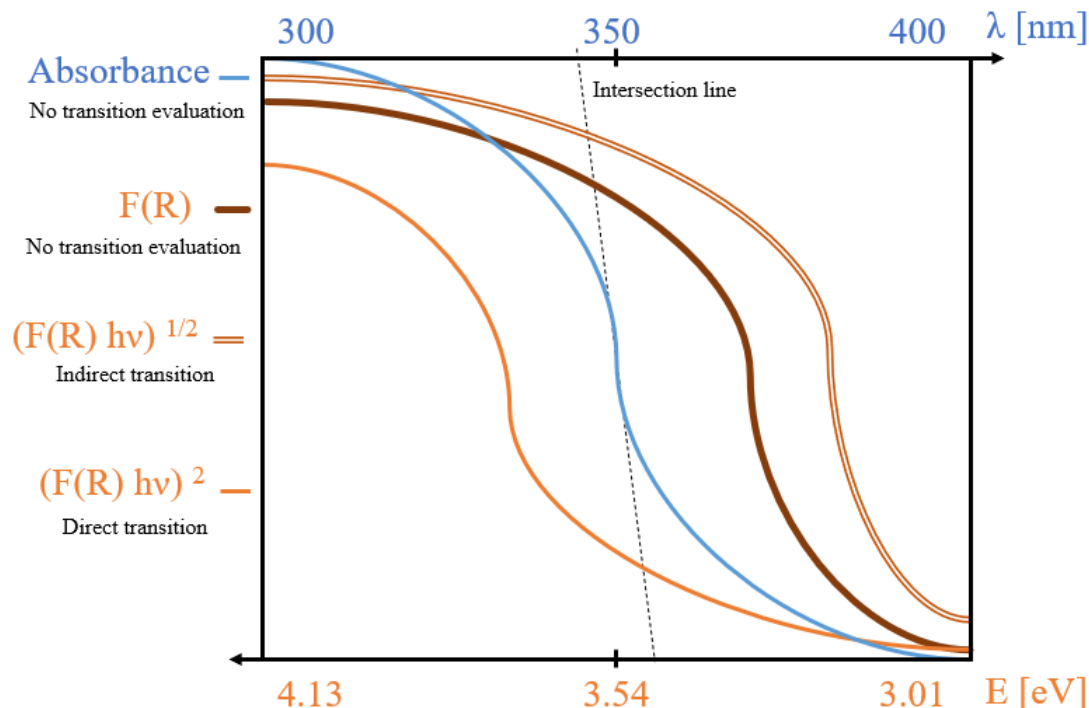
Figure 3.5: Exaggerated graphical representation of band gap measurements methods by DRS for a generic material. Adapted from López (2012).

3.2.3
Nitrogen Physisorption

The physical adsorption of nitrogen molecules on a solid surface is a technique used for surface evaluation, such as specific surface area and pore volume. The analysis usually uses the Brunauer–Emmett–Teller (BET) method, which is based on the relative pressure variation until gas saturation. [16]

3.2.4
Characterization in Photocatalysis

In Llorca et al. [30], the characterization was carried out to measure the crystalline structure, the dimensions of particle size, the surface area and the band gap of titania and the photocatalyst samples that used the titania as a support. This study applied Tauc plot in DRS technique. The characterization values supported analysis properties and enable the formulation of a trend for hydrogen production. According to them and their reaction conditions, the TiO_2 nanotubes had the best result for the non decorated sample pristine TiO_2, which showed better performance than the standard P25 sample.

3.3
Artificial Neural Networks

Artificial Neural Network (ANN) is a statistical method able to identify correlations between elements, usually applied in complex systems. It works based on biological neural circuit, which is an amount of neural interconnections that gives information through synapses. This cell structure has basically three main parts: the dendrite, which receives an information, the body, which process the information and the axon, which moves the information forward. Artificial neurons are similarly arranged in layers namely input (or also first layer), hidden and output, shown in Figure 3.6. [39, 13, 40, 41]
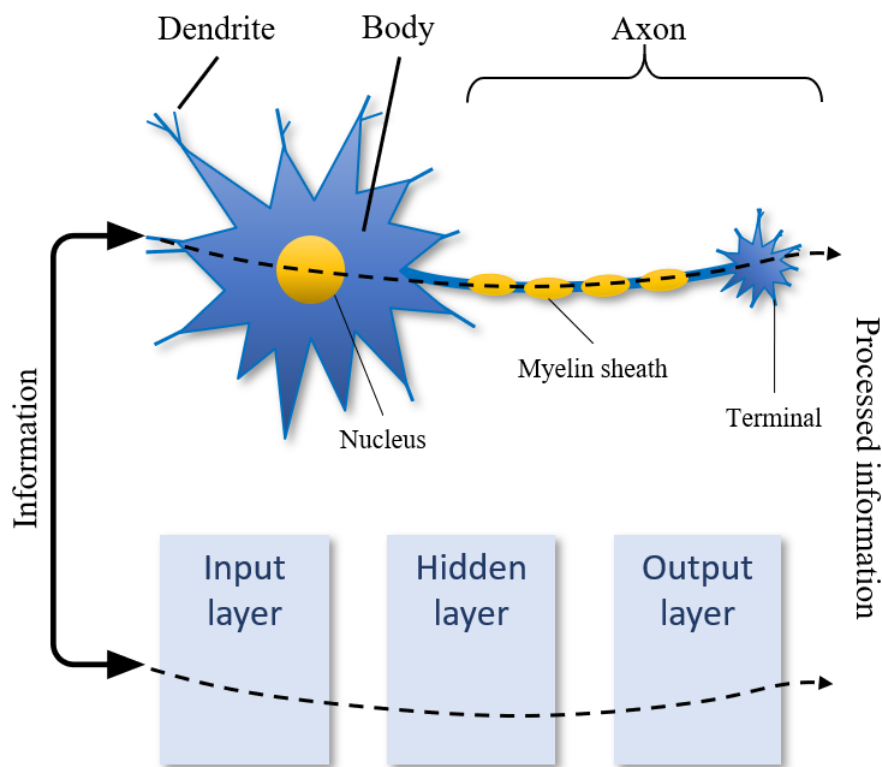
Figure 3.6: Comparison of biological and artificial neurons.

3.3.1
Neuron structure

A neuron is constituted by weights and biases, which measure the variable relevance and degree of freedom. A weight affects the information magnitude and the bias is a polarization term attached for each neuron. All information provided is rated by mathematical functions. On these terms, there are n inputs $\vec{x_n} = (x_1, x_2, ..., x_n)$, which have a respective **weight** $\vec{w_n} = (w_1, w_2, ..., w_n)$, that are activated by a transfer giving one output value $\hat{y}$, according to the decision equation that is the sum of input times weight plus **bias** (Equation 3-7). If

that sum is equal or greater than the neuron threshold (θ), the signal goes forward. After that, the ŷ could be used as output value for the output neuron or either as input for another hidden neuron. It is worth mentioning that the network can have several output vectors, here was considered one, just for the system simplicity. [13, 40, 42]

$$\sum_{i=1}^{n}(x_i.w_i) + b \geq \theta \qquad (3\text{-}7)$$

The connection of the neurons establishes the network. A simple ANN is represented on Figure 3.7, where n input values are connected to j neurons from a single layer. Each neuron has the influences of weights and bias, where the information given pass through a generic function limier. The output information from all neurons generates the single output value ŷ. This network only passes the information forward and it does not have a feedback from the output to the input, thus it is called as non recurrent network. [39, 40, 41, 42]
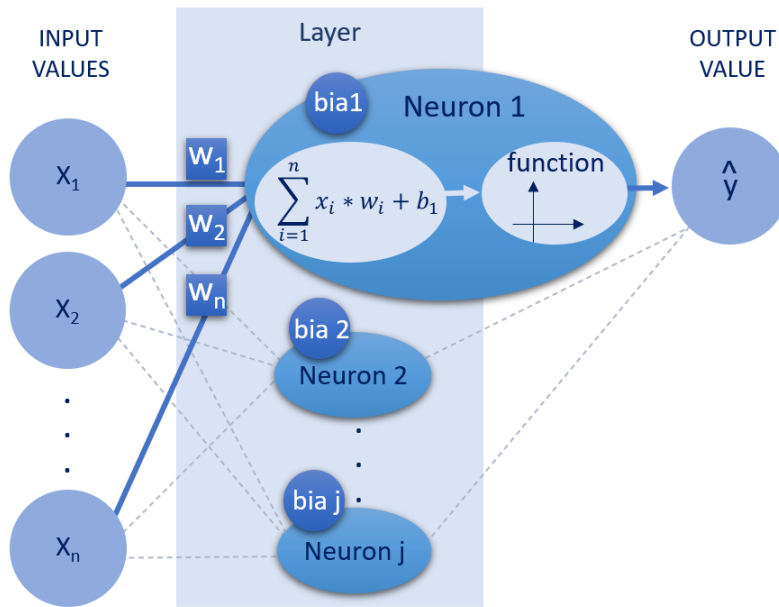
Figure 3.7: A generic feedforward network with a single layer.

The weights and biases values are provided and adjusted during the learning process, whose aim is to make the network able to reproduce a requested output group from a particular input group, for example for Classification. This is the training step that can be classified into supervised and non supervised. [13, 42]

3.3.2
Training categories

The supervised training has a value vector from the requested output group, that is, the output value is known. So, the network learning is developed based on minimization of the error from that observed value ($\mathbf{y}$) to that predicted value by the network ($\hat{\mathbf{y}}$), after the model be fed back by the inputs x_n information. The training data is used for the adjustment of weights and biases during the learning process and the test data for the network evaluation.

On the other hand, the non supervised training does not require the output information. Because this process is able to get statistical properties from the training dataset, classify them into similarity groups. Thus, that set must be sufficient to recognize a pattern and generate an output value. [42]

3.3.3
ANN architecture

The network architecture is as important as the learning process, because the quantity of hidden layers, types of networks, the quantity of neurons, transfer and activation functions are chosen for each problem.

3.3.3.1
Number of hidden layers

A hidden layer is the layer that is neither directly connected to input nor output. So, it can have a different amount of neurons. A multilayer ANN has more than one hidden layer. It is widely applied for recurrent networks for complex systems, allowing more synapses, that is, interconnections. However, having a more sophisticated process is not indicative of a good network. Figure 3.8 illustrates a multilayer ANN with two hidden layers, where each one has a different number of hidden neurons, $\mathbf{j}$ and $\mathbf{z}$ respectively.
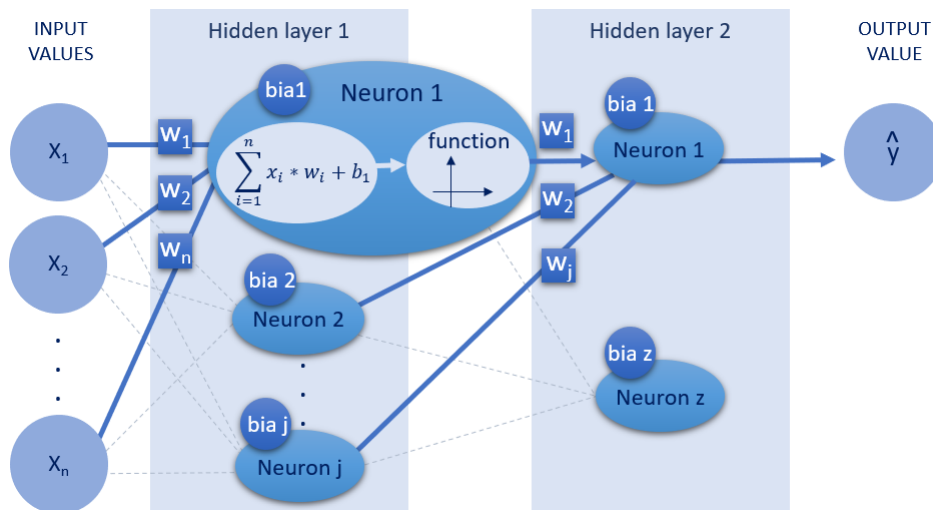
Figure 3.8: A generic feedforward network multilayer.

3.3.3.2
Number of hidden neurons

The number of neurons on the layers is a variable of the network development. For the input layer, the neurons are the input variables of the system and for the output layer, the output variable. On the other hand, the numbers of neurons on the hidden layers can be changed.

The number of hidden neurons must be at least the same of the input neurons in order to avoid underfitting error, which is a poor adjustment of the model. But it also must support the information given from the training dataset, avoid overfitting error that counts the residual variation. Thus, the number of the hidden neurons (**Na** where a is the correspondent hidden layer) is set for each problem.

3.3.3.3
ANN Types

The ANN can have different interconnections called ANN Types. The networks that process the information beyond a non-recurring basis are called Feedforward (FF). In another words, the first layer has the input data, which are the input neurons; the last layer gives the output data, and all hidden layers are fully connected. The FF is illustrated on Figure 3.9. [43]
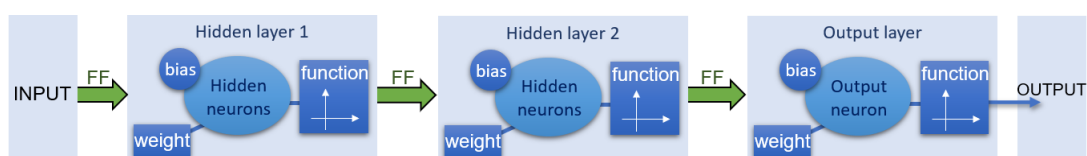
Figure 3.9: ANN FF with two hidden layers.

The mathematical equation of the FF architecture with one hidden layer, one output **y** and **n** input neurons **x** is shown on Equation 3-8:

$$y^{FF} = Fy(by + \sum_{k=1}^{j}(wy_k.F1(b1_k + \sum_{i=1}^{n} x_i.w1_{ki}))) \tag{3-8}$$

Where **Fy** is the output function; **F1** the transfer function; **w1** the weight from the input neuron **n** to the hidden neuron **k**; **wy** the weight from the hidden neuron **k** to the output neuron; **by** the bias of the output neuron and **b1** the bias of the hidden neuron **k**. [44]

Cascade-forward network (CF) is quite similar to FF, but it is a recurrent network, that is, it also includes a connection for all forward layers from previous layers, thus it explores more the sensibility of multilayers variables than FF. The CF is illustrated on Figure 3.10, where the input layer not only gives the information to the first hidden layer but also to all next layers, including the other hidden layer and the output layer. Each connection creates a weight in the layer. [43]
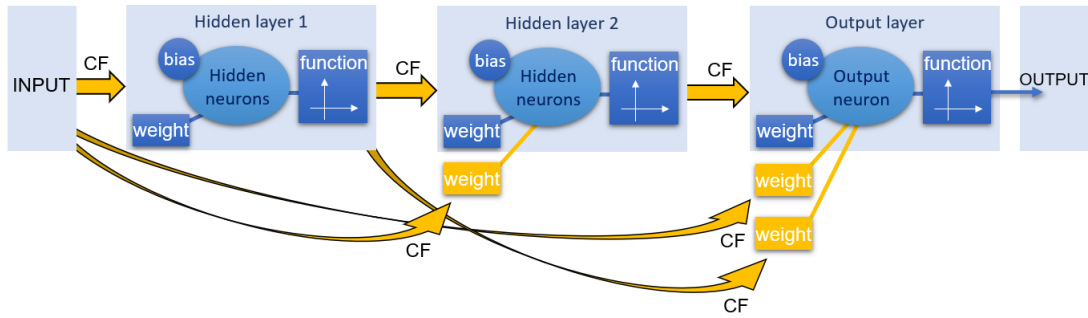
Figure 3.10: ANN CF with two hidden layers.

The mathematical equation of the architecture CF with one hidden layer, one output **y** and **n** input neurons **x** shown on Equation 3-9 has a different term added to the FF equation (Equation 3-10).

$$y^{CF} = (\sum_{i=1}^{n} F0.w0_i.x_i) + Fy(by + \sum_{k=1}^{j}(wy_k.F1(b1_k + \sum_{i=1}^{n} x_i.w1_{ki}))) \tag{3-9}$$

$$y^{CF} = \sum_{i=1}^{n} F0.w0_i.x_i + y^{FF} \tag{3-10}$$

Where **F0** is the transfer function from the input layer to the output and **w0** the feedback weight from the input neuron **i** to the output. [44]

The Elman network (ELM) is a dynamic and layer-recurrent network. It has also been explored for small nuances identification, because is a completely recurrent network. The ELM is illustrated on Figure 3.11, where each infor-

mation $\hat{\mathbf{y}}$ is feedback to the previous layers. Thus, the first hidden layer not only receives a weight from itself $\hat{\mathbf{y}}$, but also another from the second hidden layer. [43]
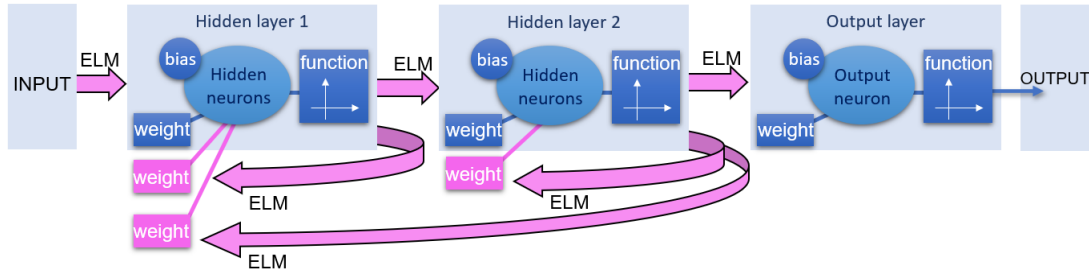
Figure 3.11: ANN ELM with two hidden layers.

The mathematical equation of the architecture ELM with one hidden layer, one output $\mathbf{y}$ and $\mathbf{n}$ input neurons $\mathbf{x}$ shown on Equation 3-11 demonstrates the aggregate complexity: a new term in the innermost sum.

$$y^{ELM} = Fy(by + \sum_{k=1}^{j}(wy_k.F1(b1_k + \sum_{i=1}^{n} x_i.(w1_{ki} + wa_{ki}))))) \tag{3-11}$$

Where $\mathbf{wa}$ is the feedback weight from the hidden neuron $\mathbf{k}$ to the input layer.

3.3.3.4
Backpropagation algorithm

The backpropagation algorithm is usually used for computing the loss function gradient in order to support a random learning process. It is based on the error minimization from the comparison of the squared difference between the predicted and observed variables from the network ($\mathbf{y}$ on Equation 3-12). [39, 40, 42, 43]

$$E_j[w] = \frac{(y_j^{observed} - \hat{y}_j^{predicted})^2}{2} \tag{3-12}$$

Where E[W] is the error of a neuron $\mathbf{j}$ with a set of weights $\mathbf{w}$.

The neurons are updated proportionally from the gradient of the error $E_j[w]$, due to the learning rate η (Equation 3-13).

$$\Delta w_{ij} = -\eta.\frac{\partial E[w]}{\partial w_{ij}} \tag{3-13}$$

Where the learning rate η is a constant between 0 and 1, $\mathbf{i}$ is the connection from the previous layer for the neuron $\mathbf{j}$ from the next layer.

As other gradient descent methods, it needs to calculate the derivative for all network layers. Then, the adjustment of weights can be rewritten as Equation 3-14. [13, 40]

$$\Delta w_{ij}^{t+1} = \eta s_i E_j + \alpha . w_{ij}^t \qquad (3\text{-}14)$$

Where Δw_{ij}^{t+1} and w_{ij}^t are the weight variation of neuron **j** to connection **i** at time **t+1** and **t** respectively, s_i is the input value of neuron **j** from connection **i** and α the momentum term.

The η and α are terms that have been explored for implementation. The learning rate influences on the convergence adjustment, because it directly changes the derivative of the minimization function. It varies between 0 and 1, and it should be as high as possible, preventing trapping on the local minimum, η near 0. But not too high, avoiding an oscillation around the global minimum, η near 1. The momentum term keeps previous information on the weights, which supports the non-oscillation on the global minimum. [13, 40]
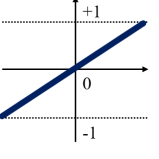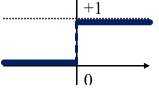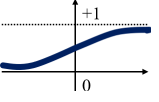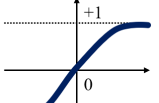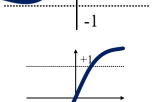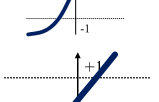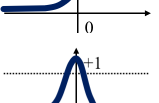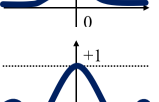
3.3.3.5
Transfer functions

The transfer functions (**Fa**, where a is the correspondent hidden layer) process the information given to a neuron from the weights and bias received. The function from the output layer is also called activation function (**Fy**). They can be differential equations for continuous systems or difference equations for discreet systems. [13]

The usual transfer functions used are listed on Table 3.1. There can also have a combination between them in each range of the domain.

Table 3.1: Transfer functions and its derivatives.

Name	Plot	Equation	Derivative
Linear		$f(x) = ax + b$	$f'(x) = a$
Unit Step		$f(x) = \begin{cases} 0 & \text{for } x < 0 \\ 1 & \text{for } x \geq 0 \end{cases}$	$f'(x) = \begin{cases} 0 & \text{for } x \neq 0 \\ \delta(x) & \text{for } x = 0 \end{cases}$
Logistic		$f(x) = \frac{1}{1+e^{-x}}$	$f'(x) = f(x)(1 - f(x))$
Tangent		$f(x) = \frac{2}{1+e^{-2x}} - 1$	$f'(x) = 1 - f(x)^2$
Arcotan		$f(x) = (\frac{2}{1+e^{-2x}} - 1)^{-1}$	$f'(x) = \frac{1}{x^2+1}$
SoftPlus		$f(x) = ln(1 + e^x)$	$f'(x) = \frac{1}{1+e^{-x}}$
Gaussian		$f(x) = e^{-x^2}$	$f'(x) = -2xe^{-x^2}$
Sinc		$f(x) = \begin{cases} 1 & \text{for } x = 0 \\ \frac{sin(x)}{x} & \text{for } x \neq 0 \end{cases}$	$f'(x) = \begin{cases} 0 & \text{for } x = 0 \\ \frac{cos(x)}{x} - \frac{sin(x)}{x^2} & \text{for } x \neq 0 \end{cases}$

3.3.4
ANN in photocatalysis

Some recent studies employed ANN in hydrogen production processes [12], whether monitoring parameters or estimating production rate. The goals in catalysis were prediction, classification and recognition [45] for theoretical or experimental studies. The reported results have successfully implemented the neural models [7, 8, 9, 10, 11].

Ghanbary et al. [8] applied ANN FF for photocatalytic prediction. They compared TiO_2 samples performance with different crystallite system as phases amount and crystallite size. They also encouraged the use of ANN for up-scaling simulation . They used the same photocatalyst of the present work. Another approach in common is the ANN modelling and no requirement of phenomena mechanisms. However, the use of neural models in the present study is distinct.

Verma et al. [46] applied ANN FF for degradation of Metronidazole (MTZ), widely used as antibiotic and seem as a pollutant in nature. The reaction of degradation uses TiO_2 photocatalyst. The input parameters were process variables: treatment time of MTZ, intensity of the UV light, the percentage surface area covered by the catalyst, Area/Volume ratio of the batch reactor, pH and the oxidant H_2O_2 dose. The output was the percentage of degradation. The regression coefficient suggested a well adjustment of the network, with $R^2_{train} = 0.9942$. The best network had one hidden layer with only four neurons.

Karimi-Jashni et al. [47] applied multilayer ANN FF for prediction of Chemical Oxygen Demand (COD) photocatalytic degradation, that is used as a variable for landfill leachate. They used tungsten doped TiO_2 nano-photocatalyst for the reaction performance. The input parameters were: percentage of tungsten content, calcination temperature, pH, and exposure time with the photocatalyst. The best network showed a good gorrelation with $R^2_{train} = 0.99$ and $R^2_{test} = 0.98$. They investigated the variables' relative importance and they also used genetic algorithm to determine the optimal degradation condition.

Yildirim et al. [48] applied ANN to establish a relationship between structural properties of CO and O_2 adsorption over gold photocatalyst. The input were the size, charge, unpaired electron, and coordination number of the gold atom bounded for each gas. Each output parameter was individually analysed: the band gap, the binding energy, the ionization potential and the electron affinity. The dataset was obtaneid from Density Functional Theory (DFT) simulation. They had a good implementation and prediction for all their data. They also suggested an improvement in the studied catalytic systems.

Bounding TiO_2 variables in ANN modelling for photocatalysis is a complex task due to its diversity. Collecting a database for them, it is even harder.

4
Methodology

The flowchart had four main steps (Figure 4.1) and, as a consequence of the ANN decisions, two Blocks (A and B). All steps related the database to the modelling. The ANN was implemented in the Matlab R2018b software and Deep Learning Toolbox (further information on Appendix).
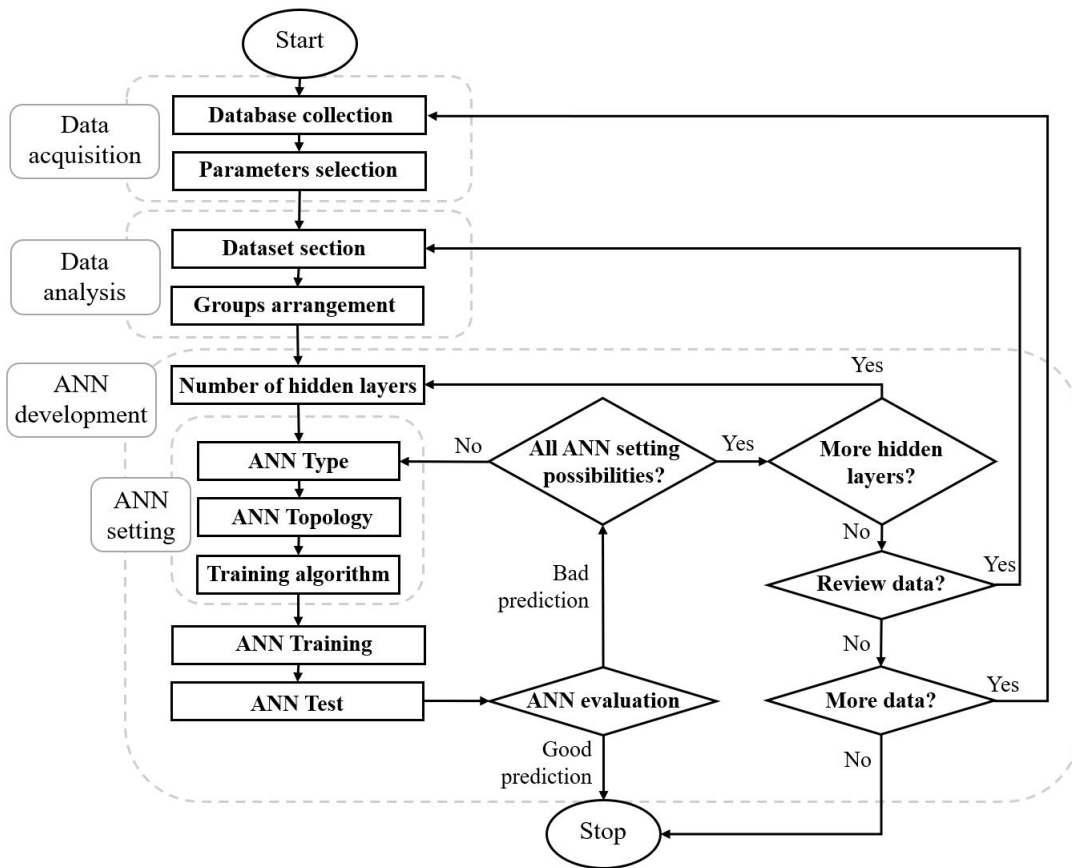
Figure 4.1: Methodology flowchart for the database construction and ANN development.

4.1
Data acquisition

First of all, articles, books and reviews were checked on the following search engines:

1. **Portal de Periódicos CAPES** - http://www-periodicos-gov-br.ez370.periodicos.capes.gov.br/

2. **Google Scholar** - https://scholar.google.com/

3. **Web of Science** - https://apps.webofknowledge.com/

4. **Scopus** - https://www.scopus.com/

Where the keywords terms used were either one or a combination of: "modelling", "photocatalyst", "characterization", "XRD", "DRS", "physisorption", "BET", "pore", "specific surface", "band gap", "TiO2", "photocatalysis", "anatase", "rutile", "anatase phase", "titania", "artificial neural network", "ANN", "crystal size", "crystallite size", "hydrogen production", "titanium dioxide", "synthesis".

Were considered only titanium dioxide photocatalyst, and no titanium-based or doped. In total, 53 different articles were used in the database.

After the Literature collection, the parameters with higher frequency report were selected from XRD, Nitrogen Physisorption and DRS techniques. The parameters used in this study were:

1. % A the percentage of anatase phase

2. % R the percentage of rutile phase

3. % B the percentage of brookite phase

4. dA [nm] the mean crystallite size of anatase phase

5. dR [nm] the mean crystallite size of rutile phase

6. dB [nm] the mean crystallite size of brookite phase

7. S $\left[\frac{m^2}{g}\right]$ the specific surface area

8. dP [nm] the pore diameter

9. Vol $\left[\frac{cm^3}{g}\right]$ the pore volume

10. CP the band gap correspondent phase

11. TT the transition type of band gap

12. Eg [eV] the band gap value

The variables CP and TT are values applied in this present work to support ANN recognition. Whenever the Correspondent Phase was not addressed by the source article or the analysed system presented a single phase, the value zero (0) was attributed to CP. The anatase phase was associated with number one (1); rutile, two (2) and brookite, three (3). For TT, the

direct allowed transition was assigned to 1; indirect allowed transition to 2; and forbidden transition or unknown, number zero. (Table 4.1)

Table 4.1: List of variables CP and TT for ANN modelling.

Phase	CP	Transition	TT
Anatase	1	indirect allowed	2
Rutile	2	direct allowed	1
Brookite	3	–	
Unknown	0	other	0

4.2
Data analysis

Then, all data were put in the same file in order to analyse them. The output parameter was only **Eg**, as an indirect photocatalytic evaluation parameter. Two Blocks A and B were defined, they had different input parameters where each group was divided into four and ten groups, respectively, in order to investigate the variables relationships. This strategy is usually used for the evaluation of the variables influence. [41]

The input parameters were **%A**, **dA**, **S**, **dP** and **Vol**. After the first attempts of ANN modelling, the mean pore diameter was not influencing the results. Making no difference, this parameter was totally discarded. Thus, Block A was divided into groups, investigating in pairs and with all parameters, as shown on Table 4.2.

Table 4.2: Parameters of Block A.

Group	Input				Output	Total of
	%A	dA	S	Vol	Eg	Vectors
I	x	x	–	–	x	249
II	x	–	x	–	x	206
III	x	–	–	x	x	124
IV	x	x	x	x	x	110

Where the cells assigned with "x" were considered and with dash were not.

Then, the full relation of crystalline phases was further investigated. Another gap in literature reports was faced: the Eg measurement and their correspondent relationship from the crystalline structure. Therefore, the variables

CP and **TT** were incorporated as input parameters as well as variables **%A**, **%R**, **%B**, **dA**,**dR**, **dB**. The Block B were divided into ten groups (Table 4.3).

Table 4.3: Parameters of Block B.

Group	Input								Output	Total of
	%A	%R	%B	dA	dR	dB	CP	TT	Eg	Vectors
I & SI	x	x	x	x	x	x	x	x	x	173 & 149
II & SII	x	x	–	x	x	–	x	x	x	183 & 163
III & SIII	x	–	–	x	–	–	x	x	x	220 & 191
IV & SIV	x	–	–	x	–	–	x	–	x	220 & 196
V & SV	x	–	–	x	–	–	–	x	x	220 & 196

Again, the cells assigned with "x" were considered and with dash were not. The crystallite size calculation from data including Rietveld Refinement were groups I to V. The ones that applied single peak Scherrer Equation were groups SI to SV.

The total of vectors varied according to experimental data found in the literature with all required variables for each group. The dataset was carefully divided - point by point - into the training data (80 %), looking out for the extremities, and the test data (20 %), ideally with no new combinations. As a consequence, the Blocks' results have had different valuation.

4.3
Training algorithms and transfer functions

The Backpropagation algorithm has been upgraded in order to be faster and have a better performance. For this, the implementation usually join η (learning rate) and α (momentum), considering the derivative from performance and the gradient minimization [39, 40]. It is the Gradient descent backpropagation (traingdx) Equation 4-1. This work used the Levenberg-Marquardt backpropagation (trainlm), the Levenberg-Marquardt backpropagation with Bayesian Regularisation (trainbr) and the One-step secant backpropagation (trainoss) algorithms. [43]

$$dX = \alpha.dX_{prev} + \eta.\alpha.\frac{d_{perf}}{dX} \tag{4-1}$$

dX: search direction
dX_{prev}: previous search direction
$\frac{d_{perf}}{dX}$: derivative from performance.

Trainlm is highly recommended due to its efficiency and quickness response. It is a second-order optimization that uses an approximation of

Jacobian matrix for minimization of weights and biases, assuming the errors values. The approximation matrix is an update from Newton's method, shown on Equation 4-2.

$$H = J^T J x_{k+1} = x_k - [J^T J + \mu I]^{-1} J^T e \tag{4-2}$$

H: Hessian matrix

J: Jacobian matrix

J^T: Transpose matrix

I: Identity matrix

e: vetor of network errors

On the other hand, trainbr uses not only the errors values, but also a linear combination between them and the weights in order to have a faster optimization than trainlm. The trainoss algorithm uses a secant approximation instead of linear approximation, requesting less computational storage and performance to minimize the gradients (Equation 4-3).

$$dX = -gX + A.X_{step} + B.dgX; \tag{4-3}$$

gX: gradient

X_{step}: weights change

dgX: gradient change

We used here difference equations: hyperbolic tangent sigmoid (tansig), logistic sigmoidal (logsig) and linear (purelin) functions. Tansig function (Equation 4-4 and derivative Equation 4-5) is a non linear transition between two states -1 and 1. Then, it can assume negative values. On the other hand, logsig (Equation 4-6 and derivative Equation 4-7) is between 0 and 1 values, assuming only positive results. The purelin (Equation 4-8 and derivative Equation 4-9) is a linear transition, so the information is constant.

$$f(x) = \frac{2}{1 + e^{-2x}} - 1 \tag{4-4}$$

$$\frac{df(x)}{dx} = \frac{4e^{-2x}}{1 + e^{-2x}} \tag{4-5}$$

$$f(x) = \frac{1}{1 + e^{-x}} \tag{4-6}$$

$$\frac{df(x)}{dx} = \frac{e^{-x}}{(1 + e^{-x})^2} \tag{4-7}$$

$$f(x) = x \tag{4-8}$$

$$\frac{df(x)}{dx} = 1 \qquad (4\text{-}9)$$

4.4
ANN development

All data were normalized, the gradient optimization was the SSE function for 10^{-4}, the convergence was also 10^{-4}, and the steps were 1000 epochs for block A and 3000 for B (Figure 8.13 on Chapter Appendix). The ANN parameters used for each Block were the type, algorithm, functions, and layers. They are listed in Table 4.4.

Table 4.4: List of ANN parameters for each block.

Parameters	Block A	Block B
ANN type (Type)	FF	FF, CF, ELM
Training algorithm (Alg.)	trainlm, trainbr, trainoss, traincgb	trainlm, trainbr, trainoss
Hidden layer function (Fx)	tansig, logsig	tansig, logsig
Number of hidden layers (x)	1	1, 2, 3
Transfer function (Fy)	purelin, tansig	purelin, tansig

For the first attempts, the ANN type was only FF. Then, for the Block B, we also included CF and ELM networks in order to improve the learning process. The ANN topology includes the transfer functions used and the hidden neurons selection. The transfer functions employed were tansig, logsig and purelin functions. The logsig was only applied for hidden layers and purelin for output layers.

Considering the peculiarity of each Block and Group, the number of inputs, outputs and hidden neurons were set to avoid calculation issues, where the maximum was set according to Equation 4-10.

$$\phi_1 = N0 + N0.N1 + N1 + N1.Ny + Ny$$
$$\phi_2 = N0 + N0.N1 + N1 + N1.N2 + N2 + N2.Ny + Ny \qquad (4\text{-}10)$$
$$\phi_3 = N0 + N0.N1 + N1 + N1.N2 + N2 + N2.N3 + N3.Ny + Ny$$

Where ϕ_1 is used for one hidden layer, ϕ_2 two and ϕ_3 three. N0 is the number of input neurons, N1 is the number of hidden neurons on the first hidden layer, N2 on the second hidden layer, N3 on the third hidden layer and Ny the output. Thus, ϕ must be less than the number of the training dataset.

The combinations of number of neurons are shown on Table 4.5 for one hidden layer evaluation and on Table 4.6 for two and three hidden layers.

Table 4.5: Number of hidden neurons tested set for one hidden layer.

	Group	Input	Hidden neurons (N1)	Output
	I	2	even{2 - 20}	1
Block A	**II**	2	even{2 - 20}	1
	III	2	even{2 - 20}	1
	IV	4	even{4 - 14}	1
	I	8	[8 - 13]	1
	SI	8	[8 - 11]	1
	II	6	[6 - 18]	1
	SII	6	[6 - 16]	1
	III	4	even{4 - 28}	1
Block B	**SII**	4	even{4 - 24}	1
	IV	3	odd{3 - 35}	1
	SIV	3	odd{3 - 31}	1
	V	3	odd{3 - 35}	1
	SV	3	odd{3 - 31}	1

Table 4.6: Hidden neurons tested set for more hidden layers on Block B.

Input neurons	Hidden neurons			Output neurons
	First layer (N1)	**Second layer** (N2)	**Third layer** (N3)	
4	{4, 6, 8}	even{4 - 22}	–	1
4	{4, 6}	{4, 6}	even{4 - 16}	1

4.5
ANN evaluation

For ANN evaluation, all models were compared by results of Sum Squared Error performance function (SSE, equation 4-11) for the training step; values of coefficient of determination (R^2 Equation 4-14) for both training and test; the linear line regression of observed and predicted values.

$$SSE = \sum_{i=1}^{n}(y_i^{observed} - \hat{y}_i^{predict})^2 \qquad (4\text{-}11)$$

$$SST = \sum_{i=1}^{n}(y_i^{observed} - \overline{y})^2 \qquad (4\text{-}12)$$

$$SSR = \sum_{i=1}^{n}(\hat{y}_i^{predict} - \overline{y})^2 \tag{4-13}$$

$$R^2 = 1 - \frac{SSE}{SST} = 1 - \frac{\sum_{i=1}^{n}(y_i^{observed} - \hat{y}_i^{predict})^2}{\sum_{i=1}^{n}(y_i^{observed} - \overline{y})^2} \tag{4-14}$$

Where $y_i^{observed}$ is the observed output value of data **i**, $\hat{y}_i^{predict}$ the predicted output value by the network, $\overline{y}$ the mean of **n** observed output values, SST is the total sum of squares, and SSR the residual sum of squares.

5
Results and discussion

5.1
Dataset results

To study the relation between TiO_2 properties and its photocatalytic performance, we adopted ANN modelling. Then, our first strategy choice was to investigate experimental literature reports instead of performing a laboratory investigation.

In the beginning of this study, we tried to implement together some processes results for the photocatalytic performance as hydrogen production rate. During the data collection in literature, we faced a philosophical issue that questioned how far could the literature reports be compared using a statistical tool. For instance the use of TiO_2 as photocatalyst in water splitting, each laboratory has its own reactor, its own light source, its own chemical solution. In Table 5.1, the reports of distinct research groups are represented with one photocatalyst each.

Table 5.1: Collection of processes data for hydrogen production from photacatalytic water splitting.

Photocatalyst	Morphology	Light Source	Light Spectrum	Solution	H_2 production rate μmol/h	Ref
SG400	spherical	Fluorescent 15w	300-400 [nm]	75 water 25 methanol	3.37	[26]
2.0TiCl$_4$/ 0.78Ti(OBu)$_4$	square bipyramid	Sun 2000 Solar Simulator	1 sun AM 1.5	electrolysis 0.9 V Ag/AgCl	4.78	[49]
#1	square bipyramid	Xenon 300W	–	methanol 10% v/v	153	[50]
A400	nanofiber	Xenon 350W	365 [nm]	80 water 20 methanol	37	[25]

Futhermore, each report has it own view of photocatalysis. For example, Masolo et al. [49] declares using "photoelectrolysis experiments" on "photocatalytic performances" with "H_2 evolution from the water splitting reaction", but some authors could not consider it as photocatalysis process.

Measurements of TiO_2 from characterization techniques seemed more consolidated and consonant. That is why we decided to investigate the performance through the band gap value, being designated as the output parameter.

5.2
Block A results

The first, in fact, data acquisition collected 52 photocatalyst reports (Tables 5.2 and 5.3).

Table 5.2: The smallest dataset of Block A.

	Photocatalyst	%A	dA	S	dP	Vol	Eg	*Ref*
1	SG400	100	13.0	61	3.5	0.344	3.22	[26]
2	SG500	100	19.0	37	3.5	0.209	3.23	[26]
3	SG600	100	33.0	24	3.5	0.185	3.22	[26]
4	SG650	96	38.0	24	–	0.149	3.20	[26]
5	SG700	88	45.0	20	–	0.125	3.16	[26]
6	SG750	62	54.0	17	–	0.071	3.10	[26]
7	SG800	6	66.0	6	~ 0	0.024	2.99	[26]
8	SG900	0	0.0	1	~ 0	0	2.98	[26]
9	HT	100	6.0	224	4.0	0206	3.11	[26]
10	HB	100	9.0	202	3.3	0.343	3.26	[26]
11	ML	100	21.0	76	7.4	0.307	3.27	[26]
12	KR	100	7	259	3.3	0.392	3.24	[26]
13	DP	82	23.0	49	2.5	0.176	3.18	[26]
14	KM	0	0.0	10	~ 0	0.034	3.00	[26]
15	hollow s. 6	100	40.0	75	91.0 102.3	0.22	2.60	[51]
16	core-shell s. 4	100	40.0	39	–	0.15	2.60	[51]
17	TiO2-A	11.4	20.3	45	11.9	0.133	3.04	[52]
18	TiO2-B	8.4	26.7	41	15.6	0.163	3.04	[52]
19	TiO2-C	0	0.0	42	16.0	0.170	3.00	[52]
20	TiO2-D	0	0.0	47	17.6	0.208	3.00	[52]
21	TiO2-E	0	0.0	63	17.5	0.233	3.00	[52]
22	TiO2-F	54.5	9.8	127	9.6	0.256	3.10	[52]
23	TiO2-G	72.3	8.5	133	10.4	0.294	3.10	[52]
24	Optimum	95	15.0	100	8.7	0.217	3.28	[53]
25	pH3	63	8.9	183	6.8	0.314	3.06	[54]

Table 5.3: The smallest dataset of Block A (continued of Table 5.2).

	Photocatalyst	%A	dA	S	dP	Vol	Eg	*Ref*
26	pH9	100	13.3	127	9.0	0.288	3.02	[54]
27	pH11	100	20.3	81	14.5	0.293	3.00	[54]
28	HTMT-300	100	7.3	295	6.9	0.450	3.16	[55]
29	HTMT-500	100	11.8	209	7.9	0.410	3.14	[55]
30	HTMT-700	100	22.3	87	10.1	0.280	3.08	[55]
31	TiO2 NTs	100	9.8	204	7.4	0.345	3.08	[56]
32	PTF-700	68	31.3	15	24.2	0.070	2.81	[57]
33	P25	83	350.0	39	20.0	0.470	2.95	[49]
					40.0			
34	1.0 TiCl4	87	220.0	196	7.1	0.630	3.02	[49]
					9.3			
35	HM-R2	0	0.0	173	13.0	0.022	3.00	[31]
					21.0			
					7.0			
36	HM-R2C	0	0.0	112	10.0	0.007	3.00	[31]
					26.0			
					6.0			
37	HM-R48	0	0.0	117	8.0	0.017	3.00	[31]
					22.0			
					6.0			
38	HM-R48C	0	0.0	92	8.0	0.009	3.00	[31]
					25.0			
					6.0			
39	FSP TiO2	81	28.0	109	15.0	0.180	3.17	[58]
40	A400	100	9.0	31	3.1	0.020	3.20	[25]

Table 5.4: The smallest dataset of Block A (continued of Table 5.2).

	Photocatalyst	%A	dA	S	dP	Vol	Eg	*Ref*
41	SC500	72	14.0	69	7.2	0.130	3.13	[25]
42	RC500	55	13.0	57	7.6	0.110	3.05	[25]
43	R800	0	0.0	5	5.6	0.010	3.00	[25]
44	G1HT2	82.1	5.2	247	4.2	0.160	3.29	[59]
45	G1HT4	81.4	5.9	240	4.4	0.330	3.30	[59]
46	G1HT6	82.11	6.4	203	5.0	0.330	3.27	[59]
47	G1HT8	90.79	6.5	211	5.6	0.390	3.28	[59]
48	G1HT10	93.19	6.7	190	6.1	0.390	3.38	[59]
49	G1HT12	95.21	6.9	198	5.6	0.370	3.40	[59]
50	SG750 (2)	73	45.5	15	–	0.102	3.10	[60]
51	TiO2-2	100	10.1	219	3.4	0.187	3.22	[61]
52	TiO2-3	100	13.8	188	4.9	0.231	3.24	[61]

The dataset was divided into training (44 vectors) and test (8 vectors). The training was carried out to have the set's maximum and minimum values, not only for the band gap but also for the other variables, being as representative as possible. Then, ANN models were developed. As previous mentioned, **dP** was not used for the ANN results because it had no difference on ANN results. Maybe because there were few data.

So, we used only FF network with 4 input neurons, where we first changed the number of hidden neurons, the transfer function and the training algorithm. We did not explored all combinations and did not get the SSE.

All topologies had a good adjustment of R^2, expect the **FF 4-7-1: trainlm, logsig, purelin** due to its $R^2_{test} = 0.40$ and the **FF 4-7-1: trainbr, tansig, purelin** with $R^2_{train} = 0.28$ and R^2_{test} 0.34. The results are shown in Table 5.5). The model **FF 4-7-1: trainlm, tansig, purelin** had $R^2_{train} = 0.9982$ (almost 1.00) and $R^2_{test} = 0.9093$ (almost 0.91), suggesting an overfitting due to the R^2 be almost one.

Table 5.5: ANN results of Block A with the smallest database.

Alg.	F1	N1	Fy	R^2_{train}	R^2_{test}
trainlm	tansig	4	purelin	0.9204	0.7196
trainlm	tansig	5	purelin	0.9736	0.7334
trainlm	tansig	6	purelin	0.9650	0.8108
trainlm	tansig	7	purelin	0.9982	0.9093
trainlm	logsig	4	purelin	0.9371	0.7450
trainlm	logsig	5	purelin	0.9432	0.7969
trainlm	logsig	6	purelin	0.9827	0.8650
trainlm	logsig	7	purelin	0.9745	0.3975
trainbr	tansig	7	purelin	0.2810	0.3391
trainoss	tansig	7	purelin	0.9135	0.6820
traincgb	tansig	7	purelin	0.9308	0.8130

All training dataset was well adjusted, but the test no. Analysing the responses data of band gap predicted from the model and the observed (Figure 5.1), it supports the training overfitting because all data seems only connected. Besides that, the model could not get the response behaviour, because the test range is not the same as the training and neural model can not extrapolate.
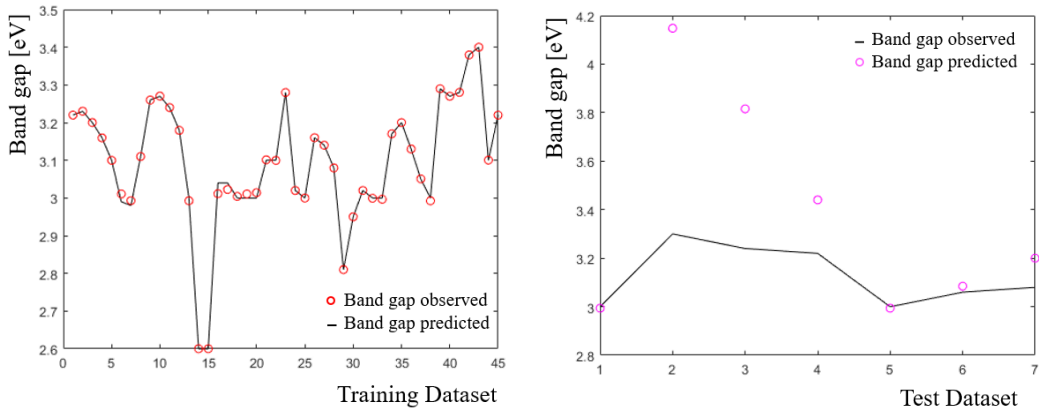
5.1(a): Training

5.1(b): Test

Figure 5.1: The dataset prediction of the result with the highest coefficients of Block A with the smallest database.

The regression line between the values predicted and observed showed a good agreement for the training recognition, being precise and accurate. However, for the test, the responses were really sparse. Due to the few test dataset, the fitting might have seemed well adjusted.

5.2(a): Training   5.2(b): Test
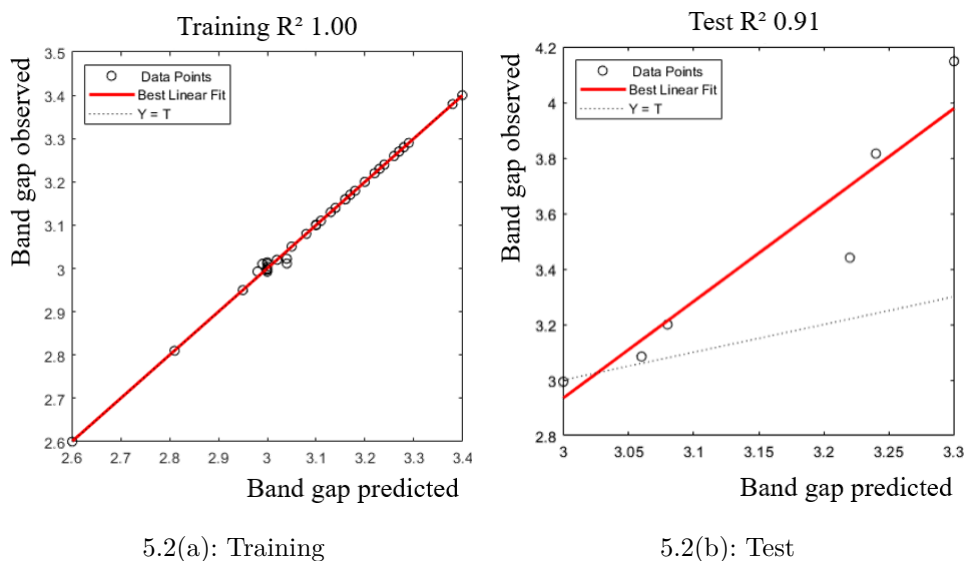
Figure 5.2: The ANN evaluation of the result with the highest coefficients of Block A with the smallest database.

In order to develop a model as diverse and representative as possible, we collected more data from literature and decided to investigate further so that each input pair would have been compared. That is, a new data acquisition.

We collected more 205 photocatalyst reports, totalling in 257 (Tables 5.6 to 5.13). The variables were the same as before. But the data were reanalysed and we discarded data points we considered flawed, as the 8 photocatalyst SG900 of a previous Block dataset, where its **S** value was 1 m^2/g.

We can also notice that a lot of papers reported the use of titania P25 as a blanck point for comparison. It may happen due to attempt a standardization of photocatalysis.

Table 5.6: Dataset I of Block A.

	Photocatalyst	%A	dA	S	Vol	Eg	*Ref*
1	SG400	100	13.0	61	0.344	3.22	[26]
2	SG500	100	19.0	37	0.209	3.23	[26]
3	SG600	100	33.0	24	0.185	3.22	[26]
4	SG650	96	38.0	24	0.149	3.20	[26]
5	SG700	88	45.0	20	0.125	3.16	[26]
6	SG750	62	54.0	17	0.071	3.10	[26]
7	SG800	6	66.0	6	0.024	2.99	[26]
8	HT	100	6.0	224	0.206	3.11	[26]
9	HB	100	9.0	202	0.343	3.26	[26]
10	ML	100	21.0	76	0.307	3.27	[26]
11	KR	100	7.0	259	0.392	3.24	[26]
12	DP	82	23.0	49	0.176	3.18	[26]
13	KM	0	0.0	10	0.034	3.00	[26]
14	TiO2-A	11	20.3	45	0.133	3.04	[52]
15	TiO2-B	8	26.7	41	0.163	3.04	[52]
16	TiO2-C	0	0.0	42	0.170	3.00	[52]
17	TiO2-D	0	0.0	47	0.208	3.00	[52]
18	TiO2-E	0	0.0	63	0.233	3.00	[52]
19	TiO2-F	55	9.8	127	0.256	3.10	[52]
20	TiO2-G	72	8.5	133	0.294	3.10	[52]
21	Optimum	95	15.0	100	0.217	3.28	[53]
22	pH3	63	8.9	183	0.314	3.06	[54]
23	pH9	100	13.3	127	0.288	3.02	[54]
24	pH11	100	20.3	81	0.293	3.00	[54]
25	HTMT-300	100	7.3	295	0.450	3.16	[55]
26	HTMT-500	100	11.8	209	0.410	3.14	[55]
27	HTMT-700	100	22.3	87	0.280	3.08	[55]
28	TiO2 NTs	100	9.8	204	0.345	3.08	[56]
29	PTF-700	68	31.3	15	0.070	2.81	[57]
30	P25	83	35.0	39	0.470	2.95	[49]
31	2.0 TiCl4	74	22.5	73	–	3.07	[49]
32	1.0 TiCl4	87	22.0	196	0.630	3.02	[49]
33	0.5 TiCl4	92	21.0	92	–	3.18	[49]
34	#1	4	28.0	24	–	3.00	[50]
35	#7	95	34.0	25	–	3.20	[50]

Table 5.7: Dataset II of Block A (continued of Table 5.6).

	Photocatalyst	%A	dA	S	Vol	Eg	*Ref*
36	HM-R2	0	0.0	173	0.022	3.00	[31]
37	HM-R2C	0	0.0	112	0.007	3.00	[31]
38	HM-R48	0	0.0	117	0.017	3.00	[31]
39	HM-R48C	0	0.0	92	0.009	3.00	[31]
40	FSP	81	28.0	109	0.180	3.17	[58]
41	A400	100	9.0	31	0.020	3.20	[25]
42	SC500	72	14.0	69	0.130	3.13	[25]
43	RC500	55	13.0	57	0.110	3.05	[25]
44	R800	0	0.0	5	0.010	3.00	[25]
45	G1HT4	81	5.9	240	0.330	3.30	[59]
46	G2HT4	80	6.2	158	0.300	3.23	[59]
47	G3HT4	79	6.2	161	0.270	3.28	[59]
48	G1M	100	17.6	52	0.130	3.27	[59]
49	G2M	100	12.8	90	0.130	3.25	[59]
50	G3M	83	10.9	75	0.140	3.24	[59]
51	G1HT2	82	5.2	247	0.160	3.29	[59]
52	G1HT4	81	5.9	240	0.330	3.30	[59]
53	G1HT6	82	6.4	203	0.330	3.27	[59]
54	G1HT8	91	6.5	211	0.390	3.28	[59]
55	G1HT10	93	6.7	190	0.390	3.38	[59]
56	G1HT12	95	6.9	198	0.370	3.40	[59]
57	Degussa P-25	80	22.0	52	–	3.20	[62]
58	Hombikat	100	7.0	280	–	3.22	[62]
59	SG-773	100	21.7	38	–	3.19	[62]
60	SG-873	100	36.9	28	–	3.19	[62]
61	SG-923	96	38.0	24	–	3.19	[62]
62	SG-973	97	50.0	24	–	3.17	[62]
63	SG-1023	92	57.0	18	–	2.97	[62]
64	SG-HT-423	100	6.5	182	–	3.26	[62]
65	SG-HT-773	100	11.9	88	–	3.25	[62]
66	SG-HT-873	100	26.2	38	–	3.25	[62]
67	SG-HT-923	100	40.7	21	–	3.24	[62]
68	SG-HT-973	96	56.1	12	–	3.13	[62]
69	SG-HT-1023	45	65.1	7	–	3.14	[62]
70	SG750 (2)	73	45.5	15	0.102	3.10	[60]

Table 5.8: Dataset III of Block A (continued of Table 5.6).

	Photocatalyst	%A	dA	S	Vol	Eg	*Ref*
71	TiO2-2	100	10.1	219	0.187	3.22	[61]
72	TiO2-3	100	13.8	188	0.231	3.24	[61]
73	TiO2-ST	97	28.0	35	0.160	3.19	[63]
74	TiO2-US	100	19.0	121	0.290	3.19	[63]
75	Crystal	100	18.1	–	–	3.40	[64]
76	MT - 600	100	21.8	54	0.230	3.10	[65]
77	Meso Titania	100	13.6	50	0.119	3.24	[66]
78	Commercial Titania	100	–	40	–	3.01	[66]
79	Reference	100	17.0	13	0.076	3.18	[67]
80	T5	100	11.0	139	–	3.57	[68]
81	TiO2 300	100	7.8	163	–	3.20	[69]
82	TNP - rotavapor	80	–	151	0.200	3.17	[70]
83	TNP- filtred	71	–	130	0.200	3.17	[70]
84	TNP - oven	69	–	121	0.200	3.17	[70]
85	TSC - glycine 400	55	–	85	–	3.08	[70]
86	TSC - glycine 500	60	–	90	–	3.08	[70]
87	TSC - urea 1:3	61	–	108	–	3.00	[70]
88	TSC - urea 1:1	58	–	65	–	3.00	[70]
89	TiO2 - P25	70	–	53	0.000	3.26	[70]
90	TiO2 - 500 undoped	100	–	49	0.108	3.14	[71]
91	TiO2 (PSG)	56	14.0	25	0.056	3.21	[72]
92	TiO2 (SCS)	100	10.5	177	0.170	3.26	[72]
93	TiO2 (MW)	100	6.0	251	0.558	3.64	[72]
94	TiO2 (PSG)	56	14.0	25	0.056	3.26	[72]
95	TiO2 (SCS)	100	10.5	177	0.170	3.42	[72]
96	TiO2 (MW)	100	6.0	251	0.558	3.50	[72]
97	TiO2 (PSG)	56	14.0	25	0.056	3.14	[72]
98	TiO2 (SCS)	100	10.5	177	0.170	3.43	[72]
99	TiO2 (MW)	100	6.0	251	0.558	3.48	[72]
100	T700	81	28.4	10	0.061	3.01	[73]
101	TA700	100	23.6	11	0.088	3.16	[73]
102	TT700	96	28.4	39	0.340	3.10	[73]
103	TC700	44	21.8	18	0.110	2.96	[73]
104	NI	100	14.0	92	0.460	2.95	[74]
105	NI450	100	16.0	79	0.420	3.00	[74]

Table 5.9: Dataset IV of Block A (continued of Table 5.6).

	Photocatalyst	%A	dA	S	Vol	Eg	*Ref*
106	NI500	100	17.0	77	0.380	2.99	[74]
107	NI550	100	18.0	68	0.460	2.99	[74]
108	undoped TiO2	86	3.9	5	0.007	3.17	[75]
109	dil. HCL #1	0	0.0	24	–	2.95	[76]
110	conc. HCL #1	0	0.0	29	–	2.98	[76]
111	conc. HCL #2	0	0.0	2	–	2.95	[76]
112	conc. HCL #3	0	0.0	8	–	3.02	[76]
113	dil. HCL #2	0	0.0	82	–	3.25	[76]
114	dil. HCL #3	0	0.0	69	–	3.28	[76]
115	dil. HCL #4	0	0.0	46	–	3.29	[76]
116	dil. HCL #5	0	0.0	18	–	3.24	[76]
117	dil. HCL #6	0	0.0	12	–	2.95	[76]
118	dil. HCL #7	0	0.0	141	–	3.15	[76]
119	dil. HCL #7	0	0.0	141	–	3.00	[76]
120	dil. HCL #8	0	0.0	35	–	3.16	[76]
121	dil. HCL #8	0	0.0	35	–	2.96	[76]
122	NaCl #1	71	2.2	189	–	3.00	[76]
123	NaCl #2	30	2.7	138	–	3.02	[76]
124	P25	80	25.1	50	–	3.02	[76]
125	TiO2	100	6.0	95	–	3.18	[77]
126	pure 0BDT	70	31.0	44	–	3.07	[78]
127	pure 0BDT	70	31.0	44	–	2.75	[78]
128	T-160	65	–	163	0.140	3.17	[79]
129	T-180	59	–	164	0.180	3.18	[79]
130	T-200	47	–	145	0.180	3.15	[79]
131	TiO2 P25 TM	70	15.6	50	–	3.22	[80]
132	TiO2-Brij56	50	7.0	100	0.350	3.02	[27]
133	TiO2-PEG	5	–	190	0.640	2.94	[27]
134	TiO2-PVA	30	9.0	150	0.280	2.97	[27]
135	TiO2-CTAB	40	11.0	70	0.180	2.99	[27]
136	P25	80	32.0	50	0.000	3.23	[27]
137	nanosized combustion TiO2	100	10.0	156	–	2.18	[81]
138	nanosized combustion TiO3	100	10.0	156	–	2.65	[81]
139	Methanol (nano 01)	69	17.0	69	–	3.19	[82]
140	Isopropyl alcohol (nano 02)	74	12.6	84	–	3.21	[82]

Table 5.10: Dataset V of Block A (continued of Table 5.6).

	Photocatalyst	%A	dA	S	Vol	Eg	*Ref*
141	Glacial acetic acid (nano 03)	82	8.3	107	–	3.27	[82]
142	Water150	73	12.0	86	–	3.19	[82]
143	Water250	78	10.6	94	–	3.26	[82]
144	Water350	83	8.1	110	–	3.28	[82]
145	Water450	74	8.6	91	–	3.21	[82]
146	T50	79	10.2	87	–	3.26	[82]
147	T60	78	9.6	98	–	3.24	[82]
148	T70	83	8.4	105	–	3.28	[82]
149	T80	76	11.3	97	–	3.23	[82]
150	6h	77	10.6	95	–	3.27	[82]
151	12h	82	8.3	108	–	3.29	[82]
152	24h	73	10.2	93	–	3.28	[82]
153	calcined 400	89	6.2	125	–	3.29	[82]
154	calcined 500	82	8.2	106	–	3.28	[82]
155	calcined 600	74	14.3	86	–	3.21	[82]
156	calcined 800	0	0.0	36	–	3.14	[82]
157	TiO2 - 100%	100	–	25	0.110	3.24	[83]
158	TiEt-450	100	15.1	43	0.650	3.22	[34]
159	TiEt-450	100	15.1	43	0.650	3.22	[34]
160	TiEt-600	97	39.1	2	0.340	3.21	[34]
161	TiMI-450	100	9.6	77	0.200	3.22	[34]
162	TiMI-600	100	13.6	35	0.130	3.21	[34]
163	TiHNO3-450	55	14.6	40	0.120	3.02	[34]
164	TiHNO3-600	9	27.3	3	0.060	2.97	[34]
165	TiO2	100	26.9	28	0.100	3.23	[84]
166	P25	80	30.0	63	0.060	3.00	[85]
167	TiO2	100	14.0	–	–	3.20	[86]
168	P-25	70	20.0	50	–	3.01	[87]
169	dil. HCl - Rutile	0	0.0	24	–	2.95	[76]
170	conc. HCl - Rutile	0	0.0	29	–	2.98	[76]
171	conc. HCl - Rutile 800	0	0.0	2	–	2.95	[76]
172	conc. HCl - Rutile Tioxide	0	0.0	8	–	3.02	[76]
173	dil. HCl - Brookite	0	0.0	82	–	3.25	[76]
174	dil. HCl - Brookite 300	0	0.0	69	–	3.28	[76]
175	dil. HCl - Brookite 450	0	0.0	46	–	3.29	[76]

Table 5.11: Dataset VI of Block A (continued of Table 5.6).

	Photocatalyst	%A	dA	S	Vol	Eg	*Ref*
176	dil. HCl - Brookite 750	0	0.0	18	–	3.24	[76]
177	dil. HCl - Rutile 900	0	0.0	12	–	2.95	[76]
178	dil. HCl - B/R -1	0	0.0	141	–	3.00	[76]
179	dil. HCl - B/R -1	0	0.0	141	–	3.15	[76]
180	dil. HCl - B/R -2	0	0.0	35	–	3.16	[76]
181	dil. HCl - B/R -2	0	0.0	35	–	2.96	[76]
182	NaCl - 1	71	2.2	189	–	3.00	[76]
183	NaCl - 2	30	2.7	138	–	3.02	[76]
184	P25	80	25.1	50	–	3.02	[76]
185	TiO2 (1:10)	7	19.0	150	–	3.07	[88]
186	TiO2 (1:10) dialysed	7	17.0	160	–	3.10	[88]
187	TiO2 (1:50)	9	15.0	210	–	3.12	[88]
188	TiO2 (1:50) dialysed	9	12.0	250	–	3.13	[88]
189	TiO2 (HCl, 24)	0	0.0	11	–	2.99	[88]
190	TiO2 (HCl, 48)	0	0.0	10	–	3.01	[88]
191	P25	72	25.0	50	–	3.13	[88]
192	Merck	74	60.0	10	–	3.18	[88]
193	TiO2 - pH3	79	–	80	0.150	3.05	[32]
194	TiO2 - pH5	100	–	43	0.240	3.27	[32]
195	TiO2 - pH7	93	–	10	0.050	3.21	[32]
196	TiO2 - pH9	100	–	88	0.220	3.32	[32]
197	T60	100	16.3	–	–	3.20	[89]
198	T65	57	19.3	–	–	2.70	[89]
199	T70	18	23.5	–	–	2.90	[89]
200	T75	0	0.0	–	–	3.00	[89]
201	P25	79	20.0	–	–	3.28	[90]
202	pH5 calcined 300	79	7.0	–	–	3.20	[91]
203	pH5 calcined 400	83	7.0	–	–	3.14	[91]
204	pH5 calcined 600	88	13.0	–	–	3.07	[91]
205	pH5 calcined 700	100	31.0	–	–	3.02	[91]
206	pH5 calcined 800	12	39.0	–	–	2.90	[91]
207	pH6 calcined 300	80	6.0	160	0.240	3.16	[91]
208	pH6 calcined 400	88	9.0	133	0.230	3.10	[91]
209	pH6 calcined 600	93	12.0	75	0.200	3.05	[91]
210	pH6 calcined 700	100	26.0	23	0.120	2.97	[91]

Table 5.12: Dataset VII of Block A (continued of Table 5.6).

	Photocatalyst	%A	dA	S	Vol	Eg	Ref
211	pH6 calcined 800	6	38.0	8	0.050	2.93	[91]
212	pH7 calcined 300	91	7.0	–	–	3.10	[91]
213	pH7 calcined 400	92	8.0	–	–	3.06	[91]
214	pH7 calcined 600	96	15.0	–	–	3.02	[91]
215	pH7 calcined 700	100	31.0	–	–	3.00	[91]
216	pH7 calcined 800	7	39.0	–	–	2.90	[91]
217	pH8 calcined 300	92	7.0	–	–	3.05	[91]
218	pH8 calcined 400	96	9.0	–	–	3.03	[91]
219	pH8 calcined 600	97	13.0	–	–	3.01	[91]
220	pH8 calcined 700	100	27.0	–	–	2.98	[91]
221	pH8 calcined 800	13	38.0	–	–	2.89	[91]
222	pH9 calcined 300	91	9.0	–	–	3.04	[91]
223	pH9 calcined 400	94	9.0	–	–	3.03	[91]
224	pH9 calcined 600	97	14.0	–	–	3.01	[91]
225	pH9 calcined 700	100	28.0	–	–	3.00	[91]
226	pH9 calcined 800	38	39.0	–	–	2.90	[91]
227	TESI	88	13.4	–	–	3.22	[92]
228	TENI	5	18.3	–	–	3.32	[92]
229	TEPCI	79	15.2	–	–	3.25	[92]
230	TECI	100	15.2	–	–	3.26	[92]
231	TEAI	77	15.2	–	–	3.21	[92]
232	TESI	88	13.4	–	–	2.83	[92]
233	TENI	5	18.3	–	–	3.05	[92]
234	TEPCI	79	15.2	–	–	2.96	[92]
235	TECI	100	15.2	–	–	3.26	[92]
236	TEAI	77	15.2	–	–	2.77	[92]
237	R1 - TiO2 80	0	0.0	–	–	3.16	[93]
238	R2 - TiO2 450	0	0.0	–	–	1.14	[93]
239	Figure 4e	100	14.9	76	0.290	3.35	[87]
240	Figure 6a1-2	100	25.0	85	0.320	3.30	[87]
241	Figure 4f	37	16.2	61	0.160	3.14	[87]
242	Figure 6b	53	19.2	98	0.280	3.22	[87]
243	Figure 5b	22	35.0	11	0.030	3.12	[87]
244	Figure 5c	90	15.1	49	0.130	3.30	[87]
245	Figure 4d	44	23.3	18	0.090	3.10	[87]

Table 5.13: Dataset VIII of Block A (continued of Table 5.6).

	Photocatalyst	%A	dA	S	Vol	Eg	*Ref*
246	Figure 4c	0	0.0	16	0.050	2.99	[87]
247	Figure 4g	0	0.0	59	0.110	3.16	[87]
248	Figure 4h	0	0.0	39	0.150	3.13	[87]
249	TWPI	100	5.7	–	–	3.41	[94]
250	TWSI	100	17.1	–	–	3.33	[94]
251	TWNI	100	15.2	–	–	3.32	[94]
252	TWPCI	100	18.3	–	–	3.29	[94]
253	TWCI	100	15.2	–	–	3.46	[94]
254	TWAI	100	13.0	–	–	3.41	[94]
255	powder A-480	100	10.4	58	–	3.13	[95]
256	powder A -550	100	12.8	–	–	3.18	[95]
257	powder A-600	100	14.9	–	–	3.23	[95]

The data was organized into groups for a better evaluation of input influences and relationships with the anatase phase in order to TiO_2 be represented. As the literature has not always all measurements for the photocatalyst, each group was analysed with different number of dataset and of hidden neurons.

5.2.1
Block A - Group I

This set has 249 vectors, two inputs, and one output, getting a matrix of variables and vectors of 747 contents. The data used from training was in total 199 photocatalysts (Tables 5.6 to 5.13). We developed 160 topologies for this group, where on Table 5.14 shows fifteen of them according to the highest R^2_{train}.

This group was the worst due to the values high **SSE**, low R^2_{train} and almost null R^2_{test}. The highest R^2_{test} was only 0.492 from topology **FF 2-6-1 trainoss, logsig, purelin** with SSE = 5.358 and R^2_{train} = 0.123.

ANN modelling could not adjust these parameters (% A, dA and Eg), suggesting they are either connected or it misses a correlation parameter. It seems to be the last option, due to both be values from the same technique and same crystalline structure of anatase phase.

Table 5.14: Results of Group I (%A, dA) from Block A with the highest R^2_{train}.

#	Alg.	F1	N1	Fy	SSE	R^2_{train}	R^2_{test}
1	trainlm	tansig	18	tansig	3.597	0.412	0.005
2	trainlm	logsig	18	tansig	3.598	0.411	0.024
3	trainlm	tansig	20	purelin	3.603	0.411	0.002
4	trainlm	tansig	16	tansig	3.683	0.397	0.087
5	trainlm	tansig	14	purelin	3.736	0.389	0.009
6	trainlm	logsig	16	tansig	3.814	0.376	0.057
7	trainlm	tansig	12	tansig	3.896	0.363	0.021
8	trainlm	tansig	18	purelin	4.027	0.341	0.008
9	trainlm	tansig	16	purelin	4.107	0.328	0.000
10	trainlm	logsig	12	purelin	4.208	0.311	0.066
11	trainlm	logsig	18	purelin	4.264	0.302	0.030
12	trainlm	logsig	20	purelin	4.266	0.302	0.006
13	trainlm	logsig	16	purelin	4.341	0.290	0.014
14	trainlm	logsig	14	purelin	4.363	0.286	0.003
15	trainlm	tansig	10	purelin	4.399	0.280	0.034

5.2.2
Block A - Group II

This set has 206 vectors, two inputs, and one output, getting a matrix of variables and vectors of 618 contents. The data used from training was in total 165 photocatalysts (Tables 5.6 to 5.13). We developed 160 topologies for this group, where on Table 5.15 shows fifteen of them according to the highest R^2_{train}.

This group had a good adjustment for training, but could not be validated. The highest R^2_{test} was 0.444 with a huge SSE (129) and poor R^2_{train} (0.093), which topology was **FF 2-20-1 trainlm, logisg, tansig**.

We can infer that the dataset was diverse, but was not enough to represent the relationship with the band gap.

Table 5.15: Results of Group II (%A, S) from Block A with the highest R^2_{train}.

#	Alg.	F1	N1	Fy	SSE	R^2_{train}	R^2_{test}
1	trainlm	logsig	20	purelin	1.335	0.833	0.023
2	trainlm	tansig	20	purelin	1.443	0.820	0.022
3	trainlm	logsig	18	purelin	1.558	0.805	0.004
4	trainlm	tansig	18	tansig	1.560	0.805	0.007
5	trainlm	logsig	16	tansig	1.586	0.802	0.018
6	trainlm	logsig	18	tansig	1.696	0.788	0.013
7	trainlm	logsig	14	tansig	1.874	0.766	0.000
8	trainlm	tansig	18	purelin	1.888	0.764	0.068
9	trainlm	tansig	16	purelin	1.909	0.762	0.014
10	trainlm	tansig	14	purelin	1.963	0.755	0.004
11	trainlm	tansig	16	tansig	1.971	0.754	0.001
12	trainlm	logsig	14	purelin	2.015	0.748	0.008
13	trainlm	logsig	16	purelin	2.031	0.746	0.008
14	trainlm	tansig	14	tansig	2.186	0.727	0.017
15	trainlm	logsig	10	tansig	2.246	0.719	0.068

5.2.3
Block A - Group III

This set has 124 vectors, two inputs, and one output, getting a matrix of variables and vectors of 372 contents. The data used from training was in total 99 photocatalysts (Tables 5.6 to 5.13). We developed 160 topologies for this group, where on Table 5.16 shows fifteen of them according to the highest R^2_{train}.

This group had a better adjustment than groups I and II. Although the high R^2_{train}, the models could not be validate as well due to the low R^2_{test}. The highest one was 0.593 with SSE = 8.637, $R^2_{train} = 0.238$ for **FF 2-4-1 trainbr, logsig, tansig**.

Table 5.16: Results of Group III (%A, Vol) from Block A with the highest R^2_{train}.

#	Alg.	F1	N1	Fy	SSE	R^2_{train}	R^2_{test}
1	trainlm	logsig	18	purelin	0.925	0.918	0.199
2	trainlm	tansig	20	purelin	0.964	0.915	0.236
3	trainlm	logsig	20	purelin	1.117	0.901	0.042
4	trainlm	logsig	20	tansig	1.136	0.900	0.135
5	trainlm	logsig	16	purelin	1.164	0.897	0.005
6	trainlm	logsig	14	tansig	1.275	0.888	0.328
7	trainlm	tansig	16	purelin	1.326	0.883	0.099
8	trainlm	tansig	20	tansig	1.436	0.874	0.041
9	trainlm	tansig	14	tansig	1.467	0.870	0.232
10	trainlm	tansig	14	purelin	1.476	0.870	0.030
11	trainlm	logsig	16	tansig	1.481	0.869	0.141
12	trainlm	logsig	14	purelin	1.550	0.863	0.108
13	trainlm	tansig	18	purelin	1.808	0.840	0.038
14	trainlm	tansig	12	purelin	1.908	0.831	0.020
15	trainlm	tansig	16	tansig	1.931	0.830	0.214

5.2.4
Block A - Group IV

This set has 110 vectors, four inputs, and one output, getting a matrix of variables and vectors of 550 contents. The data used from training was in total 88 photocatalysts (Tables 5.6 to 5.13). We developed 96 topologies for this group, where on Table 5.17 shows fifteen of them according to the highest R^2_{train}.

Table 5.17: Results of Group IV (%A, dA, S, Vol) from Block A with the highest R^2_{train}.

#	Alg.	F1	N1	Fy	SSE	R^2_{train}	R^2_{test}
1	trainlm	logsig	14	purelin	0.202	0.982	0.005
2	trainlm	tansig	14	tansig	0.204	0.981	0.026
3	trainlm	tansig	14	purelin	0.204	0.981	0.253
4	trainlm	tansig	12	purelin	0.316	0.971	0.156
5	trainlm	logsig	12	purelin	0.382	0.965	0.018
6	trainlm	tansig	12	tansig	0.458	0.958	0.047
7	trainlm	logsig	12	tansig	0.545	0.950	0.056
8	trainlm	tansig	10	purelin	0.999	0.909	0.113
9	trainlm	logsig	10	purelin	1.025	0.906	0.003
10	traincgb	logsig	12	purelin	1.153	0.895	0.014
11	traincgb	tansig	14	tansig	1.229	0.888	0.107
12	traincgb	tansig	12	purelin	1.258	0.885	0.004
13	traincgb	logsig	14	purelin	1.308	0.880	0.304
14	traincgb	tansig	12	tansig	1.317	0.880	0.091
15	traincgb	tansig	14	purelin	1.356	0.876	0.391

This group had the best training adjustment of Block A. But again, with low adjustment for the test. The third highest R^2_{train} was around 0.98 with 14 hidden neurons and a combination of the transfer functions. As the N1 was as large as possible, these results suggest an overfitting (Figure 5.3).
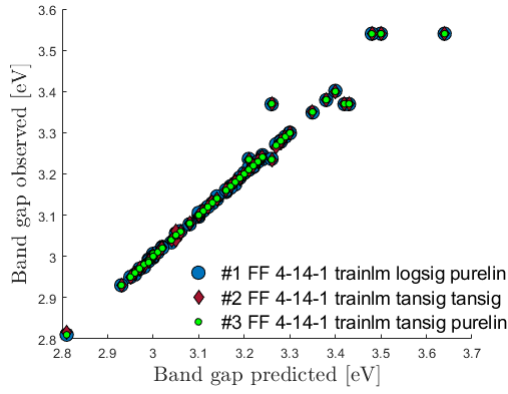
5.3(a): Training
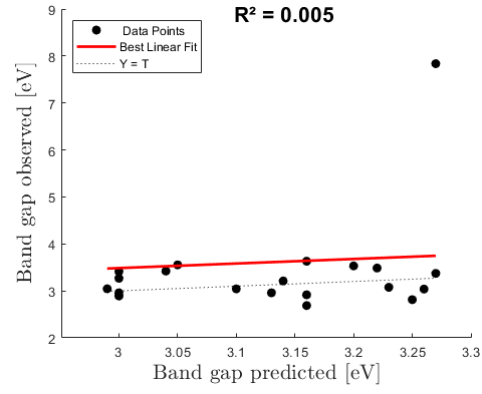
5.3(b): Test #1
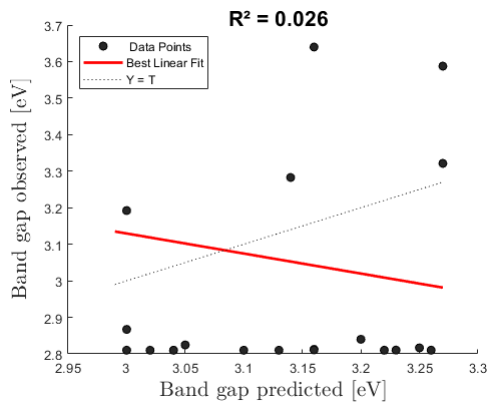
5.3(c): Test #2
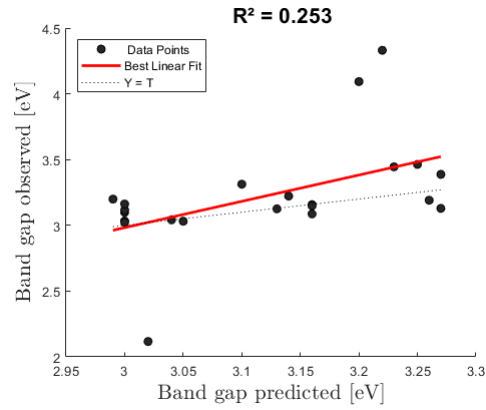
5.3(d): Test #3

Figure 5.3: The highest R^2_{train} of ANN results of Group IV of Block A.

The training of # 1, # 2 and # 3 overlapped. But the test adjustments were different. The #2 had a negative regression and none was precise or linear.

On the other hand, the highest R^2_{test} was 0.522, with 70 % of approval of the training and SSE = 3.278, for topology **FF 4-4-1 trainlm, tansig, purelin**.

To evaluate the error, we analysed the values between the predicted and observed on Figure 5.4. We noticed an odd behavior of the relation, as a horizontal dispersion error for the training. The test was neither precise nor accurate.

5.4(a): Training

5.4(b): Test
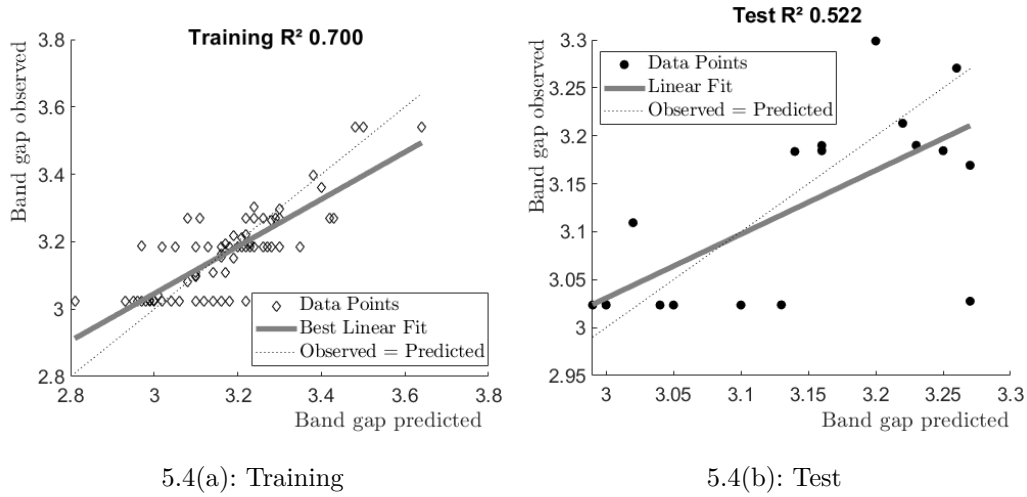
Figure 5.4: Regression diagram of **FF 4-4-1 trainlm, tansig, purelin** Group IV, Block A.

Figure 5.5 has both training and test dataset prediction. They confirm the non linearity of output values and the modelling failure.

5.5(a): Training

5.5(b): Test
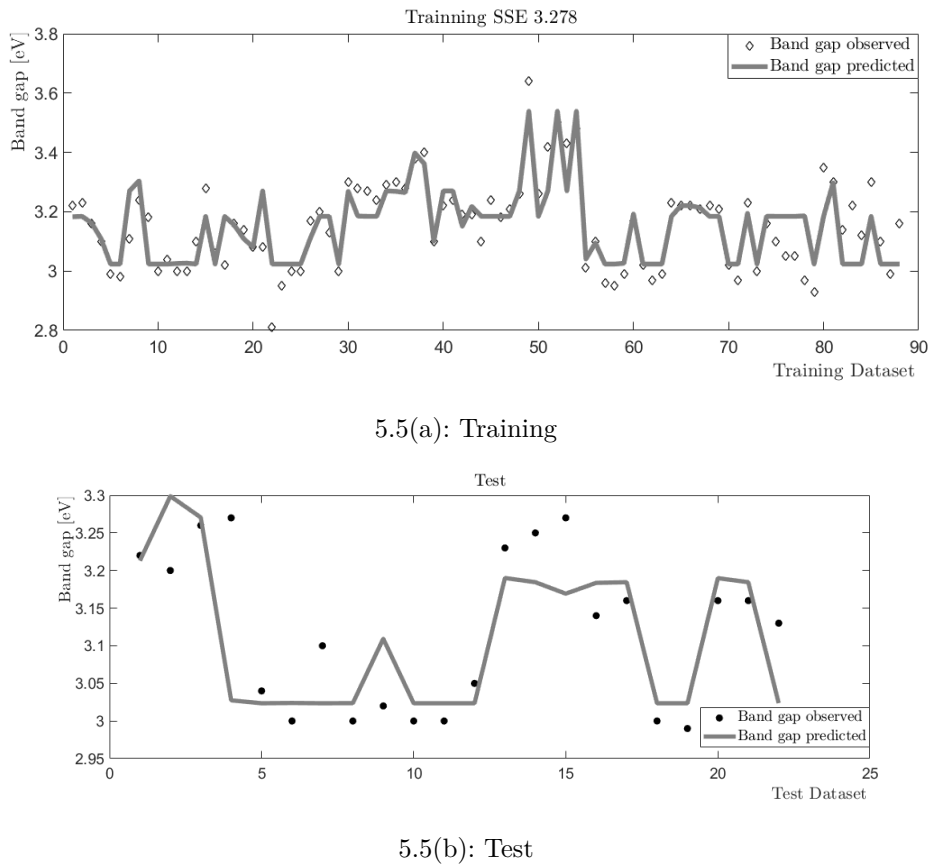
Figure 5.5: Prediction behaviour of **FF 4-4-1 trainlm, tansig, purelin** Group IV, Block A.

Almost all results had insignificant R^2_{test}. The %A and dA variables may

have no direct relation to Eg or only them was not enough, though. Moreover, not only **S** but also **Vol** variables might be direct associated with anatase phase on the band gap value, but the database might not be as representative.

Nevertheless, the group IV result was not expected. The incorporation of new data should have improved the ANN model. But only 70 % of the training data could be predicted and half of the test.

By far trainlm was the algorithm that best fitted, due to have the results with the highest coefficients with the lowest error in all groups. We can not say about the transfer functions, because for each network they changed.

Then, even having a diverse dataset, but not a good prediction, we considered this block was enough explored. Thus we decided to review our data acquisition establishing the Block B.

5.3
Block B results

Due to the group IV of Block A results, for Block B we decided to collect other variables corresponding on other crystalline phases of crystallite TiO_2, that is, rutile and brookite phases. We no longer used **S** and **Vol** as input parameters.

While we were collecting the information of the other crystalline phases, we noticed two issues. The first is that the majority reports ignored the less present phases and they were not measured. Then we expanded the search for new reports on literature in order to expand the dataset. The second is that we should have added the two variables **CP** and **TT** in order to avoid misunderstood and support ANN modelling. For instance, some data reported the transition type of the bad gap and measured the DRS values with more than one method, getting two values for **Eg**. Others also attached the band gap values with the respective phase.

We reorganized the reports and acquired more, resulting in 220 photocatalysts (Tables 5.18 to 5.24).

Table 5.18: Dataset I for Block B.

	Photocatalyst	%A	%R	%B	dA	dR	dB	CP	TT	Eg	*Ref*
1	SG400	100	0	0	13.0	0	0	1	0	3.22	[26]
2	SG500	100	0	0	19.0	0	0	1	0	3.23	[26]
3	SG600	100	0	0	33.0	0	0	1	0	3.22	[26]
4	SG650	96	4	0	38.0	45.0	0	0	0	3.20	[26]
5	SG700	88	12	0	45.0	55.0	0	0	0	3.16	[26]
6	SG750	62	38	0	54.0	54.0	0	0	0	3.10	[26]
7	SG800	6	94	0	66.0	87.0	0	0	0	2.99	[26]
8	SG900	0	100	0	0	96.0	0	2	0	2.98	[26]
9	HT	100	0	0	6.0	0	0	1	0	3.11	[26]
10	HB	100	0	0	9.0	0	0	1	0	3.26	[26]
11	ML	100	0	0	21.0	0	0	1	0	3.27	[26]
12	DP	82	18	0	23.0	44.0	0	0	0	3.18	[26]
13	KM	0	100	0	0	68.0	0	2	0	3.00	[26]
14	TiO2-A	11	68	21	20.3	–	–	0	0	3.04	[52]
15	TiO2-B	8	71	20	26.7	–	–	0	0	3.04	[52]
16	TiO2-C	0	100	0	0	21.1	0	2	0	3.00	[52]
17	TiO2-D	0	100	0	0	18.3	0	2	0	3.00	[52]
18	TiO2-E	0	100	0	0	16.6	0	2	0	3.00	[52]
19	TiO2-F	54	44	0	9.8	–	0	0	0	3.10	[52]
20	TiO2-G	72	28	0	8.5	–	0	0	0	3.10	[52]
21	Optimum	95	5	0	15.0	12.0	0	0	1	3.28	[53]
22	pH3	63	0	37	8.9	0	–	0	1	3.06	[54]
23	pH9	100	0	0	13.3	0	0	1	1	3.02	[54]
24	pH11	100	0	0	20.3	0	0	1	1	3.00	[54]
25	HTMT-300	100	0	0	7.3	0.0	0	1	1	3.16	[55]
26	HTMT-500	100	0	0	11.8	0.0	0	1	1	3.14	[55]
27	HTMT-700	100	0	0	22.3	0.0	0	1	1	3.08	[55]
28	TiO2 NTs	100	0	0	9.8	0.0	0	1	2	3.08	[56]
29	PTF-700	68	32	0	31.3	–	0	0	0	2.81	[57]
30	P25	83	17	0	35.0	52.5	0	0	0	2.95	[49]
31	2.0 TiCl4	74	26	0	22.5	23.0	0	0	0	3.07	[49]
32	1.0 TiCl4	87	13	0	22.0	21.0	0	0	0	3.02	[49]
33	0.5 TiCl4	92	78	0	21.0	19.0	0	0	0	3.18	[49]
34	#1	4	96	0	28.0	36.0	0	2	2	3.00	[50]
35	#7	95	5	0	34.0	28.0	0	1	2	3.20	[50]

Table 5.19: Dataset II of Block B (continued of Table 5.18).

	Photocatalyst	%A	%R	%B	dA	dR	dB	CP	TT	Eg	Ref
36	HM-R2	0	100	0	0.0	7.5	0	2	0	3.00	[31]
37	HM-R2C	0	100	0	0.0	9.9	0	2	0	3.00	[31]
38	HM-R48	0	100	0	0.0	10.5	0	2	0	3.00	[31]
39	HM-R48C	0	100	0	0.0	12.8	0	2	0	3.00	[31]
40	FSP	81	19	0	28.0	125.0	0	0	0	3.17	[58]
41	A400	100	0	0	9.0	0.0	0	1	0	3.20	[25]
42	SC500	72	28	0	14.0	23.0	0	0	0	3.13	[25]
43	RC500	55	45	0	13.0	21.0	0	0	0	3.05	[25]
44	R800	0	100	0	0.0	43.0	0	2	0	3.00	[25]
45	G1HT4	81	0	19	5.9	0.0	−	0	2	3.30	[59]
46	G2HT4	80	0	20	6.2	0.0	−	0	2	3.23	[59]
47	G3HT4	79	0	21	6.2	0.0	−	0	2	3.28	[59]
48	G1M	100	0	0	17.6	0.0	0	0	2	3.27	[59]
49	G2M	100	0	0	12.8	0.0	0	0	2	3.25	[59]
50	G3M	83	0	17	10.9	0.0	−	0	2	3.24	[59]
51	G1HT2	82	0	18	5.2	0.0	−	0	2	3.29	[59]
52	G1HT6	82	0	18	6.4	0.0	−	0	2	3.27	[59]
53	G1HT8	91	0	9	6.5	0.0	−	0	2	3.28	[59]
54	G1HT10	93	0	7	6.7	0.0	−	0	2	3.38	[59]
55	G1HT12	95	0	5	6.9	0.0	−	0	2	3.40	[59]
56	P-25	80	20	0	22.0	85.0	0	0	2	3.20	[62]
57	Hombikat	100	0	0	7.0	0.0	0	1	2	3.22	[62]
58	SG-773	100	0	0	21.7	0.0	0	1	2	3.19	[62]
59	SG-873	100	0	0	36.9	0.0	0	1	2	3.19	[62]
60	SG-923	96	4	0	38.0	45.0	0	0	2	3.19	[62]
61	SG-973	97	3	0	50.0	101.6	0	0	2	3.17	[62]
62	SG-1023	92	8	0	57.0	86.3	0	0	2	2.97	[62]
63	SG-HT-423	100	0	0	6.5	0.0	0	1	2	3.26	[62]
64	SG-HT-773	100	0	0	11.9	0.0	0	1	2	3.25	[62]
65	SG-HT-873	100	0	0	26.2	0.0	0	1	2	3.25	[62]
66	SG-HT-923	100	0	0	40.7	0.0	0	1	2	3.24	[62]
67	SG-HT-973	96	4	0	56.1	142.3	0	0	2	3.13	[62]
68	SG-HT-1023	45	55	0	65.1	105.1	0	0	2	3.14	[62]
69	TiO2-2	100	0	0	10.1	0.0	0	1	1	3.22	[61]
70	TiO2-3	100	0	0	13.8	0.0	0	1	1	3.24	[61]

Table 5.20: Dataset III of Block B (continued of Table 5.18).

	Photocatalyst	%A	%R	%B	dA	dR	dB	CP	TT	Eg	*Ref*
71	TiO2-ST	97	3	0	28.0	–	0	0	2	3.19	[63]
72	TiO2-US	100	0	0	19.0	0.0	0	1	2	3.19	[63]
73	Crystal	100	0	0	18.1	0.0	0	1	2	3.40	[64]
74	MT - 600	100	0	0	21.8	0.0	0	1	2	3.10	[65]
75	Meso Titania	100	0	0	13.6	0.0	0	1	1	3.24	[66]
76	Reference	100	0	0	17.0	0.0	0	1	2	3.18	[67]
77	T5	100	0	0	11.0	0.0	0	1	0	3.57	[68]
78	TiO2 300	100	0	0	7.8	0.0	0	1	0	3.20	[69]
79	PSG	56	44	0	14.0	–	0	0	2	3.21	[72]
80	SCS	100	0	0	10.5	0.0	0	1	2	3.26	[72]
81	MW	100	0	0	6.0	0.0	0	1	2	3.64	[72]
82	PSG	56	44	0	14.0	–	0	0	0	3.26	[72]
83	SCS	100	0	0	10.5	0.0	0	1	0	3.42	[72]
84	MW	100	0	0	6.0	0.0	0	1	0	3.50	[72]
85	PSG	56	44	0	14.0	–	0	0	1	3.14	[72]
86	SCS	100	0	0	10.5	0.0	0	1	1	3.43	[72]
87	MW	100	0	0	6.0	0.0	0	1	1	3.48	[72]
88	T700	81	19	0	28.4	31.7	0	0	2	3.01	[73]
89	TA700	100	0	0	23.6	0.0	0	1	2	3.16	[73]
90	TT700	96	4	0	28.4	40.7	0	0	2	3.10	[73]
91	TC700	44	56	0	21.8	40.7	0	0	2	2.96	[73]
92	NI	100	0	0	14.0	0.0	0	1	2	2.95	[74]
93	NI450	100	0	0	16.0	0.0	0	1	2	3.00	[74]
94	NI500	100	0	0	17.0	0.0	0	1	2	2.99	[74]
95	NI550	100	0	0	18.0	0.0	0	1	2	2.99	[74]
96	undoped TiO2	86	14	0	3.9	12.3	0	0	0	3.17	[75]
97	dil. HCL #1	0	100	0	0.0	3.8	0	2	2	2.95	[76]
98	conc. HCL #1	0	100	0	0.0	4.3	0	2	2	2.98	[76]
99	conc. HCL #2	0	100	0	0.0	25.4	0	2	2	2.95	[76]
100	conc. HCL #3	0	100	0	0.0	50.0	0	2	2	3.02	[76]
101	dil. HCL #2	0	0	100	0.0	0.0	7	3	2	3.25	[76]
102	dil. HCL #3	0	0	100	0.0	0.0	8	3	2	3.28	[76]
103	dil. HCL #4	0	0	100	0.0	0.0	10	3	2	3.29	[76]
104	dil. HCL #5	0	0	100	0.0	0.0	16	3	2	3.24	[76]
105	dil. HCL #6	0	100	0	0.0	32.7	0	2	2	2.95	[76]

Table 5.21: Dataset IV of Block B (continued of Table 5.18).

	Photocatalyst	%A	%R	%B	dA	dR	dB	CP	TT	Eg	*Ref*
106	dil. HCL #7	0	26	74	0.0	4.2	4	3	2	3.15	[76]
107	dil. HCL #7	0	26	74	0.0	4.2	4	2	2	3.00	[76]
108	dil. HCL #8	0	61	40	0.0	4.7	9	3	2	3.16	[76]
109	dil. HCL #8	0	61	40	0.0	4.7	9	2	2	2.96	[76]
110	NaCl #1	71	13	16	2.2	7.1	3	1	2	3.00	[76]
111	NaCl #2	30	63	7	2.7	5.0	5	1	2	3.02	[76]
112	P25	80	20	0	25.1	33.2	0	1	2	3.02	[76]
113	TiO2	100	0	0	6.0	0.0	0	1	0	3.18	[77]
114	pure 0BDT	70	30	0	31.0	–	0	0	1	3.07	[78]
115	pure 0BDT	70	30	0	31.0	–	0	0	2	2.75	[78]
116	PVA	30	70	0	9.0	10.0	0	0	0	2.97	[27]
117	CTAB	40	60	0	11.0	10.0	0	0	0	2.99	[27]
118	P25	80	20	0	32.0	52.0	0	0	0	3.23	[27]
119	Brij56	50	50	0	7.0	10.0	0	0	0	3.02	[27]
120	P25 TM	70	30	0	15.6	–	0	0	2	3.22	[80]
121	TiO2	100	0	0	10.0	0.0	0	1	0	2.18	[81]
122	TiO3	100	0	0	10.0	0.0	0	1	0	2.65	[81]
123	nano 01	69	31	0	17.0	–	0	0	0	3.19	[82]
124	nano 02	74	26	0	12.6	–	0	0	0	3.21	[82]
125	nano 03	82	18	0	8.3	–	0	0	0	3.27	[82]
126	Water150	73	27	0	12.0	–	0	0	0	3.19	[82]
127	Water250	78	22	0	10.6	–	0	0	0	3.26	[82]
128	Water350	83	17	0	8.1	–	0	0	0	3.28	[82]
129	Water450	74	26	0	8.6	–	0	0	0	3.21	[82]
130	T50	79	21	0	10.2	–	0	0	0	3.26	[82]
131	T60	78	22	0	9.6	–	0	0	0	3.24	[82]
132	T70	83	17	0	8.4	–	0	0	0	3.28	[82]
133	T80	76	24	0	11.3	–	0	0	0	3.23	[82]
134	6h	77	23	0	10.6	–	0	0	0	3.27	[82]
135	12h	82	18	0	8.3	–	0	0	0	3.29	[82]
136	24h	73	27	0	10.2	–	0	0	0	3.28	[82]
137	calcined 400	89	11	0	6.2	–	0	0	0	3.29	[82]
138	calcined 500	82	18	0	8.2	–	0	0	0	3.28	[82]
139	calcined 600	74	26	0	14.3	–	0	0	0	3.21	[82]
140	calcined 800	0	100	0	0.0	21.1	0	2	0	3.14	[82]

Table 5.22: Dataset V of Block B (continued of Table 5.18).

	Photocatalyst	%A	%R	%B	dA	dR	dB	CP	TT	Eg	*Ref*
141	TiEt-450	100	0	0	15.1	0.0	0	1	1	3.22	[34]
142	TiEt-600	97	3	0	39.1	–	0	0	1	3.21	[34]
143	TiMI-450	100	0	0	9.6	0.0	0	1	1	3.22	[34]
144	TiMI-600	100	0	0	13.6	0.0	0	1	1	3.21	[34]
145	TiHNO3-450	55	45	0	14.6	22.2	0	0	1	3.02	[34]
146	TiHNO3-600	9	91	0	27.3	37.5	0	0	1	2.97	[34]
147	TiO2	100	0	0	26.9	0.0	0	1	2	3.23	[84]
148	P25	80	20	0	30.0	–	0	0	1	3.00	[85]
149	TiO2	100	0	0	14.0	0.0	0	1	2	3.20	[86]
150	1:10	7	0	0	19.0	0.0	0	0	2	3.07	[88]
151	1:10 dialysed	7	0	0	17.0	0.0	0	0	2	3.10	[88]
152	1:50	9	0	0	15.0	0.0	0	0	2	3.12	[88]
153	1:50 dialysed	9	0	0	12.0	0.0	0	0	2	3.13	[88]
154	TiO2 (HCl, 24)	0	21	0	0.0	20.0	0	0	2	2.99	[88]
155	TiO2 (HCl, 48)	0	32	0	0.0	25.0	0	0	2	3.01	[88]
156	P25	72	18	0	25.0	33.0	0	0	2	3.13	[88]
157	Merck	74	0	0	60.0	0.0	0	0	2	3.18	[88]
158	T60	100	0	0	16.3	0.0	0	1	2	3.20	[89]
159	T65	57	43	0	19.3	17.1	0	0	2	2.70	[89]
160	T70	18	82	0	23.5	19.0	0	0	2	2.90	[89]
161	T75	0	100	0	0.0	21.0	0	2	2	3.00	[89]
162	P25	79	21	0	20.0	23.0	0	0	0	3.28	[90]
163	pH5 cal.300	79	0	0	7.0	0.0	7	0	2	3.20	[91]
164	pH5 cal.400	83	0	17	7.0	0.0	7	0	2	3.14	[91]
165	pH5 cal.600	88	0	12	13.0	0.0	6	0	2	3.07	[91]
166	pH5 cal.700	100	0	0	31.0	0.0	0	1	2	3.02	[91]
167	pH5 cal.800	12	88	0	39.0	55.4	0	0	2	2.90	[91]
168	pH6 cal.300	80	0	20	6.0	0.0	7	0	2	3.16	[91]
169	pH6 cal.400	88	0	12	9.0	0.0	8	0	2	3.10	[91]
170	pH6 cal.600	93	0	7	12.0	0.0	7	0	2	3.05	[91]
171	pH6 cal.700	100	0	0	26.0	0.0	0	1	2	2.97	[91]
172	pH6 cal.800	6	94	0	38.0	55.4	0	0	2	2.93	[91]
173	pH7 cal.300	91	0	10	7.0	0.0	6	0	2	3.10	[91]
174	pH7 cal.400	92	0	7	8.0	0.0	9	0	2	3.06	[91]
175	pH7 cal.600	96	0	3	15.0	0.0	8	0	2	3.02	[91]

Table 5.23: Dataset VI of Block B (continued of Table 5.18).

	Photocatalyst	%A	%R	%B	dA	dR	dB	CP	TT	Eg	*Ref*
176	pH7 cal.700	100	0	0	31.0	0.0	0	1	2	3.00	[91]
177	pH7 cal.800	7	93	0	39.0	55.4	0	0	2	2.90	[91]
178	pH8 cal.300	92	0	8	7.0	0.0	6	0	2	3.05	[91]
179	pH8 cal.400	96	0	4	9.0	0.0	9	0	2	3.03	[91]
180	pH8 cal.600	97	0	2	13.0	0.0	6	0	2	3.01	[91]
181	pH8 cal.700	100	0	0	27.0	0.0	0	1	2	2.98	[91]
182	pH8 cal.800	13	87	0	38.0	55.4	0	0	2	2.89	[91]
183	pH9 cal.300	91	0	8	9.0	0.0	6	0	2	3.04	[91]
184	pH9 cal.400	94	0	6	9.0	0.0	8	0	2	3.03	[91]
185	pH9 cal.600	97	0	2	14.0	0.0	6	0	2	3.01	[91]
186	pH9 cal.700	100	0	0	28.0	0.0	0	1	2	3.00	[91]
187	pH9 cal.800	38	62	0	39.0	55.4	0	0	2	2.90	[91]
188	TESI	88	12	0	13.4	15.3	0	1	1	3.22	[92]
189	TENI	5	95	0	18.3	30.6	0	1	1	3.32	[92]
190	TEPCI	79	21	0	15.2	18.3	0	1	1	3.25	[92]
191	TECI	100	0	0	15.2	0.0	0	1	1	3.26	[92]
192	TEAI	77	23	0	15.2	18.3	0	1	1	3.21	[92]
193	TESI	88	12	0	13.4	15.3	0	2	2	2.83	[92]
194	TENI	5	95	0	18.3	30.6	0	2	2	3.05	[92]
195	TEPCI	79	21	0	15.2	18.3	0	2	2	2.96	[92]
196	TEAI	77	23	0	15.2	18.3	0	2	2	2.77	[92]
197	R1 - 80	0	100	0	0.0	5.6	0	2	2	3.16	[93]
198	Figure 4e	100	0	0	14.9	0.0	0	1	1	3.35	[87]
199	Figure 6a1-2	100	0	0	25.0	0.0	0	1	1	3.30	[87]
200	Figure 4f	37	63	0	16.2	–	0	0	1	3.14	[87]
201	Figure 6b	53	47	0	19.2	–	0	0	1	3.22	[87]
202	Figure 5b	22	78	0	35.0	–	0	0	1	3.12	[87]
203	Figure 5c	90	10	0	15.1	–	0	0	1	3.30	[87]
204	Figure 4d	44	56	0	23.3	–	0	0	1	3.10	[87]
205	Figure 4c	0	100	0	0.0	30.2	0	2	1	2.99	[87]
206	Figure 4g	0	100	0	0.0	17.1	0	2	1	3.16	[87]
207	Figure 4h	0	100	0	0.0	21.7	0	2	1	3.13	[87]
208	P-25	70	30	0	20.0	–	0	0	1	3.01	[87]
209	TWPI	100	0	0	5.7	0.0	0	1	1	3.41	[94]
210	TWSI	100	0	0	17.1	0.0	0	1	1	3.33	[94]

Table 5.24: Dataset VII of Block B (continued of Table 5.18).

	Photocatalyst	%A	%R	%B	dA	dR	dB	CP	TT	Eg	*Ref*
211	TWNI	100	0	0	15.2	0.0	0	1	1	3.32	[94]
212	TWPCI	100	0	0	18.3	0.0	0	1	1	3.29	[94]
213	TWCI	100	0	0	15.2	0.0	0	1	1	3.46	[94]
214	TWAI	100	0	0	13.0	0.0	0	1	1	3.41	[94]
215	powder A-480	100	0	0	10.4	0.0	0	1	2	3.13	[95]
216	powder A -550	100	0	0	12.8	0.0	0	1	2	3.18	[95]
217	powder A-600	100	0	0	14.9	0.0	0	1	2	3.23	[95]
218	as-prepared SM-1	56	0	45	6.2	0.0	3	0	2	3.16	[96]
219	as-prepared SM-2	50	10	41	6.9	0.0	9	0	2	3.19	[96]
220	P25	80	20	0	37.0	90.0	0	0	2	3.08	[96]

Before few model attempts, we also noticed something that may have confused the recognition of ANN models. It was another measurement by literature issue: the technique used for crystallite size. As the Scherrer equation was far more employed, we included corresponding groups that only have data from it, that is, without the data value from Rietveld refinement.

The groups arrangement considered the interference of rutile and brookite phases as input parameters and the influence of XRD measurement with only Scherrer equation (groups S). Remembering that we used other ANN types in this Block.

5.3.1
Block B - Group I

This set has 173 vectors (Tables 5.18 to 5.24), 8 inputs, and one output, getting a matrix of variables and vectors of 1557 contents. The training data has 140 photocatalysts. Were developed 216 topologies for this group, where on Table 5.25 shows fifteen of them according to the highest R^2_{train}.

This group had low SSE (around 1), a good adjustment for training (more than 80 %) and a bad for the test (almost null). The first three had SSE smaller than one, a cascade network with trainlm and logsig for the transfer function on the first hidden layer. Moreover, the number of hidden neurons were near the maximum as possible without error.

Table 5.25: Results of Group I (% A, % R, % B, dA, dR, dB, CP, TT) from Block B with the highest R^2_{train}.

#	Type	Alg.	F1	N1	Fy	SSE	R^2_{train}	R^2_{test}
1	CF	trainlm	logsig	13	purelin	0.828	0.885	0.001
2	CF	trainlm	logsig	13	tansig	0.861	0.880	0.001
3	CF	trainlm	logsig	11	tansig	0.885	0.877	0.009
4	FF	trainlm	logsig	12	tansig	0.998	0.861	0.010
5	ELM	trainlm	tansig	13	purelin	1.009	0.859	0.026
6	ELM	trainlm	tansig	12	purelin	1.011	0.859	0.000
7	ELM	trainlm	tansig	13	tansig	1.021	0.858	0.016
8	FF	trainlm	tansig	13	tansig	1.022	0.858	0.012
9	CF	trainlm	tansig	12	purelin	1.035	0.856	0.000
10	ELM	trainlm	logsig	12	tansig	1.058	0.853	0.012
11	CF	trainlm	tansig	13	purelin	1.059	0.852	0.017
12	ELM	trainlm	tansig	11	tansig	1.061	0.852	0.02
13	FF	trainlm	logsig	13	purelin	1.067	0.851	0.009
14	CF	trainlm	logsig	12	purelin	1.069	0.851	0.012
15	ELM	trainlm	logsig	10	purelin	1.074	0.850	0.044

5.3.2
Block B - Group II

This set has 183 vectors (Tables 5.18 to 5.24), 6 inputs, and one output, getting a matrix of variables and vectors of 1241 contents. The training data has 148 photocatalysts. Were developed 465 topologies for this group, where on Table 5.14 shows fifteen of them according to the highest R^2_{train}.

This group had a small improvement from Group I. Tansig was the transfer function used on topologies with the highest R^2_{train} and ELM network also well adjusted.

Table 5.26: Results of Group II (% A, % R, dA, dR, CP, TT) from Block B with the highest R^2_{train}.

#	Type	Alg.	F1	N1	Fy	SSE	R^2_{train}	R^2_{test}
1	CF	trainlm	tansig	18	purelin	0.839	0.892	0.018
2	ELM	trainlm	tansig	17	purelin	0.840	0.892	0.000
3	ELM	trainlm	tansig	18	tansig	0.861	0.889	0.002
4	FF	trainlm	tansig	18	purelin	0.867	0.888	0.006
5	ELM	trainlm	logsig	17	tansig	0.875	0.887	0.039
6	CF	trainlm	logsig	18	purelin	0.888	0.885	0.001
7	CF	trainlm	logsig	18	tansig	0.888	0.885	0.024
8	ELM	trainlm	tansig	18	purelin	0.895	0.885	0.023
9	ELM	trainlm	tansig	15	tansig	0.895	0.885	0.000
10	ELM	trainlm	tansig	15	purelin	0.901	0.884	0.000
11	ELM	trainlm	tansig	16	tansig	0.914	0.882	0.024
12	ELM	trainlm	logsig	17	purelin	0.916	0.882	0.004
13	CF	trainlm	tansig	16	tansig	0.923	0.881	0.010
14	FF	trainlm	logsig	17	tansig	0.930	0.880	0.008
15	ELM	trainlm	tansig	17	tansig	0.954	0.877	0.002

5.3.3
Block B - Group III

This set has 220 vectors (Tables 5.18 to 5.24), 4 inputs, and one output, getting a matrix of variables and vectors of 1100 contents. The training data has 177 photocatalysts. Were developed 465 topologies for this group, where on Table 5.14 shows fifteen of them according to the highest R^2_{train}.

As the previous results of Block B, this group had a small improvement. But now there is not an agreement with the best network type and transfer function.

Table 5.27: Results of Group III (% A, dA, CP, TT) from Block B with the highest R^2_{train}.

#	Type	Alg.	F1	N1	Fy	SSE	R^2_{train}	R^2_{test}
1	ELM	trainlm	tansig	28	tansig	0.831	0.905	0.006
2	CF	trainlm	logsig	24	purelin	0.833	0.905	0.004
3	ELM	trainlm	tansig	28	purelin	0.842	0.904	0.016
4	ELM	trainlm	tansig	26	tansig	0.846	0.904	0.001
5	CF	trainlm	tansig	28	purelin	0.850	0.903	0.026
6	FF	trainlm	logsig	26	purelin	0.856	0.902	0.023
7	ELM	trainlm	tansig	26	purelin	0.861	0.902	0.017
8	FF	trainlm	logsig	24	purelin	0.873	0.901	0.026
9	CF	trainlm	tansig	26	purelin	0.891	0.899	0.034
10	FF	trainlm	logsig	26	tansig	0.894	0.898	0.011
11	CF	trainlm	logsig	28	purelin	0.896	0.898	0.010
12	CF	trainlm	logsig	26	purelin	0.933	0.894	0.000
13	ELM	trainlm	logsig	22	purelin	0.935	0.893	0.048
14	FF	trainlm	tansig	22	purelin	0.936	0.893	0.002
15	CF	trainlm	logsig	28	tansig	0.943	0.893	0.005

5.3.4
Block B - Group IV

This set has 220 vectors (Tables 5.18 to 5.24), 3 inputs, and one output, getting a matrix of variables and vectors of 880 contents. The training data has 177 photocatalysts. Were developed 612 topologies for this group, where on Table 5.14 shows fifteen of them according to the highest R^2_{train}.

This group shows a decay on the coefficients results.

Table 5.28: Results of Group IV (% A, dA, CP) from Block B with the highest R^2_{train}.

#	Type	Alg.	F1	N1	Fy	SSE	R^2_{train}	R^2_{test}
1	FF	trainlm	tansig	29	tansig	1.429	0.837	0.004
2	CF	trainlm	tansig	33	tansig	1.436	0.836	0.000
3	CF	trainlm	tansig	33	purelin	1.458	0.834	0.002
4	CF	trainlm	tansig	31	purelin	1.466	0.833	0.020
5	CF	trainlm	logsig	25	tansig	1.543	0.824	0.016
6	FF	trainlm	tansig	35	purelin	1.544	0.824	0.016
7	CF	trainlm	logsig	29	purelin	1.560	0.822	0.000
8	CF	trainlm	logsig	27	tansig	1.586	0.819	0.013
9	FF	trainlm	logsig	25	tansig	1.616	0.816	0.001
10	FF	trainlm	logsig	35	purelin	1.617	0.816	0.006
11	ELM	trainlm	tansig	19	tansig	1.630	0.814	0.008
12	ELM	trainlm	tansig	21	tansig	1.709	0.805	0.026
13	CF	trainlm	logsig	17	purelin	1.756	0.800	0.001
14	FF	trainlm	logsig	29	purelin	1.763	0.799	0.034
15	CF	trainlm	tansig	21	tansig	1.780	0.797	0.001

5.3.5
Block B - Group V

This set has 220 vectors (Tables 5.18 to 5.24), 3 inputs, and one output, getting a matrix of variables and vectors of 880 contents. The training data has 177 photocatalysts. Were developed 612 topologies for this group, where on Table 5.14 shows fifteen of them according to the highest R^2_{train}.

This group also shows a decay on the coefficients results, but better than group IV. Thus, the variables **TT** support the modelling adjustment and improve the response when they are used together. The improvement of the coefficients without the information of rutile and brookite phases (group III) suggests they do not improve the fitting.

Table 5.29: Results of Group V (% A, dA, TT) from Block B with the highest R^2_{train}.

#	Type	Alg.	F1	N1	Fy	SSE	R^2_{train}	R^2_{test}
1	FF	trainlm	logsig	35	purelin	1.293	0.853	0.011
2	FF	trainlm	logsig	35	tansig	1.300	0.852	0.006
3	CF	trainlm	logsig	35	purelin	1.312	0.850	0.004
4	ELM	trainlm	tansig	35	purelin	1.313	0.850	0.003
5	ELM	trainlm	tansig	33	purelin	1.322	0.849	0.009
6	CF	trainlm	logsig	33	tansig	1.331	0.848	0.001
7	ELM	trainlm	tansig	25	tansig	1.340	0.847	0.005
8	ELM	trainlm	logsig	33	tansig	1.344	0.847	0.011
9	CF	trainlm	tansig	35	purelin	1.350	0.846	0.000
10	CF	trainlm	tansig	33	purelin	1.356	0.846	0.001
11	FF	trainlm	tansig	35	tansig	1.356	0.845	0.000
12	CF	trainlm	tansig	31	purelin	1.361	0.845	0.006
13	FF	trainlm	tansig	31	purelin	1.361	0.845	0.014
14	FF	trainlm	tansig	35	purelin	1.364	0.845	0.004
15	FF	trainlm	logsig	33	purelin	1.365	0.845	0.000

5.3.6
Block B - Group SI

This set has 149 vectors (Tables 5.18 to 5.24), 8 inputs, and one output, getting a matrix of variables and vectors of 1341 contents. The training data has 119 photocatalysts. Were developed 112 topologies for this group, where on Table 5.14 shows fifteen of them according to the highest R^2_{train}.

This group had a slightly worse result than group I. Although the low adjustment of the test, there appears a better R^2_{test}, as # 9 with 0.353. Th highest R^2_{test} was 0.392 with 0.827 for training, SSE = 1.144, topology **ELM 8-10-1 trainlm, tansig, purelin**.

Table 5.30: Results of Group SI (% A, % R, % B, dA, dR, dB, CP, TT) from Block B with the highest R^2_{train}.

#	Type	Alg.	F1	N1	Fy	SSE	R^2_{train}	R^2_{test}
1	ELM	trainlm	tansig	11	purelin	0.895	0.865	0.046
2	CF	trainlm	logsig	11	tansig	0.990	0.850	0.001
3	ELM	trainlm	logsig	10	tansig	1.049	0.841	0.016
4	CF	trainlm	logsig	9	tansig	1.052	0.841	0.235
5	FF	trainlm	tansig	11	tansig	1.056	0.840	0.279
6	FF	trainlm	logsig	11	tansig	1.058	0.840	0.032
7	FF	trainlm	logsig	9	tansig	1.065	0.839	0.007
8	CF	trainlm	logsig	11	purelin	1.072	0.838	0.035
9	ELM	trainlm	logsig	9	purelin	1.073	0.838	0.353
10	CF	trainlm	tansig	11	tansig	1.075	0.837	0.006
11	ELM	trainlm	logsig	11	tansig	1.077	0.837	0.143
12	CF	trainlm	tansig	10	tansig	1.080	0.837	0.000
13	ELM	trainlm	logsig	11	purelin	1.091	0.835	0.131
14	ELM	trainlm	logsig	9	tansig	1.109	0.832	0.028
15	ELM	trainlm	tansig	9	tansig	1.120	0.831	0.013

5.3.7
Block B - Group SII

This set has 163 vectors (Tables 5.18 to 5.24), 6 inputs, and one output, getting a matrix of variables and vectors of 1141 contents. The training data has 130 photocatalysts. Were developed 397 topologies for this group, where on Table 5.14 shows fifteen of them according to the highest R^2_{train}.

This group had a small improvement from Group SI. The highest R^2_{test} was 0.531, with R^2_{train} = 0.825, SSE = 1.261, for topology **ELM 6-11-1 trainlm, logsig, tansig**.

Table 5.31: Results of Group SII (% A, % R, dA, dR, CP, TT) from Block B with the highest R^2_{train}.

#	Type	Alg.	F1	N1	Fy	SSE	R^2_{train}	R^2_{test}
1	ELM	trainlm	tansig	16	tansig	0.800	0.889	0.173
2	CF	trainlm	logsig	15	purelin	0.853	0.881	0.199
3	ELM	trainlm	tansig	16	purelin	0.867	0.879	0.003
4	ELM	trainlm	tansig	15	tansig	0.902	0.874	0.020
5	FF	trainlm	tansig	15	purelin	0.904	0.874	0.048
6	ELM	trainlm	logsig	16	purelin	0.915	0.873	0.144
7	ELM	trainlm	tansig	15	purelin	0.923	0.872	0.072
8	CF	trainlm	tansig	16	tansig	0.936	0.870	0.005
9	ELM	trainlm	logsig	15	tansig	0.950	0.868	0.072
10	ELM	trainlm	logsig	16	tansig	0.951	0.868	0.000
11	FF	trainlm	tansig	14	purelin	0.967	0.865	0.062
12	ELM	trainlm	tansig	11	tansig	0.976	0.864	0.032
13	CF	trainlm	tansig	15	purelin	0.980	0.864	0.013
14	FF	trainlm	logsig	16	purelin	0.987	0.863	0.207
15	CF	trainlm	logsig	13	tansig	0.990	0.862	0.014

5.3.8
Block B - Group SIII

This set has 191 vectors (Tables 5.18 to 5.24), 4 inputs, and one output, getting a matrix of variables and vectors of 955 contents. The training data has 154 photocatalysts. Were developed 397 topologies for this group, where on Table 5.14 shows fifteen of them according to the highest R^2_{train}.

This group had a small improvement from Group SII, but it has lower test coefficients. Where the highest could validate 48.3 % (test) of only 29.8 % adjustment of the training, with a high SSE 5.692 (topology **CF 4-10-1 trainbr, logsig, tansig**.

Table 5.32: Results of Group SIII (% A, dA, CP, TT) from Block B with the highest R^2_{train}.

#	Type	Alg.	F1	N1	Fy	SSE	R^2_{train}	R^2_{test}
1	CF	trainlm	logsig	24	purelin	0.803	0.901	0.164
2	CF	trainlm	tansig	24	purelin	0.805	0.901	0.012
3	FF	trainlm	logsig	22	tansig	0.859	0.894	0.002
4	ELM	trainlm	tansig	24	tansig	0.860	0.894	0.077
5	CF	trainlm	logsig	24	tansig	0.870	0.893	0.007
6	FF	trainlm	logsig	24	purelin	0.870	0.893	0.109
7	ELM	trainlm	tansig	20	purelin	0.882	0.891	0.047
8	ELM	trainlm	tansig	24	purelin	0.905	0.888	0.153
9	FF	trainlm	logsig	20	tansig	0.905	0.888	0.162
10	FF	trainlm	logsig	24	tansig	0.906	0.889	0.031
11	FF	trainlm	logsig	20	purelin	0.914	0.887	0.090
12	CF	trainlm	tansig	22	tansig	0.928	0.886	0.002
13	ELM	trainlm	tansig	18	purelin	0.962	0.881	0.014
14	ELM	trainlm	logsig	24	purelin	0.965	0.881	0.000
15	FF	trainlm	tansig	24	purelin	0.965	0.881	0.220

5.3.9
Block B - Group SIV

This set has 196 vectors (Tables 5.18 to 5.24), 3 inputs, and one output, getting a matrix of variables and vectors of 784 contents. The training data has 156 photocatalysts. Were developed 540 topologies for this group, where on Table 5.14 shows fifteen of them according to the highest R^2_{train}.

This group also shows a decay on the coefficients results, just the same that happened on Group IV.

Table 5.33: Results of Group SIV (% A, dA, CP) from Block B with the highest R^2_{train}.

#	Type	Alg.	F1	N1	Fy	SSE	R^2_{train}	R^2_{test}
1	CF	trainlm	tansig	25	tansig	1.485	0.817	0.312
2	CF	trainlm	tansig	29	purelin	1.501	0.815	0.000
3	FF	trainlm	tansig	31	tansig	1.534	0.811	0.010
4	CF	trainlm	tansig	23	purelin	1.538	0.810	0.000
5	CF	trainlm	logsig	29	tansig	1.562	0.807	0.081
6	CF	trainlm	logsig	25	tansig	1.593	0.803	0.002
7	FF	trainlm	logsig	23	purelin	1.621	0.800	0.138
8	ELM	trainlm	tansig	19	purelin	1.626	0.799	0.003
9	CF	trainlm	tansig	21	tansig	1.660	0.795	0.029
10	ELM	trainlm	tansig	21	tansig	1.683	0.792	0.016
11	FF	trainlm	logsig	19	purelin	1.707	0.789	0.009
12	FF	trainlm	tansig	19	tansig	1.729	0.787	0.031
13	FF	trainlm	tansig	11	tansig	1.746	0.785	0.121
14	CF	trainlm	tansig	15	tansig	1.781	0.780	0.000
15	FF	trainlm	logsig	19	tansig	1.794	0.779	0.189

5.3.10
Block B - Group SV

This set has 196 vectors (Tables 5.18 to 5.24), 3 inputs, and one output, getting a matrix of variables and vectors of 784 contents. The training data has 156 photocatalysts. Were developed 540 topologies for this group, where on Table 5.14 shows fifteen of them according to the highest R^2_{train}.

This group had an improvement again, with the highest results of R^2_{train} of Block B. However, the R^2_{test} was low too, where the highest could adjust only 42.8 % (test) of 28.3 % for training, with a high SSE 5.01 from topology **ELM 3-3-1 trainlm, tansig, tansig**.

Table 5.34: Results of Group SV (% A, dA, TT) from Block B with the highest R^2_{train}.

#	Type	Alg.	F1	N1	Fy	SSE	R^2_{train}	R^2_{test}
1	CF	trainlm	tansig	31	purelin	0.744	0.908	0.001
2	ELM	trainlm	tansig	31	purelin	0.813	0.900	0.006
3	ELM	trainlm	tansig	27	purelin	0.823	0.898	0.000
4	FF	trainlm	logsig	31	purelin	0.830	0.898	0.019
5	ELM	trainlm	logsig	31	tansig	0.831	0.898	0.107
6	CF	trainlm	logsig	31	tansig	0.865	0.893	0.016
7	CF	trainlm	logsig	31	purelin	0.870	0.893	0.002
8	ELM	trainlm	tansig	29	purelin	0.882	0.891	0.009
9	CF	trainlm	tansig	27	purelin	0.904	0.888	0.018
10	ELM	trainlm	tansig	31	tansig	0.907	0.888	0.098
11	CF	trainlm	logsig	29	purelin	0.910	0.888	0.002
12	CF	trainlm	logsig	29	tansig	0.924	0.886	0.000
13	FF	trainlm	tansig	31	purelin	0.928	0.885	0.019
14	FF	trainlm	tansig	29	purelin	0.933	0.885	0.021
15	ELM	trainlm	tansig	25	purelin	0.937	0.884	0.005

In order to compare the results, we summarized the highest results of each group on Table 5.35. We highlighted the cells with the highest coefficients of R^2 and the lowest SSE.

Table 5.35: The best topologies of each group: SSE, R^2 results.

Group	Type	Alg.	F1	N1	Fy	SSE	R^2_{train}	R^2_{test}
I	CF	trainlm	logsig	13	purelin	0.828	0.885	0.001
II	CF	trainlm	tansig	18	purelin	0.839	0.892	0.018
III	ELM	trainlm	tansig	28	tansig	0.831	0.905	0.006
IV	FF	trainlm	tansig	29	tansig	1.429	0.837	0.004
V	FF	trainlm	logsig	35	purelin	1.293	0.853	0.011
SI	ELM	trainlm	tansig	11	purelin	0.895	0.865	0.046
SII	ELM	trainlm	tansig	16	tansig	0.800	0.889	0.173
SIII	CF	trainlm	logsig	24	purelin	0.803	0.901	0.164
SIV	CF	trainlm	tansig	25	tansig	1.485	0.817	0.312
SV	CF	trainlm	tansig	31	purelin	0.744	0.908	0.001

We noticed that groups **S** had better coefficients, implying that values from the same technique have more accordance. Neither the rutile nor the brookite phases had a significant effect on the prediction, maybe because they are not as studied as anatase phase. If you have less report, less you know about this variable, notably for brookite phase [59, 76]. The influence of less information of a parameter in a network is also reported on article Yildirim, 2011 [97] with the variable of Temperature. On the other hand, CP and TT variables changed the models.

By far trainlm was the best algorithm, but transfer functions varied for each result. We expected that trainbr could have adjusted better, according to its use and success on literature. The behaviour of model topologies evaluation and the number of hidden neurons are shown on Figure 5.6 for the best result, group SIII. Except for specific combinations, trainlm (the middle yellow bar) had the smallest SSE with a high number of hidden neurons (higher than 18 neurons).
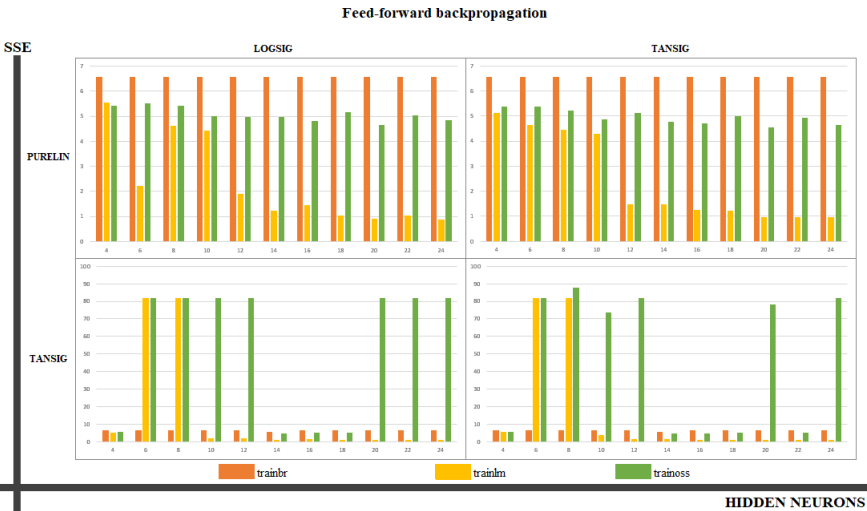
5.6(a): FF
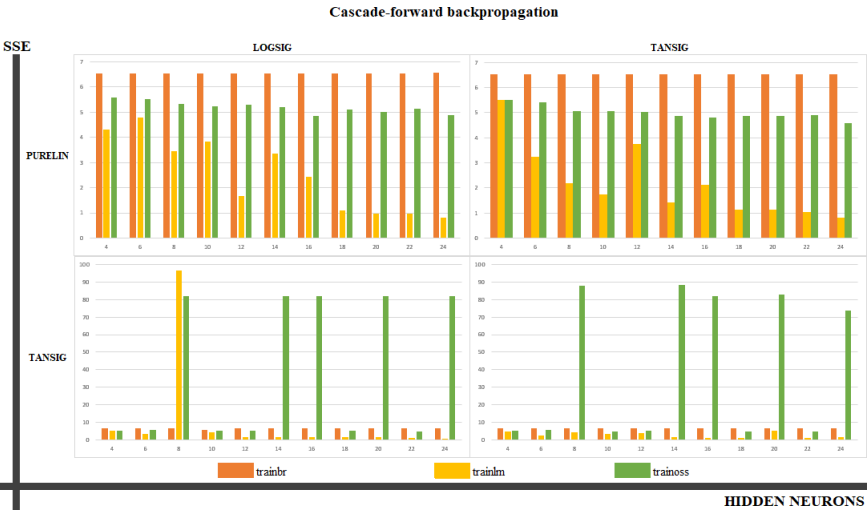
5.6(b): CF
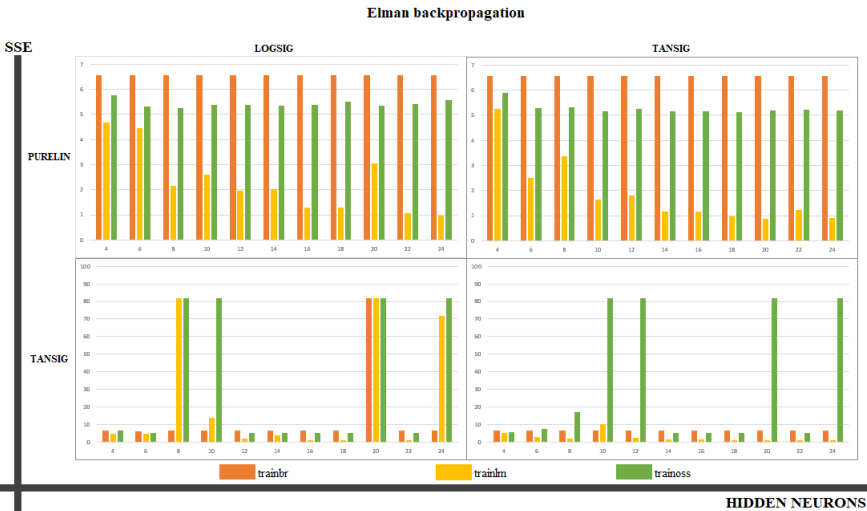
5.6(c): ELM

Figure 5.6: SSE performance for hidden neurons numbers of Group SIII of Block B.

Even though group SIII had the best result (high SSE and R^2 train), it presented a bad adjustment to the test dataset (low R^2 test). Both linear and angular coefficients of the training had good adjustment, however the test data has diverged and the output predicted was negative, having no physical meaning (Figure 5.7).
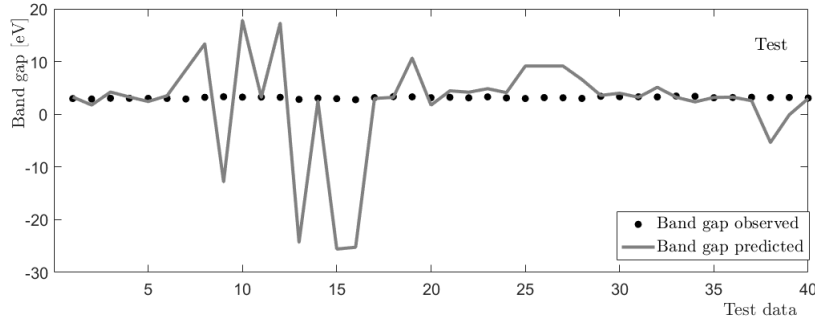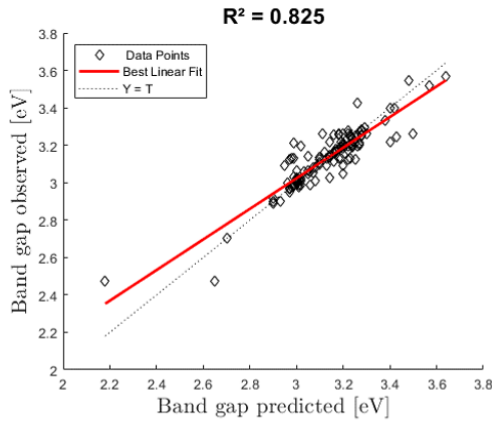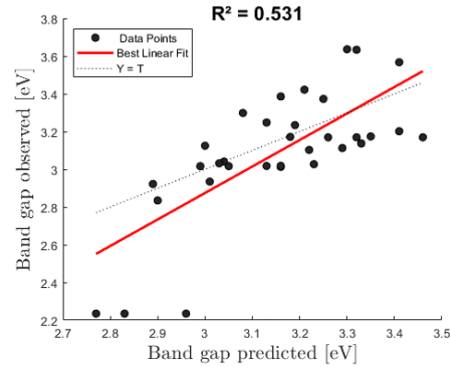

Figure 5.7: Prediction behaviour of Group SIII of Block B.

The group SII's network of **ELM 6-11-1 trainlm, logsig, tansig** topology had an interesting adjustment, showing a SSE = 1.21 and $R^2 =$ 82.5 % for training and $R^2 = 53.1$ % for test. Its regression diagrams are shown on Figure 5.8. The training shows a good adjustment, but the test is very dispersed around the best linear fit line.

5.8(a): Training

5.8(b): Test

Figure 5.8: Regression diagram of **ELM 6-11-1 trainlm, logsig, tansig** Group SII, Block B.

Figure 5.9 shows the datasets' prediction behaviour. There are some inconsistencies between the training and the test, such as points 8, 12, 14, 15, 18 of test dataset because their predicted values were the network value limits.
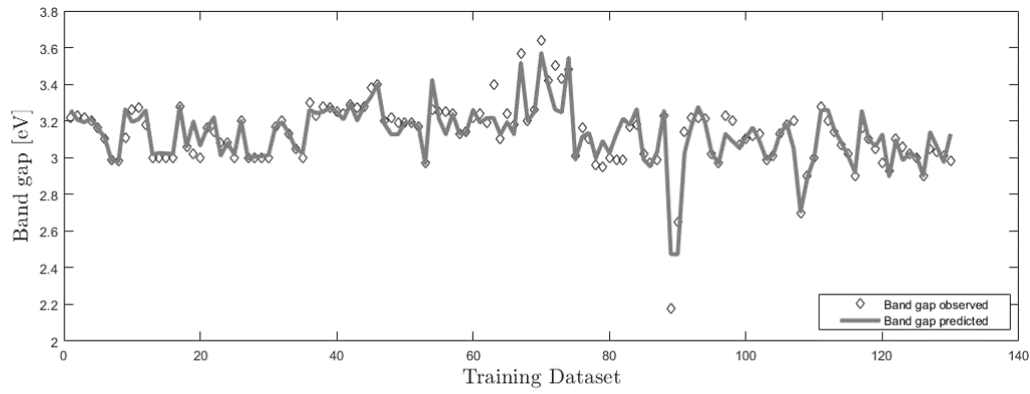
5.9(a): Training
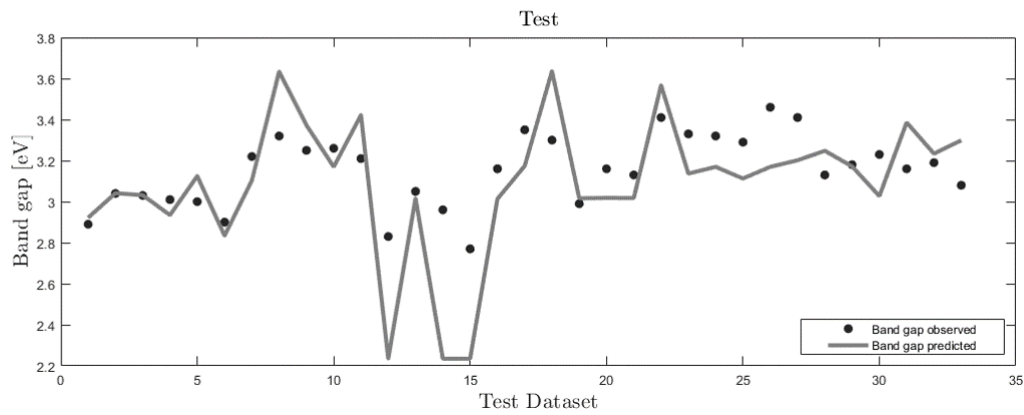
5.9(b): Test

Figure 5.9: Prediction behaviour of **ELM 6-11-1 trainlm, logsig, tansig** Group SII, Block B.

It can also be noticed that even though the training behaviour seems to have connected points, some of them were not able to be predicted by the network. Such as points 63, 67, 70, 72, 82, 89. On the other hand, the test seems to have abrupt behaviour, and the set was not well predicted.

5.3.11
Block B multilayer

The Group SIII was investigated with more hidden layers, which six results with the highest coefficients of two and three hidden layers are shown on Table 5.36).

Table 5.36: The third best topologies of group SIII of Block B with more hidden layers.

Type	F1	N1	F2	N2	Fy	SSE	R^2_{train}	R^2_{test}
CF	logsig	4	tansig	6	purelin	2.238	0.843	0.507
CF	tansig	4	logsig	4	purelin	3.770	0.735	0.504
FF	logsig	6	logsig	4	tansig	3.199	0.775	0.465

(a) Two hidden layers

| Type	F1	N1	F2	N2	F3	N3	Fy	SSE	Train	Test
CF	logsig	4	logsig	6	tansig	8	tansig	1.353	0.905	0.444
FF	logsig	6	tansig	6	logsig	8	purelin	1.309	0.908	0.341
CF	logsig	4	logsig	6	logsig	10	purelin	0.787	0.945	0.334

(b) Three hidden layers

We investigated the regression of observed and predicted values of the highest coefficients of both training and test, shown on Figures 5.10, 5.11 and 5.12.

The band gap regression diagram shows a dispersion on both training and test, despite of having a lot of training points well fitted (on Figure 5.10).
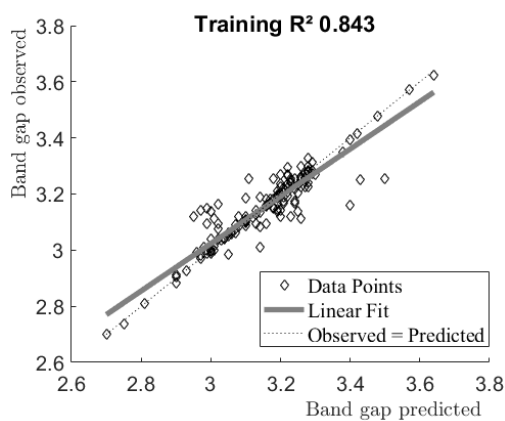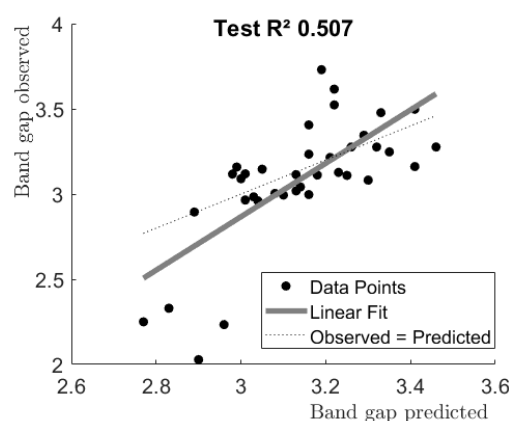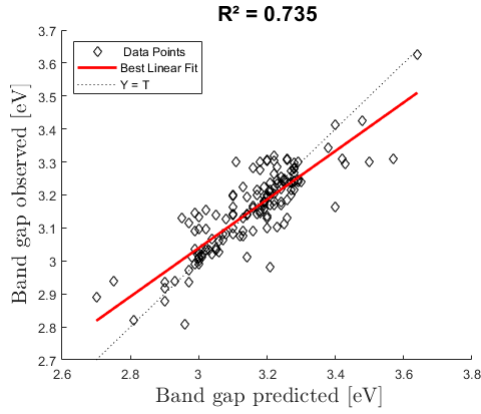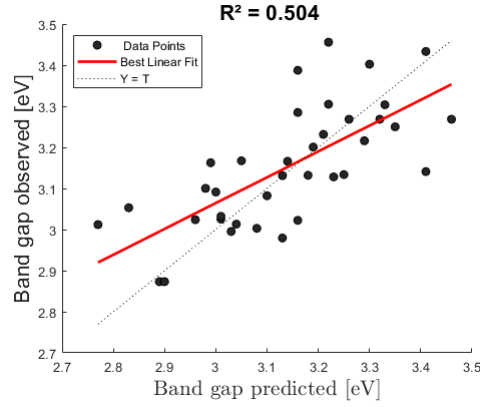

5.10(a): Training   5.10(b): Test

Figure 5.10: Regression diagram of **CF 4-4-6-1 trainlm, logsig, tansig, purelin** Group SIII, Block B.

The Figure 5.11 shows that the values are more disperse than CF 4-4-6-1 topology (Figure 5.10).
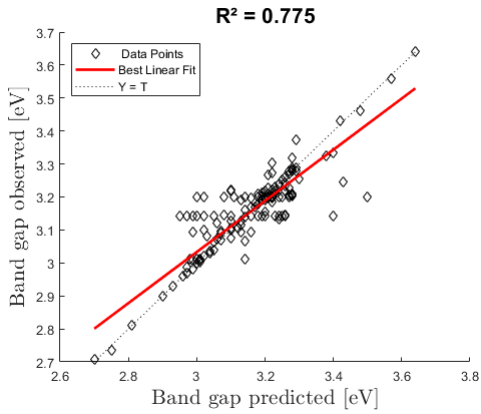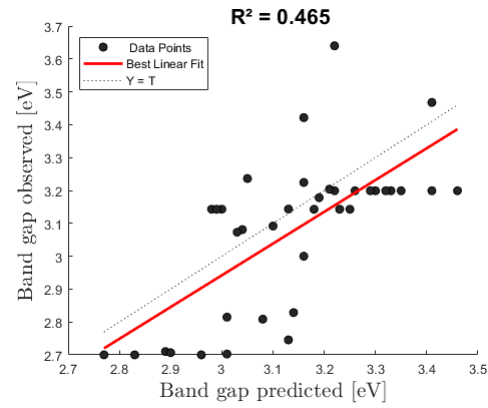
5.11(a): Training   5.11(b): Test

Figure 5.11: Regression diagram of **CF 4-4-4-1 trainlm, tansig, logsig, purelin** Group SIII, Block B.

The Figure 5.12 shows that it is the worst fitting than the three we have just analysed. We notice here again the tendency of horizontal points.

5.12(a): Training   5.12(b): Test

Figure 5.12: Regression diagram of **FF 4-6-4-1 trainlm, logsig, logsig, tansig** Group SIII, Block B.

The Figure 5.12 shows all training regression diagrams together. The CF 4-4-4-1 network is less accurate than the other two, and the FF 4-6-4-1 is more disperse than the CF 4-4-6-1, which seems to be the most adjusted network.

From Figure 5.14, the prediction behaviour reveals a coherent band gap adjustment and limits, scale 2 to 3.8 eV for the test. However, this network is able to predict only half of the new information. The model slightly follows the behaviour of the band gap value and disagrees in three major points: 7th, 11th and 37th. As the system behavior is the first achievement of modelling, this result reveals the potential of this study.
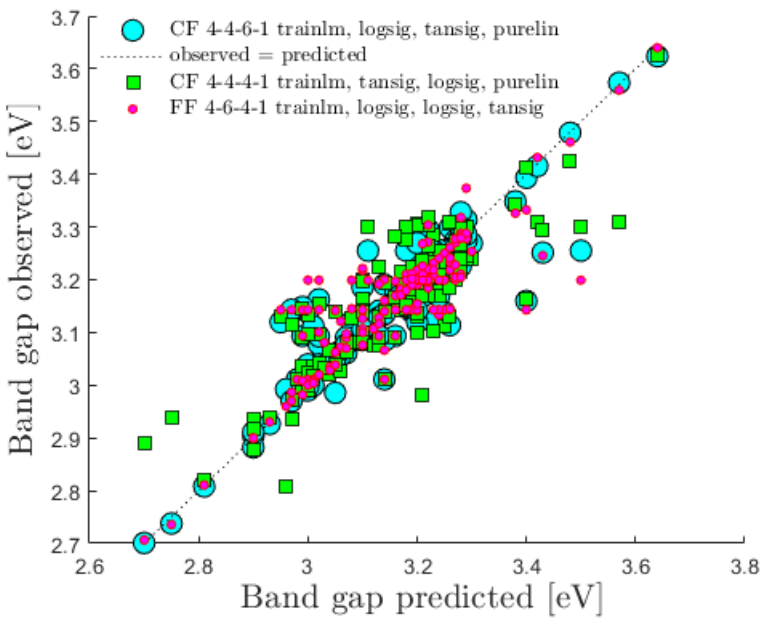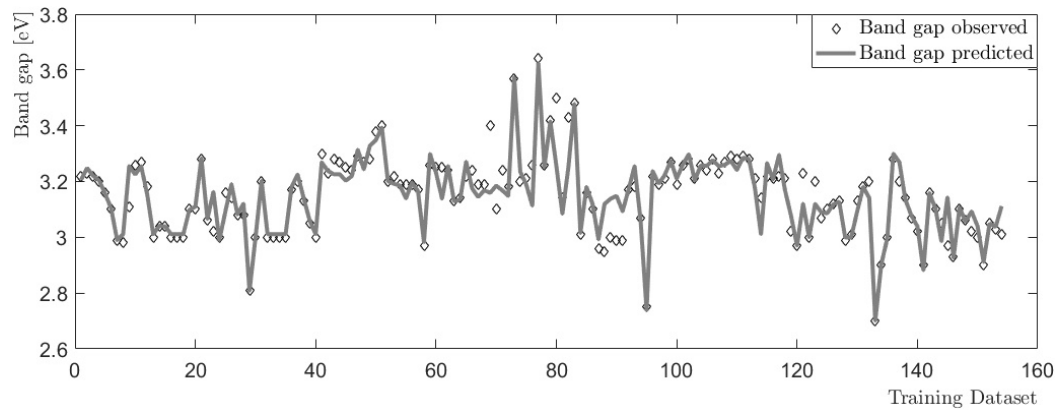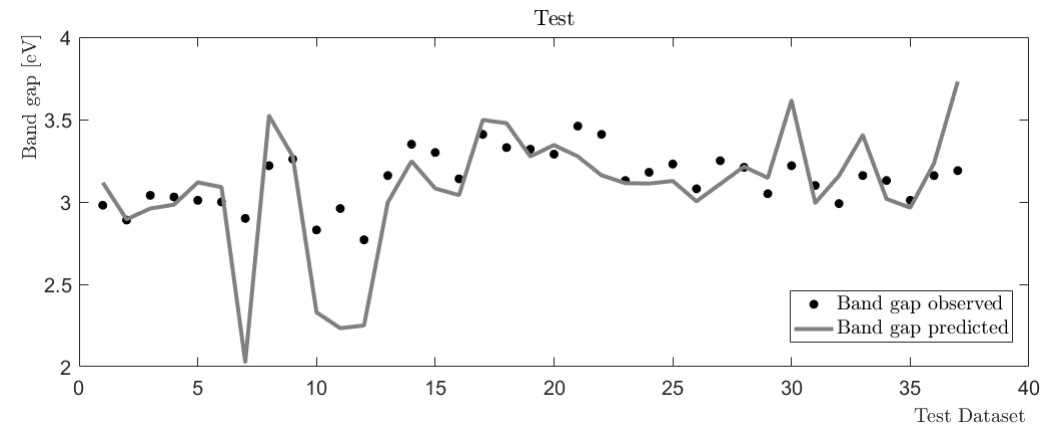
Figure 5.13: Regression diagrams comparison for Block B multilayers networks.
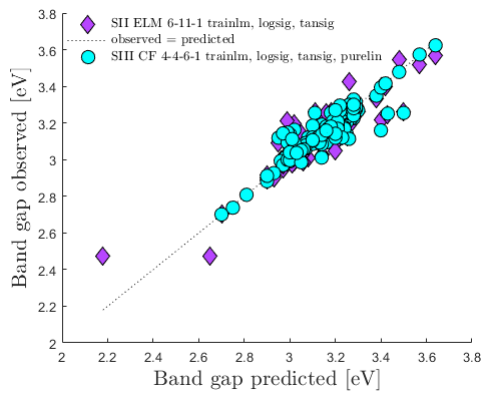

5.14(a): Training

5.14(b): Test

Figure 5.14: Prediction behaviour of **CF 4-4-6-1 trainlm, logsig, tansig, purelin** Group SIII, Block B.

Thus, the results of group SII ELM 6-11-1 and group SIII CF 4-4-6-1 can be compared. The regression diagram (Figure 5.15 of training shows both networks are well adjusted, but the SII seems to have sparser points. The test regression shows both did not predicted well, and the SII network seems to have horizontal lines of data dispersion.
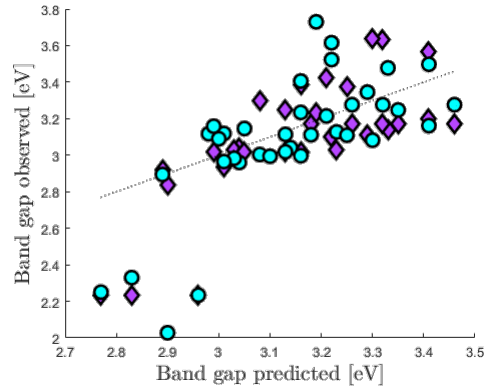
5.15(a): Training   5.15(b): Test

Figure 5.15: Regression diagrams comparison of groups SII (diamond) and SIII (circle) networks.

Furthermore, the networks (SII and SIII) had the same behaviour in similar points that could not be predicted in both cases. However, the SIII network behaviour is softer, maybe because it has two hidden layers. The strategy of a multilayer network improved the coefficients. Moreover, this network has 154 training vectors, which is larger than SII ELM 6-11-1 dataset with 130 training vectors. Therefore, the network of topology **CF 4-4-6-1 trainlm, logsig, tansig, purelin** is the most adjusted model. Its weights and biases are shown below in Table 5.37.

Nevertheless, the model with the highest coefficients of Block B multilayer could not be validated because its test correlation coefficient has failed ($R^2_{test} = 50.7$ %). Considering the exhaustive modelling investigation and the disparity of literature reports, it was considered worthy the discussion of the characterization techniques.

There is no common sense or standard evaluation of the synthesis and characterization of TiO_2, especially the measurement of the band gap. There are researches that use DRS with different techniques namely as Kubelka-Munk [26, 82], Tauc plot or modified Kubelka-Munk[54, 62] while other researches employ the information directly from the Absorption Spectra [52, 53]. Even though the first and the second techniques can be used to classify

Table 5.37: Weights and biases of **CF 4-4-6-1 trainlm, logsig, tansig, purelin** Group SIII, Block B.

	biases	neuron	%A	dA	CP	TT
Hidden 1	-4.589	**1**	-2.020	-4.261	-0.434	-2.094
	-0.756	**2**	-0.491	2.808	0.892	-1.184
	-0.709	**3**	5.891	-3.128	4.028	0.719
	11.450	**4**	-5.542	14.850	0.509	6.754
Hidden 2	-30.035	**1**	16.997	-3.680	12.726	2.526
	1.628	**2**	-15.303	12.555	-1.363	-23.342
	-18.498	**3**	12.809	5.291	-0.170	-8.804
	5.592	**4**	22.598	1.829	-14.560	3.399
	-8.574	**5**	-1.294	-12.546	-3.318	-3.211
	0.029	**6**	-4.092	-3.885	0.777	-4.131
Output	-1.957	**1**	2.313	0.824	-1.252	0.509

	neuron	1	2	3	4
Hidden 1	**1**	59.866	12.082	1.934	23.293
	2	-22.808	-53.428	-7.197	-2.545
x	**3**	20.677	0.126	8.806	15.771
	4	-29.269	39.188	-25.969	-7.282
Hidden 2	**5**	-13.689	39.370	1.239	-1.416
	6	-5.819	-2.529	-1.924	3.755
Hidden 1 x Output	**1**	3.558	4.568	4.699	-1.593

Hidden 2 x Output

neuron	1	2	3	4	5	6
1	-0.728	1.724	-1.042	-0.460	-1.226	1.887

the transition type of the material as direct or indirect, allowed or forbidden, this matter was not always addressed in the scientific reports [26, 83].

Besides, some inconsistencies were noticed, such as authors [34, 54, 72] which have measured the direct band gap though the Modified Kubelka-Munk for pure anatase phase, but considered it having indirect band gap.

It is noteworthy, in general, the values obtained are not reported with their errors involved.

TiO$_2$ phases influence on the photocatalytic performance [22, 23, 50, 49], due to the indirect band gap of anatase phase and direct band gap of rutile phase. Further, the P25 shows different amounts of anatase and rutile [28, 30, 38]. Though there is a lot of debate about it [23, 98], no mathematical explanation was found. Therefore, it is important to analyse it properly.

In López and Gómez [38], the size effect (for Nano and Bulk dimensions), the phase aspect (with P25 and pure anatase synthesized) and the band gap evaluation (with Absorption, Kubelka-Munk, Tauc-plot measurements) were investigated, showing slight changes. The results consolidate the importance

of considering an appropriate type of transition. For instance, the Tauc plot with indirect allowed transition is the most used. It has an accurate result for the bandgap of TiO_2 synthesized by the sol-gel method and for the commercial P25.

The approach of Owolabi and Gondal [14] was quite similar to the present work. They used neural models to predict the band gap of doped titanium dioxide. The input variables was also a photocatalyst characteristic, the crystal lattice distortion, represented as the lattice parameters (a,c). All data were taken from literature and they used a statistical analysis to support. It is reported a good adjustment from the model. But it only discussed the error value (root mean square error (RMSE) of 13.13 %) and did not mention the correlation coefficients. The RMSE considering the best topology for group SIII, with SSE 2.238 and 154 training variables, is 12.0 %, and for group SII (with SSE 1.21 and 130 variables) is 9.6 %, both are lower than the Owolabi paper, showing that only the error does not represent the network adjustment. The present study explored more carefully ANN tool, with computational and mathematical criteria, such as ANN types and a larger database.

5.4
Critical analysis

The benefit of our methodology was to explore several interconnection structures, with and without recurrence network, using backpropagation that allows the minimization of error in a more efficient way than classical methods of modelling. Thus, we could exhaustive explore mathematical models through the combinations of the ANN type, transfer functions, number of hidden layers, training algorithm, number of hidden neurons, number of input parameters. A total of 4943 topologies were explored.

The model network is directly connected to the supervised dataset. Thinking about the nature of catalysis be inconstant, the learning rule for pattern recognition is a challenge that we could not achieve. It might have happened because this type of model requires a more accurate implementation of the physical-chemical characteristics due to that non classical nature. Or also a missing crystal characteristic, such as lattice parameter distortion. Since a parameter that could adjust the network is not evident, it should be further investigated.

Using literature data have advantages and disadvantages points. The advantages are that the evaluation can be of diverse experimental data and does not depend on laboratory analysis. Despite being an arduous work to collect manually each information from different reports, it only needs a single

well adjusted model to be succeed and then be generalized, studied and estimate the variables effect.

However, interpreting and comparing the results of other research groups should be more careful. So, the disadvantages are if a piece of selected information is not frequently used or applied, we might have disregard its influence. Just like happened with the rutile and brookite phases variables, where they did not influence the models' adjustment. The reason can be the variables are not actually connected. Or also, be a result of having far less information (on corresponding variables percentage and crystallite size).

Another disadvantage of using literature data is it might have a lack of standardization and boundary of information, variable, or scenario. As a consequence, the models can present inconsistencies.

For the database stability, the variables range should be in agreement, that is, the measurements in the same unit, having statistical information (error and variance, for example) and having the same order of magnitude (to not succumb a variable influence). This logic is supported by the crystallite size in the present work, where the Scherrer Equation was used for variables on groups **S** on Block B and had a better model adjustment than mixed groups with Scherrer equation and Rietveld refinement.

Despite so many variability in the database and ANN topologies, the result with highest coefficients found (which was from Block B) had fifty percent of success in addition to behaviour in harmony with predicted and observed data, that is, with a good precision, but a bad accuracy, suggesting that it should be further investigated.

This work assessed a literature report with no standard calculations for the band gap, in addition to incoherent reported results (such as reported by López and Gómez [38]), with a modelling strategy of ANN. Under these circumstances, the present work provided a qualified and extensive investigation of titanium dioxide parameters as a photocatalyst.

6
Conclusion

The present work was carried out to explore TiO_2 properties relationship using Artifial Neural Networks. The band gap value was used as an indirect variable of photocatalytic performance. The database was obtained from the literature, in order to be as representative, large, and diverse as possible.

The methodology had four main steps: data acquisition, data analysis, ANN development, and ANN settings. As a result, two blocks, namely Block A and Block B, were studied with different input parameters. Moreover, each block was arranged into groups to explore the influences of each variable in pairs (A) and the relevant similarities (B), using support variables for the band gap identification, **CP** and **TT**.

The Block A input parameters were the crystallite size and percentage rate for anatase phase, the specific surface area and the pore volume. The first attempt had the smallest database, on the other hand the best adjustment model with 99.82 % for training and 90.93 % for test. Since this database does not represent all parameters on literature beyond that of the own dataset, the database was four times increased and new models were developed.

The groups results did not succeed. The predict and observed values had a bad behaviour, and they had not been well adjusted. Besides this, the group I's result was the worst. However, both parameters **% A** and **dA** are obtained from XRD technique. Thus, the modelling was not reaching the nuances and getting into conflict, that is, the adjustments search of weights and bias were stopping before the global minimum.

The Block B input parameters were the crystallite size and percentage rate for each phase (anatase, rutile and brookite), the correspondent phase and the transition type of the band gap. This Block was a reformulation of the worst group result of Block A. Since group IV's inputs are structural properties (crystalline phases), they are more coherent variables to be further explored than the other parameters.

The impact of having a robust input parameters was that the system might be more bounded. As a consequence, the best model (**CF 4-4-6-1 trainlm, logsig, tansig, purelin**) according to the result of training (R^2 0.843) could not be validated by the test (R^2 0.507). Thus, the database

was reviewed and discussed. Discussion about characterization measurements suggests the calculation techniques should be applied more carefully, for instance, the band gap measurement and its correspondent transition type. Besides, standardization is highly necessary.

The strategy for modelling revealed that the learning procedure has a huge impact either for the training algorithm or the ANN type. A Cascade forward backpropagation with Levenberg-Marquard algorithm has manifested as the best learning. Thus, it should be more applied for other systems.

The main obstacle of modelling may have been originated from catalysis reports and its empirical nature. There is neither standard nor relative error enough for each measurement in the literature to support ANN development. In addition, the mathematical relation between photocatalyst properties for crystalline structure could be fulfilled with statistical data.

7
Future Research

For future research, we highly suggest the following items for a better understanding of materials properties modelling:

– Investigate more variables that can be used for modelling, either structure of the photocatalyst or from photocatalysis process, such as morphology and synthesis method, respectively, aiming to obtain the best scenario for photocatalysis operation.

– Perform a statistical report in the next experiments and measurements, such as standard error and covariance, aiming to improve the database for prediction.

– Apply the recommendations of DRS measurement, paying attention to the calculation methods according to the transition type involved.

– Promote debates about standard characterization techniques.

– Try another modelling technique, as Neurofuzzy, or Radial Basis Functions ANN.

– Adjust the training algorithm, e. g. with Particle Swarm Optimization

– Perform the experimental report through a Design of Experiments.

– Apply the neural models to validate the experimental results.

Bibliographic data

[1] HUMAYUN, M.; RAZIQ, F.; KHAN, A. ; LUO, W.. **Modification strategies of TiO₂ for potential applications in photocatalysis: a critical review**. Green Chemistry Letters and Reviews, 11(2):86–102, 2018.

[2] DAL SANTO, V.; NALDONI, A.. **Titanium dioxide photocatalysis**, volumen 8. 2018.

[3] HANAOR, D.; SORRELL, C.. **Review of the anatase to rutile phase transformation**. Journal of Materials Science, 46:855–874, 02 2011.

[4] SHI, D.; GUO, Z. ; BEDFORD, N.. **6 - nanotitanium oxide as a photocatalytic material and its application**. In: Shi, D.; Guo, Z. ; Bedford, N., editors, NANOMATERIALS AND DEVICES, Micro and Nano Technologies, p. 161 – 174. William Andrew Publishing, Oxford, 2015.

[5] JAFARI, T.; MOHARRERI, E.; AMIN, A. S.; MIAO, R.; SONG, W. ; SUIB, S. L.. **Photocatalytic water splitting - The untamed dream: A review of recent advances**. Molecules, 21(7), 2016.

[6] KOU, J.; LU, C.; WANG, J.; CHEN, Y.; XU, Z. ; VARMA, R. S.. **Selectivity Enhancement in Heterogeneous Photocatalytic Transformations**. Chemical Reviews, 117(3):1445–1514, 2017.

[7] ZULFIQAR, M.; SAMSUDIN, M. F. R. ; SUFIAN, S.. **Modelling and optimization of photocatalytic degradation of phenol via TiO₂ nanoparticles: An insight into response surface methodology and artificial neural network**. Journal of Photochemistry and Photobiology A: Chemistry, 384:112039, 2019.

[8] GHANBARY, F.; MODIRSHAHLA, N.; KHOSRAVI, M. ; BEHNA-JADY, M. A.. **Synthesis of TiO₂ nanoparticles in different thermal conditions and modeling its photocatalytic activity with artificial neural network**. Journal of Environmental Sciences, 24(4):750 – 756, 2012.

PUC-Rio - Certificação Digital Nº 1812690/CA

[9] TOMA, F.-L.; GUESSASMA, S.; KLEIN, D.; MONTAVON, G.; BERTRAND, G. ; CODDET, C.. **Neural computation to predict TiO₂ photocatalytic efficiency for nitrogen oxides removal**. Journal of Photochemistry and Photobiology A: Chemistry, 165(1):91 – 96, 2004.

[10] PAREEK, V.; BRUNGS, M.; ADESINA, A. ; SHARMA, R.. **Artificial neural network modeling of a multiphase photodegradation system**. Journal of Photochemistry and Photobiology A: Chemistry, 149(1):139 – 146, 2002.

[11] PIRDASHTI, M.; CURTEANU, S.; KAMANGAR, M. H.; HASSIM, M. H. ; KHATAMI, M. A.. **Artificial neural networks: Applications in chemical engineering**. Reviews in Chemical Engineering, 29(4):205–239, 2013.

[12] **Computational intelligence approach formodeling hydrogen production: A review**. Engineering Applications of Computational Fluid Mechanics, 12(1):438–458, 2018.

[13] REGO, A. S. D. C.. **Optimization of the parameters of delignification of sugarcane bagasse with alkaline hydrogen peroxide through neural model**. Master's thesis, Pontifical Catholic University of Rio de Janeiro, 2017.

[14] OWOLABI, T. O.; GONDAL, M. A.. **A hybrid intelligent scheme for estimating band gap of doped titanium dioxide semiconductor using crystal lattice distortion**. Computational Materials Science, 137:249 – 256, 2017.

[15] COSTA, L. H.. **Janus nanoparticles formed by gold and titanium dioxide as photocatalyst for hydrogen production from water**. Master's thesis, Pontifical Catholic University of Rio de Janeiro, 2018.

[16] AMARAL, R. N. P. D.. **Synthesis and characterization of Fe and Cu titanates heterojunctions grown on TiO₂ for water photolysis**. Master's thesis, Pontifical Catholic University of Rio de Janeiro, 2017.

[17] KITTEL, CHARLES. **Introduction to Solid State Physics**. John Wiley & Sons, 5 edition, 1976.

[18] CALLISTER, WILLIAM D.. **Materials Science and Engineering: An Introduction**. John Wiley & Sons, 5 edition, 1999.

[19] BELARUSIAN STATE UNIVERSITY. **Study of semiconductors by uv-vis absorption spectroscopy**. Department of Energy Physics TEMPUS program of the European Union, p. 1–15, 2012.

[20] PAN, H.. **Principles on design and fabrication of nanomaterials as photocatalysts for water-splitting**. Renewable and Sustainable Energy Reviews, 57:584 – 601, 2015.

[21] WANG, K.; JANCZAREK, M.; WEI, Z.; RAJA-MOGAN, T.; ENDO-KIMURA, M.; KHEDR, T. M.; OHTANI, B. ; KOWALSKA, E.. **Morphology- and Crystalline Composition-Governed Activity of Titania-Based Photocatalysts: Overview and Perspective**. Catalysts, 9(12):1054, dec 2019.

[22] CAMPS, E.; CASTREJÓN-SÁNCHEZ, V. H.; CAMACHO-LÓPEZ, M. ; BASURTO, R.. **Influence of the nitriding process on the band-gap of TiO$_2$ thin films with phase mixture**. In: THIN SOLID FILMS, volumen 581, p. 54–58. Elsevier B.V., apr 2015.

[23] TOBALDI, D.; LAJAUNIE, L.; ROZMAN, N.; CAETANO, A.; SEABRA, M.; ŠKAPIN, A. S.; ARENAL, R. ; LABRINCHA, J.. **Impact of the absolute rutile fraction on TiO$_2$ visible-light absorption and visible-light-promoted photocatalytic activity**. Journal of Photochemistry and Photobiology A: Chemistry, 382:111940, 2019.

[24] DU, H.; LIU, Y. N.; SHEN, C. C. ; XU, A. W.. **Nanoheterostructured photocatalysts for improving photocatalytic hydrogen production**. Cuihua Xuebao/Chinese Journal of Catalysis, 38(8):1295–1306, 2017.

[25] XU, F.; XIAO, W.; CHENG, B. ; YU, J.. **Direct z-scheme anatase/rutile bi-phase nanocomposite TiO$_2$ nanofiber photocatalyst with enhanced photocatalytic h2-production activity**. International Journal of Hydrogen Energy, 39(28):15394 – 15402, 2014.

[26] PULIDO MELIÁN, E.; GONZÁLEZ DÍAZ, O.; ORTEGA MÉNDEZ, A.; LÓPEZ, C. R.; NEREIDA SUÁREZ, M.; DOÑA RODRÍGUEZ, J.; NAVÍO, J.; FERNÁNDEZ HEVIA, D. ; PÉREZ PEÑA, J.. **Efficient and affordable hydrogen production by water photo-splitting using TiO$_2$ -based photocatalysts**. International Journal of Hydrogen Energy, 38(5):2144–2155, feb 2013.

[27] ROSSELER, O.; SHANKAR, M. V.; DU, M. K.-L.; SCHMIDLIN, L.; KELLER, N. ; KELLER, V.. **Solar light photocatalytic hydrogen production from water over Pt and Au/TiO2(anatase/rutile) photocatalysts: Influence of noble metal and porogen promotion**. Journal of Catalysis, 269(1):179–190, jan 2010.

[28] MARTÍNEZ, L.; BENITO, M.; MATA, I.; SOLER, L.; MOLINS, E. ; LLORCA, J.. **Preparation and photocatalytic activity of Au/ TiO₂ lyogels for hydrogen production**. Sustainable Energy and Fuels, 2(10):2284–2295, 2018.

[29] NADEEM, M. A.; MURDOCH, M.; WATERHOUSE, G. I.; METSON, J. B.; KEANE, M. A.; LLORCA, J. ; IDRISS, H.. **Photoreaction of ethanol on Au/ TiO₂ anatase: Comparing the micro to nanoparticle size activities of the support for hydrogen production**. Journal of Photochemistry and Photobiology A: Chemistry, 216(2-3):250–255, 2010.

[30] MARTÍNEZ, L.; SOLER, L.; ANGURELL, I. ; LLORCA, J.. **Effect of TiO₂ nanoshape on the photoproduction of hydrogen from water-ethanol mixtures over Au₃Cu/TiO₂ prepared with pre-formed Au-Cu alloy nanoparticles**. Applied Catalysis B: Environmental, 248(February):504–514, 2019.

[31] HOLM, A.; HAMANDI, M.; SIMONET, F.; JOUGUET, B.; DAPPOZZE, F. ; GUILLARD, C.. **Impact of rutile and anatase phase on the photocatalytic decomposition of lactic acid**. Applied Catalysis B: Environmental, 253:96–104, sep 2019.

[32] LOPEZ, T.; GOMEZ, R.; SANCHEZ, E.; TZOMPANTZI, F. ; VERA, L.. **Photocatalytic Activity in the 2,4-Dinitroaniline Decomposition Over TiO₂ Sol-Gel Derived Catalysts**. Journal of Sol-Gel Science and Technology, 22(1/2):99–107, 2001.

[33] ATEIA, M.; ALALM, M. G.; AWFA, D.; JOHNSON, M. S. ; YOSHIMURA, C.. **Modeling the degradation and disinfection of water pollutants by photocatalysts and composites: A critical review**. Science of the Total Environment, 698:134197, 2020.

[34] CARBAJO, J.; BAHAMONDE, A. ; FARALDOS, M.. **Photocatalyst performance in wastewater treatment applications: Towards the role of TiO₂ properties**. Molecular Catalysis, 434:167–174, jun 2017.

[35] KUNKA, C.; BOYCE, B. L.; FOILES, S. M. ; DINGREVILLE, R.. **Revealing inconsistencies in x-ray width methods for nanomaterials**. Nanoscale, 11:22456–22466, 2019.

[36] AVILLEZ, R. R. D.; ABRANTES, F. G. A. ; LETICHEVSKY, S.. **On the Intrinsic Limits of the Convolution Method to Obtain the Crystallite Size Distribution from Nanopowders Diffraction**. Materials Research, 21, 00 2018.

[37] BHATTACHARYYA, D.; CHAUDHURI, S. ; PAL, A.. **Bandgap and optical transitions in thin films from reflectance measurements**. Vacuum, 43(4):313 – 316, 1992.

[38] LÓPEZ, R.; GÓMEZ, R.. **Band-gap energy estimation from diffuse reflectance measurements on sol-gel and commercial TiO_2 : A comparative study**. Journal of Sol-Gel Science and Technology, 61(1):1–7, 2012.

[39] HAYKIN, S.. **Neural Networks: A Comprehensive Foundation**. Pearson Education, 2 edition, 1999.

[40] CUNHA VALIM, I.. **Modeling and optimization strategies applied to the sugarcane bagasse delignification processes**. Master's thesis, Pontifical Catholic University of Rio de Janeiro, 2018.

[41] SANTOS, B. F.. **Study of biosurfactant production using agroindustrial waste with development of statistical models and soft sensor by artificial neural network**. PhD thesis, University of Campinas, 2015.

[42] NETO, O.; PACHECO, M.. **Nanotecnologia Computacional Inteligente: CONCEBENDO A ENGENHARIA EM NANOTECNOLOGIA**. PUC-Rio and Interciência, 2012.

[43] MATLAB. **Deep Learning Toolbox version R2018b**. The MathWorks Inc., Natick, Massachusetts, 2018.

[44] WARSITO, B.; SANTOSO, R.; SUPARTI ; YASIN, H.. **Cascade forward neural network for time series prediction**. Journal of Physics: Conference Series, 1025:012097, may 2018.

[45] LI, H.; ZHANG, Z. ; LIU, Z.. **Application of artificial neural networks for catalysis: A review**. Catalysts, 7(10), 2017.

[46] TALWAR, S.; VERMA, A. K. ; SANGAL, V. K.. **Modeling and optimization of fixed mode dual effect (photocatalysis and photofenton) assisted metronidazole degradation using ann coupled with genetic algorithm**. Journal of Environmental Management, 250:109428, 2019.

[47] AZADI, S.; KARIMI-JASHNI, A. ; JAVADPOUR, S.. **Modeling and optimization of photocatalytic treatment of landfill leachate using tungsten-doped tio2 nano-photocatalysts: Application of artificial neural network and genetic algorithm**. Process Safety and Environmental Protection, 117:267 – 277, 2018.

[48] DAVRAN-CANDAN, T.; GÜNAY, M. E. ; YILDIRIM, R.. **Structure and activity relationship for co and O_2 adsorption over gold nanoparticles using density functional theory and artificial neural networks**. Journal of Chemical Physics, 132:174113, 2010.

[49] MASOLO, E.; SENES, N.; PELLICER, E.; BARÓ, M. D.; ENZO, S.; PILO, M. I.; MULAS, G. ; GARRONI, S.. **Evaluation of the anatase/rutile phase composition influence on the photocatalytic performances of mesoporous TiO_2 powders**. International Journal of Hydrogen Energy, 40(42):14483–14491, nov 2015.

[50] KHO, Y. K.; IWASE, A.; TEOH, W. Y.; MÄDLER, L.; KUDO, A. ; AMAL, R.. **Photocatalytic H2 Evolution over TiO_2 Nanoparticles. The Synergistic Effect of Anatase and Rutile**. The Journal of Physical Chemistry C, 114(6):2821–2829, feb 2010.

[51] HOU, J.; YANG, X.; LV, X.; HUANG, M.; WANG, Q. ; WANG, J.. **Controlled synthesis of TiO_2 mesoporous microspheres via chemical vapor deposition**. Journal of Alloys and Compounds, 511(1):202 – 208, 2012.

[52] ZHANG, J.; XIAO, X. ; NAN, J.. **Hydrothermal-hydrolysis synthesis and photocatalytic properties of nano- TiO_2 with an adjustable crystalline structure**. Journal of Hazardous Materials, 176(1-3):617–622, apr 2010.

[53] BEHNAJADY, M.; ESKANDARLOO, H.; MODIRSHAHLA, N. ; SHOKRI, M.. **Investigation of the effect of sol–gel synthesis variables on structural and photocatalytic properties of TiO_2 nanoparticles**. Desalination, (1-3):10–17, sep 2011.

[54] YU, J.; SU, Y.; CHENG, B. ; ZHOU, M.. **Effects of pH on the microstructures and photocatalytic activity of mesoporous nanocrystalline titania powders prepared via hydrothermal method**. Journal of Molecular Catalysis A: Chemical, 258(1-2):104–112, oct 2006.

[55] KIM, D. S.; KWAK, S.-Y.. **The hydrothermal synthesis of mesoporous TiO₂ with high crystallinity, thermal stability, large surface area, and enhanced photocatalytic activity**. Applied Catalysis A: General, 323:110–118, apr 2007.

[56] PANG, Y. L.; LIM, S.; ONG, H. C. ; CHONG, W. T.. **Synthesis, characteristics and sonocatalytic activities of calcined γ- Fe₂O₃ and TiO₂ nanotubes/γ- Fe₂O₃ magnetic catalysts in the degradation of Orange G**. Ultrasonics Sonochemistry, 29:317–327, mar 2016.

[57] BAO, N.; WEI, Z.; MA, Z.; LIU, F. ; YIN, G.. **Si-doped mesoporous TiO₂ continuous fibers: Preparation by centrifugal spinning and photocatalytic properties**. Journal of Hazardous Materials, 174(1-3):129–136, feb 2010.

[58] INTURI, S. N. R.; SUIDAN, M. ; SMIRNIOTIS, P. G.. **Influence of synthesis method on leaching of the Cr- TiO₂ catalyst for visible light liquid phase photocatalysis and their stability**. Applied Catalysis B: Environmental, 180:351–361, jan 2016.

[59] SANTOS, L. M. D.. **Síntese e caracterização de TiO₂ com modificações superficiais para aplicação em fotocatálise heterogênea**. PhD thesis, Universidade Federal de Uberlândia, 2017.

[60] MELIÁN], E. P.; HENRÍQUEZ-CÁRDENES, E.; DÍAZ], O. G. ; RO-DRÍGUEZ], J. D.. **Study of adsorption and degradation of dimethylphthalate on tio2-based photocatalysts**. Chemical Physics, 475:112 – 118, 2016.

[61] NIU, J.; YAO, B.; PENG, C.; ZHANG, W. ; CHEN, Y.. **Rapid Microwave Hydrothermal Methods Synthesis of TiO₂ Photocatalysts Using Different Sources of Materials**. Integrated Ferroelectrics, 152(1):163–173, mar 2014.

[62] SECK, E.; DOÑA-RODRÍGUEZ, J.; PULIDO MELIÁN, E.; FERNÁNDEZ-RODRÍGUEZ, C.; GONZÁLEZ-DÍAZ, O.; PORTILLO-CARRIZO, D. ; PÉREZ-PEÑA, J.. **Comparative study of**

nanocrystalline titanium dioxide obtained through sol–gel and sol–gel–hydrothermal synthesis. Journal of Colloid and Interface Science, 400:31–40, jun 2013.

[63] COLMENARES, J.; ARAMENDÍA, M.; MARINAS, A.; MARINAS, J. ; URBANO, F.. **Synthesis, characterization and photocatalytic activity of different metal-doped titania systems**. Applied Catalysis A: General, 306:120–127, jun 2006.

[64] YU, J.; XIONG, J.; CHENG, B. ; LIU, S.. **Fabrication and characterization of Ag– TiO₂ multiphase nanocomposite thin films with enhanced photocatalytic activity**. Applied Catalysis B: Environmental, 60(3-4):211–221, oct 2005.

[65] YU, J. C.; ZHANG, L.; ZHENG, Z. ; ZHAO, J.. **Synthesis and Characterization of Phosphated Mesoporous Titanium Dioxide with High Photocatalytic Activity**. Chemistry of Materials, 15(11):2280–2286, jun 2003.

[66] RENUKA, N.; PRAVEEN, A. ; ARAVINDAKSHAN, K.. **Synthesis and characterisation of mesoporous anatase TiO₂ with highly crystalline framework**. Materials Letters, 91:118–120, jan 2013.

[67] LIU, G.; HAN, C.; PELAEZ, M.; ZHU, D.; LIAO, S.; LIKODIMOS, V.; IOANNIDIS, N.; KONTOS, A. G.; FALARAS, P.; DUNLOP, P. S. M.; BYRNE, J. A. ; DIONYSIOU, D. D.. **Synthesis, characterization and photocatalytic evaluation of visible light activated C-doped TiO₂ nanoparticles**. Nanotechnology, (29):294003, jul 2012.

[68] PORKODI, K.; AROKIAMARY, S. D.. **Synthesis and spectroscopic characterization of nanostructured anatase titania: A photocatalyst**. Materials Characterization, 58(6):495–503, jun 2007.

[69] KŐRÖSI, L.; DÉKÁNY, I.. **Preparation and investigation of structural and photocatalytic properties of phosphate modified titanium dioxide**. Colloids and Surfaces A: Physicochemical and Engineering Aspects, 280(1-3):146–154, jun 2006.

[70] HUSSAIN, M.; CECCARELLI, R.; MARCHISIO, D.; FINO, D.; RUSSO, N. ; GEOBALDO, F.. **Synthesis, characterization, and photocatalytic application of novel TiO₂ nanoparticles**. Chemical Engineering Journal, 157(1):45–51, feb 2010.

[71] PERIYAT, P.; BAIJU, K.; MUKUNDAN, P.; PILLAI, P. ; WARRIER, K.. **High temperature stable mesoporous anatase TiO$_2$ photocatalyst achieved by silica addition**. Applied Catalysis A: General, (1-2):13–19, oct 2008.

[72] CHALLAGULLA, S.; NAGARJUNA, R.; GANESAN, R. ; ROY, S.. **TiO$_2$ synthesized by various routes and its role on environmental remediation and alternate energy production**. Nano-Structures & Nano-Objects, 12:147–156, oct 2017.

[73] CHOWDHURY, I. H.; KUNDU, S. ; NASKAR, M. K.. **Effect of organic acids on the physicochemical properties of titania and its photodegradation efficiency of methyl orange**. Journal of Physics and Chemistry of Solids, 121:367–374, oct 2018.

[74] KOLEN'KO, Y.; GARSHEV, A.; CHURAGULOV, B.; BOUJDAY, S.; PORTES, P. ; COLBEAU-JUSTIN, C.. **Photocatalytic activity of sol–gel derived titania converted into nanocrystalline powders by supercritical drying**. Journal of Photochemistry and Photobiology A: Chemistry, 172(1):19–26, may 2005.

[75] NOORIMOTLAGH, Z.; KAZEMINEZHAD, I.; JAAFARZADEH, N.; AHMADI, M.; RAMEZANI, Z. ; SILVA MARTINEZ, S.. **The visible-light photodegradation of nonylphenol in the presence of carbon-doped TiO$_2$ with rutile/anatase ratio coated on GAC: Effect of parameters and degradation mechanism**. Journal of Hazardous Materials, 350:108–120, may 2018.

[76] DI PAOLA, A.; CUFALO, G.; ADDAMO, M.; BELLARDITA, M.; CAMPOSTRINI, R.; ISCHIA, M.; CECCATO, R. ; PALMISANO, L.. **Photocatalytic activity of nanocrystalline TiO$_2$ (brookite, rutile and brookite-based) powders prepared by thermohydrolysis of TiCl$_4$ in aqueous chloride solutions**. Colloids and Surfaces A: Physicochemical and Engineering Aspects, 317(1-3):366–376, mar 2008.

[77] KUSIOR, A.; KLICH-KAFEL, J.; TRENCZEK-ZAJAC, A.; SWIERCZEK, K.; RADECKA, M. ; ZAKRZEWSKA, K.. **TiO$_2$–SnO$_2$ nanomaterials for gas sensing and photocatalysis**. Journal of the European Ceramic Society, 33(12):2285–2290, oct 2013.

[78] GANESH, I.. **Surface, structural, energy band-gap, and photocatalytic features of an emulsion-derived B-doped TiO$_2$ nanopowder**. Molecular Catalysis, 451:51–65, may 2018.

[79] QIAN, X.; HAN, H.; CHEN, Y. ; YUAN, Y.. **Sol–gel solvothermal route to synthesize anatase/brookite/rutile TiO₂ nanocomposites with highly photocatalytic activity**. Journal of Sol-Gel Science and Technology, 85(2):394–401, feb 2018.

[80] PIRZADA, B. M.; MIR, N. A.; QUTUB, N.; MEHRAJ, O.; SABIR, S. ; MUNEER, M.. **Synthesis, characterization and optimization of photocatalytic activity of TiO₂ / ZrO₂ nanocomposite heterostructures**. Materials Science and Engineering: B, 193:137–145, mar 2015.

[81] NAGAVENI, K.; SIVALINGAM, G.; HEGDE, M. ; MADRAS, G.. **Solar photocatalytic degradation of dyes: high activity of combustion synthesized nano TiO₂** . Applied Catalysis B: Environmental, 48(2):83–93, mar 2004.

[82] VENKATACHALAM, N.; PALANICHAMY, M. ; MURUGESAN, V.. **Sol–gel preparation and characterization of nanosize TiO₂: Its photocatalytic performance**. Materials Chemistry and Physics, 104(2-3):454–459, aug 2007.

[83] MATOS, J.; OCARES-RIQUELME, J.; POON, P. S.; MONTAÑA, R.; GARCÍA, X.; CAMPOS, K.; HERNÁNDEZ-GARRIDO, J. C. ; TITIRICI, M. M.. **C-doped anatase TiO₂ : Adsorption kinetics and photocatalytic degradation of methylene blue and phenol, and correlations with DFT estimations**. Journal of Colloid and Interface Science, 547:14–29, jul 2019.

[84] FIORENZA, R.; BELLARDITA, M.; SCIRÈ, S. ; PALMISANO, L.. **Effect of the addition of different doping agents on visible light activity of porous TiO₂ photocatalysts**. Molecular Catalysis, 455:108–120, aug 2018.

[85] YU, J.; ZHOU, M.; CHENG, B. ; ZHAO, X.. **Preparation, characterization and photocatalytic activity of in situ N,S-codoped TiO₂ powders**. Journal of Molecular Catalysis A: Chemical, 246(1-2):176–184, mar 2006.

[86] LIU, C.; TANG, X.; MO, C. ; QIANG, Z.. **Characterization and activity of visible-light-driven TiO₂ photocatalyst codoped with nitrogen and cerium**. Journal of Solid State Chemistry, 181(4):913–919, apr 2008.

[87] SHEN, L.; BAO, N.; ZHENG, Y.; GUPTA, A.; AN, T. ; YANAGI-SAWA, K.. **Hydrothermal Splitting of Titanate Fibers to Single-Crystalline TiO$_2$ Nanostructures with Controllable Crystalline Phase, Morphology, Microstructure, and Photocatalytic Activity**. The Journal of Physical Chemistry C, 112(24):8809–8818, jun 2008.

[88] ADDAMO, M.; DEL ARCO, M.; BELLARDITA, M.; CARRIAZO, D.; DI PAOLA, A.; GARCÍA-LÓPEZ, E.; MARCI, G.; MARTÍN, C.; PALMISANO, L. ; RIVES, V.. **Photoactivity of nanostructured TiO$_2$ catalysts in aqueous system and their surface acid-base, bulk and textural properties**. Research on Chemical Intermediates, 33:465–479, 2007.

[89] VERMA, R.; SAMDARSHI, S.. **Correlating oxygen vacancies and phase ratio/interface with efficient photocatalytic activity in mixed phase TiO$_2$** . Journal of Alloys and Compounds, 629:105–112, apr 2015.

[90] RATNAWATI; GUNLAZUARDI, J.; DEWI, E. L. ; SLAMET. **Effect of NaBF4 addition on the anodic synthesis of TiO$_2$ nanotube arrays photocatalyst for production of hydrogen from glycerol–water solution**. International Journal of Hydrogen Energy, 39(30):16927–16935, oct 2014.

[91] KHAN, H.. **Sol–gel synthesis of TiO$_2$ from TiOSO$_4$: characterization and UV photocatalytic activity for the degradation of 4-chlorophenol**. Reaction Kinetics, Mechanisms and Catalysis, 121(2):811–832, aug 2017.

[92] SAKET-OSKOUI, M.; KHATAMIAN, M.; NOFOUZI, K. ; YAVARI, A.. **Study on crystallinity and morphology controlling of titania using acrylamide gel method and their photocatalytic properties**. Advanced Powder Technology, 25(5):1634–1642, sep 2014.

[93] MAURYA, A.; CHAUHAN, P.; MISHRA, S. K. ; SRIVASTAVA, R. K.. **Structural, optical and charge transport study of rutile TiO$_2$ nanocrystals at two calcination temperatures**. Journal of Alloys and Compounds, 509(33):8433–8440, aug 2011.

[94] SAKET-OSKOUI, M.; KHATAMIAN, M.. **Morphology and crystalline phase-controllable synthesis of titania nanoparticles via acrylamide gel method and their photocatalytic properties**. Materials Science in Semiconductor Processing, 27:103–113, nov 2014.

[95] FAHIM, N. F.; SEKINO, T.. **A Novel Method for Synthesis of Titania Nanotube Powders using Rapid Breakdown Anodization**. Chemistry of Materials, 21(9):1967–1979, may 2009.

[96] YU, J. C.; ZHANG, L. ; YU, J.. **Direct Sonochemical Preparation and Characterization of Highly Active Mesoporous TiO$_2$ with a Bicrystalline Framework**. Chemistry of Materials, 14(11):4647–4653, nov 2002.

[97] GÜNAY, M. E.; YILDIRIM, R.. **Neural network analysis of selective CO oxidation over copper-based catalysts for knowledge extraction from published data in the literature**. Industrial and Engineering Chemistry Research, 50(22):12488–12500, 2011.

[98] VOEPEL, P.; WEISS, M.; SMARSLY, B. M. ; MARSCHALL, R.. **Photocatalytic activity of multiphase TiO$_2$(b)/anatase nanoparticle heterojunctions prepared from ionic liquids**. Journal of Photochemistry and Photobiology A: Chemistry, 366:34 – 40, 2018. Special Issue on Selected Papers from the Sixth International Conference on Semiconductor Photochemistry - SP-6.

8
Appendix

	Authors	Title	Year	Source title	DOI
1	Liu T., Liu Y., Wang D., Li Y., Shao L.	Artificial neural network modeling on the prediction of mass transfer coefficient for ozone absorption in RPB	2019	Chemical Engineering Research and Design	10.1016/j.cherd.2019.09.027
2	Jadhav A.J., Srivastava V.C.	Multicomponent adsorption isotherm modeling using thermodynamically inconsistent and consistent models	2019	AIChE Journal	10.1002/aic.16727
3	Ding Y., Zhang Y., Ren Y.M., Orkoulas G., Christofides P.D.	Machine learning-based modeling and operation for ALD of SiO2 thin-films using data from a multiscale CFD simulation	2019	Chemical Engineering Research and Design	10.1016/j.cherd.2019.09.005
4	Pavlić B., Kaplan M., Bera O., Oktem Olgun E., Canli O., Milosavljević N., Antić B., Zeković Z.	Microwave-assisted extraction of peppermint polyphenols – Artificial neural networks approach	2019	Food and Bioproducts Processing	10.1016/j.fbp.2019.09.016
5	Zaranezhad A., Asilian Mahabadi H., Dehghani M.R.	Development of prediction models for repair and maintenance-related accidents at oil refineries using artificial neural network, fuzzy system, genetic algorithm, and ant colony optimization algorithm	2019	Process Safety and Environmental Protection	10.1016/j.psep.2019.08.031
6	Oskui F.N., Aghdasinia H., Sorkhabi M.G.	Modeling and optimization of chromium adsorption onto clay using response surface methodology, artificial neural network, and equilibrium isotherm models	2019	Environmental Progress and Sustainable Energy	10.1002/ep.13260
7	Pădurețu C.-C., Isopescu R., Râu I., Apetroaei M.R., Schröder V.	Influential extraction parameters for the characterization of chitosan from crab shell	2019	Korean Journal of Chemical Engineering	10.1007/s11814-019-0379-7
8	Gülüm M., Onay F.K., Bilgin A.	Measurement and estimation of densities of different biodiesel–diesel–alcohol ternary blends	2019	Environmental Progress and Sustainable Energy	10.1002/ep.13248
9	Fiyadh S.S., AlSaadi M.A., Binti Jaafar W.Z., AlOmar M.K., Fayaed S.S., Hama A.R., Hin L.S., El-Shafie A.	Mercury removal from water using deep eutectic solvents-functionalized multi walled carbon nanotubes: Nonlinear autoregressive network with an exogenous input neural network approach	2019	Environmental Progress and Sustainable Energy	10.1002/ep.13261
10	Hemmat Esfe M., Kiannejad Amiri M., Bahiraei M.	Optimizing thermophysical properties of nanofluids using response surface methodology and particle swarm optimization in a non-dominated sorting genetic algorithm	2019	Journal of the Taiwan Institute of Chemical Engineers	10.1016/j.jtice.2019.07.009
11	Shi J., Li X., Khan F., Chang Y., Zhu Y., Chen G.	Artificial bee colony Based Bayesian Regularization Artificial Neural Network approach to model transient flammable cloud dispersion in congested area	2019	Process Safety and Environmental Protection	10.1016/j.psep.2019.05.046
12	Tolba A., Gar Alalm M., Elsamadony M., Mostafa A., Afify H., Dionysiou D.D.	Modeling and optimization of heterogeneous Fenton-like and photo-Fenton processes using reusable Fe3O4-MWCNTs	2019	Process Safety and Environmental Protection	10.1016/j.psep.2019.06.011
13	Ayoubi-Feiz B., Sheydaei M., Karimi M.	Visible light photoelectrocatalysis for wastewater treatment using bifacial N-TiO2/Graphene/Ho2O3/Titanium nanocomposite: Artificial neural network modeling and evaluation of ozone addition	2019	Process Safety and Environmental Protection	10.1016/j.psep.2019.04.026
14	Nikkhah A., Rohani A., Rosentrater K.A., El Haj Assad M., Ghnimi S.	Integration of principal component analysis and artificial neural networks to more effectively predict agricultural energy flows	2019	Environmental Progress and Sustainable Energy	10.1002/ep.13130
15	Stratiev D., Shishkova I., Tankov I., Pavlova A.	Challenges in characterization of residual oils. A review	2019	Journal of Petroleum Science and Engineering	10.1016/j.petrol.2019.03.026
16	Boral S., Chaturvedi S.K., Naikan V.N.A.	A case-based reasoning system for fault detection and isolation: a case study on complex gearboxes	2019	Journal of Quality in Maintenance Engineering	10.1108/JQME-05-2018-0039
17	Schäfer P., Caspari A., Kleinhans K., Mhamdi A., Mitsos A.	Reduced dynamic modeling approach for rectification columns based on compartmentalization and artificial neural networks	2019	AIChE Journal	10.1002/aic.16568
18	Godo-Pla L., Emiliano P., Valero F., Poch M., Sin G., Monclús H.	Predicting the oxidant demand in full-scale drinking water treatment using an artificial neural network: Uncertainty and sensitivity analysis	2019	Process Safety and Environmental Protection	10.1016/j.psep.2019.03.017
19	Abbasi M., Rastgoo M.N., Nakisa B.	Monthly and seasonal modeling of municipal waste generation using radial basis function neural network	2019	Environmental Progress and Sustainable Energy	10.1002/ep.13033
20	Ding Y., Zhang Y., Kim K., Tran A., Wu Z., Christofides P.D.	Microscopic modeling and optimal operation of thermal atomic layer deposition	2019	Chemical Engineering Research and Design	10.1016/j.cherd.2019.03.004

Figure 8.1: Data from Figure 1.1: articles from Scopus 2015-2019 with ANN, photocatalysis and engineers.

	Authors	Title	Year	Source title	DOI
21	Hamedi H., Ehteshami M., Mirbagheri S.A., Zendehboudi S.	New deterministic tools to systematically investigate fouling occurrence in membrane bioreactors	2019	Chemical Engineering Research and Design	10.1016/j.cherd.2019.02.003
22	Yarveicy H., Saghafi H., Ghiasi M.M., Mohammadi A.H.	Decision tree-based modeling of CO 2 equilibrium absorption in different aqueous solutions of absorbents	2019	Environmental Progress and Sustainable Energy	10.1002/ep.13128
23	Jeon K., Yang S., Kang D., Na J., Lee W.B.	Development of surrogate model using CFD and deep neural networks to optimize gas detector layout	2019	Korean Journal of Chemical Engineering	10.1007/s11814-018-0204-8
24	Bagheri M., Akbari A., Mirbagheri S.A.	Advanced control of membrane fouling in filtration systems using artificial intelligence and machine learning techniques: A critical review	2019	Process Safety and Environmental Protection	10.1016/j.psep.2019.01.013
25	Rizkin B.A., Popovich K., Hartman R.L.	Artificial Neural Network control of thermoelectrically-cooled microfluidics using computer vision based on IR thermography	2019	Computers and Chemical Engineering	10.1016/j.compchemeng.2018.11.016
26	Feng J., Hajizadeh I., Yu X., Rashid M., Samadi S., Sevil M., Hobbs N., Brandt R., Lazaro C., Maloney Z., Littlejohn E., Quinn L., Cinar A.	Multi-model sensor fault detection and data reconciliation: A case study with glucose concentration sensors for diabetes	2019	AIChE Journal	10.1002/aic.16435
27	Li F., Wang W., Xu J., Yi J., Wang Q.	Comparative study on vulnerability assessment for urban buried gas pipeline network based on SVM and ANN methods	2019	Process Safety and Environmental Protection	10.1016/j.psep.2018.11.014
28	Al-Refaie A., Bani Domi G., Abdullah R.	A fuzzy goal programming-regression approach to optimize process performance of multiple responses under uncertainty	2019	International Journal of Management Science and Engineering Management	10.1080/17509653.2018.1467802
29	Kılıç B., Arabacı E.	Alternative approach in performance analysis of organic rankine cycle (ORC)	2019	Environmental Progress and Sustainable Energy	10.1002/ep.12901
30	Panerati J., Schnellmann M.A., Patience C., Beltrame G., Patience G.S.	Experimental methods in chemical engineering: Artificial neural networks–ANNs	2019	Canadian Journal of Chemical Engineering	10.1002/cjce.23507
31	Torabi M., Hashemi S., Saybani M.R., Shamshirband S., Mosavi A.	A Hybrid clustering and classification technique for forecasting short-term energy consumption	2019	Environmental Progress and Sustainable Energy	10.1002/ep.12934
32	Li W., Xia F., Zhao S., Zhang M., Li W., Zhang J.	Characterization of liquid–liquid mass transfer performance in a novel pore-array intensified tube-in-tube microchannel	2019	AIChE Journal	10.1002/aic.16893
33	Bharadwaj A.V.S.L.S., Niju S., Meera Sheriffa Begum K.M., Anantharaman N.	Performance and evaluation of calcined limestone as catalyst in biodiesel production from high viscous nonedible oil	2019	Environmental Progress and Sustainable Energy	10.1002/ep.13342
34	Boojari M.A., Zamir S.M., Shojaosadati S.A.	Transient-state strategies for the removal of toluene vapor in a two-liquid phase biotrickling filter: Experimental study and neural network analysis	2019	Process Safety and Environmental Protection	10.1016/j.psep.2018.10.017
35	Wang B., Qian F.	Three dimensional gas dispersion modeling using cellular automata and artificial neural network in urban environment	2018	Process Safety and Environmental Protection	10.1016/j.psep.2018.09.006
36	Sayyad Amin J., Zendehboudi S., Mohamadi E.	Evolution of tar ball aggregates in Caspian Sea: Implications of connectionist tools linked with image analysis	2018	Environmental Progress and Sustainable Energy	10.1002/ep.12886
37	Mehmood A., Haq N.-U., Zameer A., Ling S.H., Raja M.A.Z.	Design of neuro-computing paradigms for nonlinear nanofluidic systems of MHD Jeffery–Hamel flow	2018	Journal of the Taiwan Institute of Chemical Engineers	10.1016/j.jtice.2018.05.046
38	Hosseinzadeh A., Najafpoor A.A., Jafari A.J., Jazani R.K., Baziar M., Bargozin H., Piranloo F.G.	Application of response surface methodology and artificial neural network modeling to assess non-thermal plasma efficiency in simultaneous removal of BTEX from waste gases: Effect of operating parameters and prediction performance	2018	Process Safety and Environmental Protection	10.1016/j.psep.2018.08.010
39	Sodeifian G., Sajadian S.A., Razmimanesh F., Ardestani N.S.	A comprehensive comparison among four different approaches for predicting the solubility of pharmaceutical solid compounds in supercritical carbon dioxide	2018	Korean Journal of Chemical Engineering	10.1007/s11814-018-0125-6
40	Alizamir M., Azhdary Moghadam M., Hashemi Monfared A., Shamsipour A.	Statistical downscaling of global climate model outputs to monthly precipitation via extreme learning machine: A case study	2018	Environmental Progress and Sustainable Energy	10.1002/ep.12856

Figure 8.2: Data from Figure 1.1 (continued).

	Authors	Title	Year	Source title	DOI
41	Lashkarbolooki M., Bayat M.	Prediction of surface tension of liquid normal alkanes, 1-alkenes and cycloalkane using neural network	2018	Chemical Engineering Research and Design	10.1016/j.cherd.2018.07.021
42	Kim B.S., Kim T.Y., Park T.C., Yeo Y.K.	Comparative study of estimation methods of NOx emission with selection of input parameters for a coal-fired boiler	2018	Korean Journal of Chemical Engineering	10.1007/s11814-018-0087-8
43	Razzaghi M., Karimi A., Ansari Z., Aghdasinia H.	Phenol removal by HRP/GOx/ZSM-5 from aqueous solution: Artificial neural network simulation and genetic algorithms optimization	2018	Journal of the Taiwan Institute of Chemical Engineers	10.1016/j.jtice.2018.03.040
44	Ahmadzadeh F.	Change point detection with multivariate control charts by artificial neural network	2018	International Journal of Advanced Manufacturing Technology	10.1007/s00170-009-2193-6
45	Charde S.J., Sonawane S.S., Sonawane S.H., Shimpi N.G.	Degradation kinetics of polycarbonate composites: Kinetic parameters and artificial neural network	2018	Chemical and Biochemical Engineering Quarterly	10.15255/CABEQ.2017.1173
46	Azadi S., Karimi-Jashni A., Javadpour S.	Modeling and optimization of photocatalytic treatment of landfill leachate using tungsten-doped TiO2 nano-photocatalysts: Application of artificial neural network and genetic algorithm	2018	Process Safety and Environmental Protection	10.1016/j.psep.2018.03.038
47	Soleimani R., Saeedi Dehaghani A.H., Shoushtari N.A., Yaghoubi P., Bahadori A.	Toward an intelligent approach for predicting surface tension of binary mixtures containing ionic liquids	2018	Korean Journal of Chemical Engineering	10.1007/s11814-017-0326-4
48	Banihashemi M., Movagharnejad K.	Use of group contribution method and intelligent algorithms to predict the flash temperature of binary mixtures	2018	Process Safety and Environmental Protection	10.1016/j.psep.2018.04.016
49	Hasani G., Daraei H., Shahmoradi B., Gharibi F., Maleki A., Yetilmezsoy K., McKay G.	A novel ANN approach for modeling of alternating pulse current electrocoagulation-flotation (APC-ECF) process: Humic acid removal from aqueous media	2018	Process Safety and Environmental Protection	10.1016/j.psep.2018.04.017
50	Ibrahim D., Jobson M., Li J., Guillén-Gosálbez G.	Optimization-based design of crude oil distillation units using surrogate column models and a support vector machine	2018	Chemical Engineering Research and Design	10.1016/j.cherd.2018.03.006
51	Thakker M.R., Parikh J.K., Desai M.A.	Synergism between ionic liquid and ultrasound for greener extraction of geraniol: Optimization using different statistical tools, comparison and prediction	2018	Chemical Engineering Research and Design	10.1016/j.cherd.2018.04.003
52	Monazzami A., Vahabzadeh F., Aroujalian A., Mogharei A.	An artificial neural network approach to determine the rheological behavior of pickering-type diesel-in-water emulsion prepared with the use of β-cyclodextrin	2018	Korean Journal of Chemical Engineering	10.1007/s11814-017-0351-3
53	das Neves T.G., Ramos W.B., de Farias Neto G.W., Brito R.P.	Intelligent control system for extractive distillation columns	2018	Korean Journal of Chemical Engineering	10.1007/s11814-017-0346-0
54	Yarveicy H., Ghiasi M.M., Mohammadi A.H.	Determination of the gas hydrate formation limits to isenthalpic Joule–Thomson expansions	2018	Chemical Engineering Research and Design	10.1016/j.cherd.2017.12.046
55	Pazouki M., Zabihi M., Shayegan J., Fatehi M.H.	Mercury ion adsorption on AC@Fe3O4-NH2-COOH from saline solutions: Experimental studies and artificial neural network modeling	2018	Korean Journal of Chemical Engineering	10.1007/s11814-017-0293-9
56	Alizadeh Kordkandi S., Mohaghegh Motlagh A.	Optimization of peroxone reaction rate using metaheuristic approach in the dearomatization and discoloration process	2018	Environmental Progress and Sustainable Energy	10.1002/ep.12741
57	Sahai S., Kulkarni T., Tikhe S., Mathpati C.S.	Use of artificial neural network to predict pressure drop in rough pipes	2018	Proceedings of the International Conference on Computing Methodologies and Communication, ICCMC 2017	10.1109/ICCMC.2017.8282729
58	Bourek Y., M'Ziou N., Benguesmia H.	Prediction of Flashover Voltage of High-Voltage Polluted Insulator Using Artificial Intelligence	2018	Transactions on Electrical and Electronic Materials	10.1007/s42341-018-0010-3
59	Davoudi E., Vaferi B.	Applying artificial neural networks for systematic estimation of degree of fouling in heat exchangers	2018	Chemical Engineering Research and Design	10.1016/j.cherd.2017.12.017
60	Jana A.K., Banerjee S.	Neuro estimator-based inferential extended generic model control of a reactive distillation column	2018	Chemical Engineering Research and Design	10.1016/j.cherd.2017.12.041

Figure 8.3: Data from Figure 1.1 (continued).

	Authors	Title	Year	Source title	DOI
61	Shaahmadi F., Anbaz M.A., Bazooyar B.	The analysis of liquid–liquid equilibria (LLE) of toluene + heptane + ionic liquid ternary mixture using intelligent models	2018	Chemical Engineering Research and Design	10.1016/j.cherd.2017.12.029
62	Bleotu I., Dragoi E.N., Mureşeanu M., Dorneanu S.-A.	Removal of Cu(II) ions from aqueous solutions by an ion-exchange process: Modeling and optimization	2018	Environmental Progress and Sustainable Energy	10.1002/ep.12793
63	Mohadesi M., Rezaei A.	Biodiesel conversion modeling under several conditions using computational intelligence methods	2018	Environmental Progress and Sustainable Energy	10.1002/ep.12698
64	Valinger D., Kušen M., Jurinjak Tušek A., Panić M., Jurina T., Benković M., Radojčić Redovniković I., Gajdoš Kljusurić J.	Development of near infrared spectroscopy models for quantitative prediction of the content of bioactive compounds in olive leaves	2018	Chemical and Biochemical Engineering Quarterly	10.15255/CABEQ.2018.1396
65	Joshi C., Singhal R.S.	Zeaxanthin production by Paracoccus zeaxanthinifaciens ATCC 21588 in a lab-scale bubble column reactor: Artificial intelligence modelling for determination of optimal operational parameters and energy requirements	2018	Korean Journal of Chemical Engineering	10.1007/s11814-017-0253-4
66	Kim T.Y., Kim B.S., Park T.C., Yeo Y.K.	Model-based control of a molten carbonate fuel cell (MCFC) process	2018	Korean Journal of Chemical Engineering	10.1007/s11814-017-0274-z
67	Md Nor N., Che Hassan C.R., Hussain M.A.	A review of data-driven fault detection and diagnosis methods: Applications in chemical process systems	2018	Reviews in Chemical Engineering	10.1515/revce-2017-0069
68	Nabizadeh Chianeh F., Basiri Parsa J., Rezaei Vahidian H.	Artificial neural network modeling for removal of azo dye from aqueous solutions by Ti anode coated with multiwall carbon nanotubes	2017	Environmental Progress and Sustainable Energy	10.1002/ep.12650
69	Khorashadizadeh M., Atashi H., Mirzaei A.A.	Process conditions effects on Fischer–Tropsch product selectivity: Modeling and optimization through a time and cost-efficient scenario using a limited data size	2017	Journal of the Taiwan Institute of Chemical Engineers	10.1016/j.jtice.2017.09.006
70	Sushma C., Anand A.P., Veeranki V.D.	Enhanced production of glutaminase free L-asparaginase II by Bacillus subtilis WB800N through media optimization	2017	Korean Journal of Chemical Engineering	10.1007/s11814-017-0211-1
71	Raja M.A.Z., Ahmed T., Shah S.M.	Intelligent computing strategy to analyze the dynamics of convective heat transfer in MHD slip flow over stretching surface involving carbon nanotubes	2017	Journal of the Taiwan Institute of Chemical Engineers	10.1016/j.jtice.2017.08.016
72	Adedigba S.A., Khan F., Yang M.	Dynamic failure analysis of process systems using neural networks	2017	Process Safety and Environmental Protection	10.1016/j.psep.2017.08.005
73	Mohebbi A., Ahmadi-Pour M., Mohebbi M.	Accurate prediction of liquid phase equilibrium adsorption of sulfur compound	2017	Chemical Engineering Research and Design	10.1016/j.cherd.2017.08.024
74	Yildiz S.	Artificial neural network (ANN) approach for modeling Zn(II) adsorption in batch process	2017	Korean Journal of Chemical Engineering	10.1007/s11814-017-0157-3
75	Stenzel O., Pecho O., Holzer L., Neumann M., Schmidt V.	Big data for microstructure-property relationships: A case study of predicting effective conductivities	2017	AIChE Journal	10.1002/aic.15757
76	Hosseinzadeh-Bandbafha H., Nabavi-Pelesaraei A., Shamshirband S.	Investigations of energy consumption and greenhouse gas emissions of fattening farms using artificial intelligence methods	2017	Environmental Progress and Sustainable Energy	10.1002/ep.12604
77	Haratipour P., Baghban A., Mohammadi A.H., Nazhad S.H.H., Bahadori A.	On the estimation of viscosities and densities of CO2-loaded MDEA, MDEA + AMP, MDEA + DIPA, MDEA + MEA, and MDEA + DEA aqueous solutions	2017	Journal of Molecular Liquids	10.1016/j.molliq.2017.06.123
78	Lauret P., Heymes F., Forestier S., Aprin L., Pey A., Perrin M.	Forecasting powder dispersion in a complex environment using Artificial Neural Networks	2017	Process Safety and Environmental Protection	10.1016/j.psep.2017.02.003
79	Şahin S., Sayim E., Samli R.	Comparative study of modeling the stability improvement of sunflower oil with olive leaf extract	2017	Korean Journal of Chemical Engineering	10.1007/s11814-017-0106-1
80	Masiur Rahman S., Khondaker A.N., Imtiaz Hossain M., Shafiullah M., Hasan M.A.	Neurogenetic modeling of energy demand in the United Arab Emirates, Saudi Arabia, and Qatar	2017	Environmental Progress and Sustainable Energy	10.1002/ep.12558

Figure 8.4: Data from Figure 1.1 (continued).

	Authors	Title	Year	Source title	DOI
201	Lenzi G.G., Evangelista R.F., Duarte E.R., Colpini L.M.S., Fornari A.C., Menechini Neto R., Jorge L.M.M., Santos O.A.A.	Photocatalytic degradation of textile reactive dye using artificial neural network modeling approach	2016	Desalination and Water Treatment	10.1080/19443994.2015.1064035
202	Fathinia M., Khataee A., Aber S., Naseri A.	Development of kinetic models for photocatalytic ozonation of phenazopyridine on TiO2 nanoparticles thin film in a mixed semi-batch photoreactor	2016	Applied Catalysis B: Environmental	10.1016/j.apcatb.2015.11.033
203	Shargh M., Behnajady M.A.	A high-efficient batch-recirculated photoreactor packed with immobilized TiO2-P25 nanoparticles onto glass beads for photocatalytic degradation of phenazopyridine as a pharmaceutical contaminant: Artificial neural network modeling	2016	Water Science and Technology	10.2166/wst.2016.132
204	Rasoulifard M.H., Seyed Dorraji M.S., Amani-Ghadim A.R., Keshavarz-Babaeinezhad N.	Visible-light photocatalytic activity of chitosan/polyaniline/CdS nanocomposite: Kinetic studies and artificial neural network modeling	2016	Applied Catalysis A: General	10.1016/j.apcata.2016.01.002
205	Garg A., Sangal V.K., Bajpai P.K.	Decolorization and degradation of Reactive Black 5 dye by photocatalysis: modeling, optimization and kinetic study	2016	Desalination and Water Treatment	10.1080/19443994.2015.1086697
206	Hassani A., Khataee A., Karaca S.	Photocatalytic degradation of ciprofloxacin by synthesized TiO2 nanoparticles on montmorillonite: Effect of operation parameters and artificial neural network modeling	2015	Journal of Molecular Catalysis A: Chemical	10.1016/j.molcata.2015.08.020
207	Behnajady M.A., Eskandarloo H., Eskandarloo F.	Artificial neural network modeling of the influence of sol-gel synthesis variables on the photocatalytic activity of TiO2 nanoparticles in the removal of Acid Red 27	2015	Research on Chemical Intermediates	10.1007/s11164-014-1753-z
208	David C., Arivazhagan M., Ibrahim M.	Spent wash decolourization using nano-Al2O3/kaolin photocatalyst: Taguchi and ANN approach	2015	Journal of Saudi Chemical Society	10.1016/j.jscs.2015.05.012
209	González-Campos G., Torres-Treviño L.M., Luévano-Hipólito E., Martinez-De La Cruz A.	Modeling synthesis processes of photocatalysts using symbolic regression α-β	2015	Proceedings of Special Session 2014 13th Mexican International Conference on Artificial Intelligence: Advances in Artificial Intelligence, MICAI 2014	10.1109/MICAI.2014.33
210	Kıranşan M., Khataee A., Karaca S., Sheydaei M.	Artificial neural network modeling of photocatalytic removal of a disperse dye using synthesized of ZnO nanoparticles on montmorillonite	2015	Spectrochimica Acta - Part A: Molecular and Biomolecular Spectroscopy	10.1016/j.saa.2014.12.100
211	Delnavaz M.	Application of artificial neural networks for prediction of photocatalytic reactor	2015	Water Environment Research	10.2175/WERD1400430.1
212	Amani-Ghadim A.R., Dorraji M.S.S.	Modeling of photocatalyatic process on synthesized ZnO nanoparticles: Kinetic model development and artificial neural networks	2015	Applied Catalysis B: Environmental	10.1016/j.apcatb.2014.08.020
213	Sabonian M., Behnajady M.A.	Artificial neural network modeling of Cr(VI) photocatalytic reduction with TiO2-P25 nanoparticles using the results obtained from response surface methodology optimization	2015	Desalination and Water Treatment	10.1080/19443994.2014.963161
214	Behnajady M.A., Eskandarloo H.	Preparation of TiO2 nanoparticles by the sol-gel method under different pH conditions and modeling of photocatalytic activity by artificial neural network	2015	Research on Chemical Intermediates	10.1007/s11164-013-1327-5
215	Vaez M., Omidkhah M., Alijani S., Zarringhalam Moghaddam A., Sadrameli M., Gholipour Zanjani N.	Evaluation of photocatalytic activity of immobilized titania nanoparticles by support vector machine and artificial neural network	2015	Canadian Journal of Chemical Engineering	10.1002/cjce.22171
216	Kıranşan M., Khataee A., Karaca S., Sheydaei M.	Synthesis of zinc oxide nanoparticles on montmorillonite for photocatalytic degradation of basic yellow 28: Effect of parameters and neural network modeling	2015	Current Nanoscience	10.2174/1573413711666150218002259
217	Mitschker J., Klüner T.	Adsorption and electronic excitation of water on TiO2 (110): Calculation of high-dimensional potential energy surfaces	2015	High Performance Computing in Science and Engineering '14: Transactions of the High Performance Computing Center, Stuttgart (HLRS) 2014	10.1007/978-3-319-10810-0_14
218	Diamanti M.V., Ormellese M., Pedeferri M.	Application-wise nanostructuring of anodic films on titanium: a review	2015	Journal of Experimental Nanoscience	10.1080/17458080.2014.999261

Figure 8.5: Data from Figure 1.1 (continued).

	Authors	Title	Year	Source title	DOI
81	Kim T.Y., Kim B.S., Park T.C., Yeo Y.K.	A comparative study of models for molten carbonate fuel cell (MCFC) processes	2017	Korean Journal of Chemical Engineering	10.1007/s11814-017-0117-y
82	Liu H., Xiao M., Liang Z., Tontiwachwuthikul P.	The analysis of solubility, absorption kinetics of CO2 absorption into aqueous 1-diethylamino-2-propanol solution	2017	AIChE Journal	10.1002/aic.15621
83	Pirrung S.M., van der Wielen L.A.M., van Beckhoven R.F.W.C., van de Sandt E.J.A.X., Eppink M.H.M., Ottens M.	Optimization of biopharmaceutical downstream processes supported by mechanistic models and artificial neural networks	2017	Biotechnology Progress	10.1002/btpr.2435
84	Abbasi M., Niaei A., Salari D., Hosseini S.A., Abedini F., Marmarshahi S.	Modeling and optimization of synthesis parameters in nanostructure La1−xBaxNi1−yCuyO3 catalysts used in the reforming of methane with CO2	2017	Journal of the Taiwan Institute of Chemical Engineers	10.1016/j.jtice.2017.02.013
85	Ayegba P.O., Abdulkadir M., Hernandez-Perez V., Lowndes I.S., Azzopardi B.J.	Applications of artificial neural network (ANN) method for performance prediction of the effect of a vertical 90° bend on an air–silicone oil flow	2017	Journal of the Taiwan Institute of Chemical Engineers	10.1016/j.jtice.2017.02.005
86	Prabhu A.A., Mandal B., Dasu V.V.	Medium optimization for high yield production of extracellular human interferon-γ from Pichia pastoris: A statistical optimization and neural network-based approach	2017	Korean Journal of Chemical Engineering	10.1007/s11814-016-0358-1
87	Amid S., Mesri Gundoshmian T.	Prediction of output energies for broiler production using linear regression, ANN (MLP, RBF), and ANFIS models	2017	Environmental Progress and Sustainable Energy	10.1002/ep.12448
88	Davoodi P., Ghoreishi S.M., Hedayati A.	Optimization of supercritical extraction of galegine from Galega officinalis L.: Neural network modeling and experimental optimization via response surface methodology	2017	Korean Journal of Chemical Engineering	10.1007/s11814-016-0304-2
89	Baghban A., Mohammadi A.H., Taleghani M.S.	Rigorous modeling of CO2 equilibrium absorption in ionic liquids	2017	International Journal of Greenhouse Gas Control	10.1016/j.ijggc.2016.12.009
90	Ghode T., Begum K.M.M.S., Desamala A.B., Narayanan A.	A Comparative Study of ANN and CFD Modelling for Pressure Drop Prediction in a Fluidized Bed with Internals	2017	Indian Chemical Engineer	10.1080/00194506.2015.1116962
91	Mahmoodi N.M., Hosseinabadi-Farahani Z., Chamani H.	Dye adsorption from single and binary systems using NiO-MnO2 nanocomposite and artificial neural network modeling	2017	Environmental Progress and Sustainable Energy	10.1002/ep.12452
92	Radovanović R.M., Jovičić M.C., Bera O.J., Pavličević J.M., Pilić B.M., Radičević R.Ž.	The use of artificial neural networks for mathematical modeling of the effect of composition and production conditions on the properties of PVC floor coverings [Primena veštačkih neuronskih mreža za matematičko modelovanje uticaja sastava i uslova proizvodnje na svojstva PVC podnih obloga]	2017	Hemijska Industrija	10.2298/HEMIND151015012R
93	Roy S., Manna S., Sengupta S., Ganguli A., Goswami S., Das P.	Comparative assessment on defluoridation of waste water using chemical and bio-reduced graphene oxide: Batch, thermodynamic, kinetics and optimization using response surface methodology and artificial neural network	2017	Process Safety and Environmental Protection	10.1016/j.psep.2017.07.010
94	Oladipo A.A., Gazi M.	Targeted boron removal from highly-saline and boron-spiked seawater using magnetic nanobeads: Chemometric optimisation and modelling studies	2017	Chemical Engineering Research and Design	10.1016/j.cherd.2017.03.024
95	Belkacem S., Bouafia S., Chabani M.	Study of oxytetracycline degradation by means of anodic oxidation process using platinized titanium (Ti/Pt) anode and modeling by artificial neural networks	2017	Process Safety and Environmental Protection	10.1016/j.psep.2017.07.007
96	Mondal S., Aikat K., Siddharth K., Sarkar K., DasChaudhury R., Mandal G., Halder G.	Optimizing ranitidine hydrochloride uptake of Parthenium hysterophorus derived N-biochar through response surface methodology and artificial neural network	2017	Process Safety and Environmental Protection	10.1016/j.psep.2017.03.011
97	Kojić P., Omorjan R.	Predicting hydrodynamic parameters and volumetric gas–liquid mass transfer coefficient in an external-loop airlift reactor by support vector regression	2017	Chemical Engineering Research and Design	10.1016/j.cherd.2017.07.029
98	Kadiyala A., Kumar A.	Vector Time Series-Based Radial Basis Function Neural Network Modeling of Air Quality Inside a Public Transportation Bus Using Available Software	2017	Environmental Progress and Sustainable Energy	10.1002/ep.12523
99	Parveen N., Zaidi S., Danish M.	Development of SVR-based model and comparative analysis with MLR and ANN models for predicting the sorption capacity of Cr(VI)	2017	Process Safety and Environmental Protection	10.1016/j.psep.2017.03.007
100	Biglarijoo N., Mirbagheri S.A., Bagheri M., Ehteshami M.	Assessment of effective parameters in landfill leachate treatment and optimization of the process using neural network, genetic algorithm and response surface methodology	2017	Process Safety and Environmental Protection	10.1016/j.psep.2016.12.006

Figure 8.6: Data from Figure 1.1 (continued).

	Authors	Title	Year	Source title	DOI
101	Azarpour A., N.G. Borhani T., R. Wan Alwi S., A. Manan Z., I. Abdul Mutalib M.	A generic hybrid model development for process analysis of industrial fixed-bed catalytic reactors	2017	Chemical Engineering Research and Design	10.1016/j.cherd.2016.10.024
102	Todorović Ž.N., Rajaković L.V., Onjia A.E.	Modelling of cations retention in ion chromatography with methanesulfonic acid as eluent [Modelovanje retencije katjona u jonskoj hromatografiji sa metansulfonskom kiselinom kao eluentom]	2017	Hemijska Industrija	10.2298/HEMIND151107014T
103	Baghban A., Sasanipour J., Haratipour P., Alizad M., Vafaee Ayouri M.	ANFIS modeling of rhamnolipid breakthrough curves on activated carbon	2017	Chemical Engineering Research and Design	10.1016/j.cherd.2017.08.007
104	Banerjee P., Barman S.R., Mukhopadhayay A., Das P.	Ultrasound assisted mixed azo dye adsorption by chitosan–graphene oxide nanocomposite	2017	Chemical Engineering Research and Design	10.1016/j.cherd.2016.10.009
105	Kamesh R., Rani K.Y.	Nonlinear control strategies based on Adaptive ANN models: Multi-product semi-batch polymerization reactor case study	2017	Chemical Engineering Research and Design	10.1016/j.cherd.2017.03.019
106	Dastkhoon M., Ghaedi M., Asfaram A., Ahmadi Azqhandi M.H., Purkait M.K.	Simultaneous removal of dyes onto nanowires adsorbent use of ultrasound assisted adsorption to clean waste water: Chemometrics for modeling and optimization, multicomponent adsorption and kinetic study	2017	Chemical Engineering Research and Design	10.1016/j.cherd.2017.06.011
107	Eryilmaz T., Arslan M., Yesilyurt M.K., Taner A.	Comparison of empirical equations and artificial neural network results in terms of kinematic viscosity prediction of fuels based on hazelnut oil methyl ester	2016	Environmental Progress and Sustainable Energy	10.1002/ep.12410
108	Agarwal H., Rathore A.S., Hadpe S.R., Alva S.J.	Artificial neural network (ANN)-based prediction of depth filter loading capacity for filter sizing	2016	Biotechnology Progress	10.1002/btpr.2329
109	Gomez-Gonzalez R., Cerino-Córdova F.J., Garcia-León A.M., Soto-Regalado E., Davila-Guzman N.E., Salazar-Rabago J.J.	Lead biosorption onto coffee grounds: Comparative analysis of several optimization techniques using equilibrium adsorption models and ANN	2016	Journal of the Taiwan Institute of Chemical Engineers	10.1016/j.jtice.2016.08.038
110	Carvajal F., Agüera F., Sánchez-Hermosilla J.	Estimating the evaporation from irrigation reservoirs of greenhouses using satellite imagery	2016	Environmental Progress and Sustainable Energy	10.1002/ep.12419
111	Li W., Wei S., Jiao W., Qi G., Liu Y.	Modelling of adsorption in rotating packed bed using artificial neural networks (ANN)	2016	Chemical Engineering Research and Design	10.1016/j.cherd.2016.08.013
112	Omidvarborna H., Kumar A., Kim D.S.	Artificial neural network prediction of NOx emissions from EGR and non-EGR engines running on soybean biodiesel fuel (B5) during cold idle mode	2016	Environmental Progress and Sustainable Energy	10.1002/ep.12376
113	Borhani T.N.G., Afzali A., Bagheri M.	QSPR estimation of the auto-ignition temperature for pure hydrocarbons	2016	Process Safety and Environmental Protection	10.1016/j.psep.2016.07.004
114	Elfghi F.M.	A hybrid statistical approach for modeling and optimization of RON: A comparative study and combined application of response surface methodology (RSM) and artificial neural network (ANN) based on design of experiment (DOE)	2016	Chemical Engineering Research and Design	10.1016/j.cherd.2016.05.023
115	von Stosch M., Hamelink J.-M., Oliveira R.	Toward intensifying design of experiments in upstream bioprocess development: An industrial Escherichia coli feasibility study	2016	Biotechnology Progress	10.1002/btpr.2295
116	Soriano A.N., Ornedo-Ramos K.F.P., Muriel C.A.M., Adornado A.P., Bungay V.C., Li M.-H.	Prediction of refractive index of binary solutions consisting of ionic liquids and alcohols (methanol or ethanol or 1-propanol) using artificial neural network	2016	Journal of the Taiwan Institute of Chemical Engineers	10.1016/j.jtice.2016.05.031
117	Bagheri A.R., Ghaedi M., Asfaram A., Hajati S., Ghaedi A.M., Bazrafshan A., Rahimi M.R.	Modeling and optimization of simultaneous removal of ternary dyes onto copper sulfide nanoparticles loaded on activated carbon using second-derivative spectrophotometry	2016	Journal of the Taiwan Institute of Chemical Engineers	10.1016/j.jtice.2016.05.004
118	Das P., Das P.	Graphene oxide for the treatment of ranitidine containing solution: Optimum sorption kinetics by linear and non linear methods and simulation using artificial neural network	2016	Process Safety and Environmental Protection	10.1016/j.psep.2016.05.018
119	Tak K., Kim J., Kwon H., Cho J.H., Moon I.	Kriging models for forecasting crude unit overhead corrosion	2016	Korean Journal of Chemical Engineering	10.1007/s11814-016-0083-9
120	Singh H., Raj V.B., Kumar J., Durani F., Mishra M., Nimal A.T., Sharma M.U.	SAW mono sensor for identification of harmful vapors using PCA and ANN	2016	Process Safety and Environmental Protection	10.1016/j.psep.2016.05.014

Figure 8.7: Data from Figure 1.1 (continued).

	Authors	Title	Year	Source title	DOI
121	Ahmad M.F., Haydar S.	Evaluation of a newly developed biosorbent using packed bed column for possible application in the treatment of industrial effluents for removal of cadmium ions	2016	Journal of the Taiwan Institute of Chemical Engineers	10.1016/j.jtice.2015.12.032
122	Podstawczyk D., Witek-Krowiak A.	Novel nanoparticles modified composite eco-adsorbents-A deep insight into kinetics modelling using numerical surface diffusion and artificial neural network models	2016	Chemical Engineering Research and Design	10.1016/j.cherd.2016.01.008
123	Ebrahimi S., Mollaiy-Berneti S., Asadi H., Peydayesh M., Akhlaghian F., Mohammadi T.	PVA/PES-amine-functional graphene oxide mixed matrix membranes for CO_2/CH_4 separation: Experimental and modeling	2016	Chemical Engineering Research and Design	10.1016/j.cherd.2016.03.009
124	Eswari J S., Chandrakar N.	Artificial neural networks as classification and diagnostic tools for lymph node-negative breast cancers	2016	Korean Journal of Chemical Engineering	10.1007/s11814-015-0255-z
125	Babaei A.A., Khataee A., Ahmadpour E., Sheydaei M., Kakavandi B., Alaee Z.	Optimization of cationic dye adsorption on activated spent tea: Equilibrium, kinetics, thermodynamic and artificial neural network modeling	2016	Korean Journal of Chemical Engineering	10.1007/s11814-014-0334-6
126	Soukht Saraee H., Jafarmadar S., Alizadeh-Haghighi E., Ashrafi S.J.	Experimental investigation of pollution and fuel consumption on a CI engine operated on alumina nanoparticles - Diesel fuel with the aid of artificial neural network	2016	Environmental Progress and Sustainable Energy	10.1002/ep.12233
127	Sodeifian G., Sajadian S.A., Saadati Ardestani N.	Evaluation of the response surface and hybrid artificial neural network-genetic algorithm methodologies to determine extraction yield of Ferulago angulata through supercritical fluid	2016	Journal of the Taiwan Institute of Chemical Engineers	10.1016/j.jtice.2015.11.003
128	Raja M.A.Z., Shah F.H., Khan A.A., Khan N.A.	Design of bio-inspired computational intelligence technique for solving steady thin film flow of Johnson-Segalman fluid on vertical cylinder for drainage problems	2016	Journal of the Taiwan Institute of Chemical Engineers	10.1016/j.jtice.2015.10.020
129	Tan P., Zhang C., Xia J., Fang Q., Chen G.	NOX emission model for coal-fired boilers using principle component analysis and support vector regression	2016	Journal of Chemical Engineering of Japan	10.1252/jcej.15we066
130	Dong S., Wang B., Wang Z., Hu X.-K., Song H.-C., Liu Q.	Comparison of prediction models for power draw in grinding and flotation processes in a gold treatment plant	2016	Journal of Chemical Engineering of Japan	10.1252/jcej.15we127
131	Dil E.A., Ghaedi M., Ghaedi A., Asfaram A., Jamshidi M., Purkait M.K.	Application of artificial neural network and response surface methodology for the removal of crystal violet by zinc oxide nanorods loaded on activate carbon: Kinetics and equilibrium study	2016	Journal of the Taiwan Institute of Chemical Engineers	10.1016/j.jtice.2015.07.023
132	Hadi N., Niaei A., Nabavi S.R., Alizadeh R., Shirazi M.N., Izadkhah B.	An intelligent approach to design and optimization of M-Mn/H-ZSM-(M: Ce, Cr, Fe, Ni) catalysts in conversion of methanol to propylene	2016	Journal of the Taiwan Institute of Chemical Engineers	10.1016/j.jtice.2015.09.017
133	Md Sarip M.S., Yamashita Y., Morad N.A., Che Yunus M.A., Abdul Aziz M.K.	Modeling and optimization of the hot compressed water extraction of palm oil using artificial neural network	2016	Journal of Chemical Engineering of Japan	10.1252/jcej.15we251
134	Torbati S.	Artificial neural network modeling of biotreatment of malachite green by Spirodela polyrhiza: Study of plant physiological responses and the dye biodegradation pathway	2016	Process Safety and Environmental Protection	10.1016/j.psep.2015.10.004
135	Tapan N.A., Günay M.E., Yildirim R.	Constructing global models from past publications to improve design and operating conditions for direct alcohol fuel cells	2016	Chemical Engineering Research and Design	10.1016/j.cherd.2015.11.018
136	Esfandyari M., Fanaei M.A., Gheshlaghi R., Mahdavi M.A.	Neural network and neuro-fuzzy modeling to investigate the power density and Columbic efficiency of microbial fuel cell	2016	Journal of the Taiwan Institute of Chemical Engineers	10.1016/j.jtice.2015.06.005
137	Brlek T.I., Pezo L.L., Voća N.M., Vukmirović Đ.M., Čolović R.R., Kiš D.E., Brkljača J.S.	The quality analyses of olive cake fuel pellets - Mathematical approach [Analiza kvaliteta agro-pelete dobijenih od pogače masline - Matematički pristup]	2016	Hemijska Industrija	10.2298/HEMIND140911008B
138	Kadiyala A., Kumar A.	Vector-time-series-based back propagation neural network modeling of air quality inside a public transportation bus using available software	2016	Environmental Progress and Sustainable Energy	10.1002/ep.12273
139	Dučić N., Ćojbašić Ž., Slavković R., Jordović B., Purenović J.	Optimization of chemical composition in the manufacturing process of flotation balls based on intelligent soft sensing [Optimizacija hemijskog sastava u proizvodnji flotacijskih kugli zasnovana na inteligentnoj softverskoj detekciji]	2016	Hemijska Industrija	10.2298/HEMIND150715068D
140	Fang Z., Liu X., Zhang M., Sun J., Mao S., Lu J., Rohani S.	A neural network approach to simulating the dynamic extraction process of l-phenylalanine from sodium chloride aqueous solutions by emulsion liquid membrane	2016	Chemical Engineering Research and Design	10.1016/j.cherd.2015.11.012

Figure 8.8: Data from Figure 1.1 (continued).

	Authors	Title	Year	Source title	DOI
141	Halali M.A., Azari V., Arabloo M., Mohammadi A.H., Bahadori A.	Application of a radial basis function neural network to estimate pressure gradient in water-oil pipelines	2016	Journal of the Taiwan Institute of Chemical Engineers	10.1016/j.jtice.2015.06.042
142	Mohagheghian E., Zafarian-Rigaki H., Motamedi-Ghahfarrokhi Y., Hemmati-Sarapardeh A.	Using an artificial neural network to predict carbon dioxide compressibility factor at high pressure and temperature	2015	Korean Journal of Chemical Engineering	10.1007/s11814-015-0025-y
143	Aghaeinejad-Meybodi A., Ebadi A., Shafiei S., Khataee A.R., Rostampour M.	Modeling and optimization of antidepressant drug Fluoxetine removal in aqueous media by ozone/H2O2 process: Comparison of central composite design and artificial neural network approaches	2015	Journal of the Taiwan Institute of Chemical Engineers	10.1016/j.jtice.2014.10.022
144	Mohammed M.L., Mbeleck R., Patel D., Niyogi D., Sherrington D.C., Saha B.	Greener and efficient epoxidation of 4-vinyl-1-cyclohexene with polystyrene 2-(aminomethyl)pyridine supported Mo(VI) catalyst in batch and continuous reactors	2015	Chemical Engineering Research and Design	10.1016/j.cherd.2014.08.001
145	Rahimi M., Hajialyani M., Beigzadeh R., Alsairafi A.A.	Application of artificial neural network and genetic algorithm approaches for prediction of flow characteristic in serpentine microchannels	2015	Chemical Engineering Research and Design	10.1016/j.cherd.2015.05.005
146	Mirbagheri S.A., Bagheri M., Bagheri Z., Kamarkhani A.M.	Evaluation and prediction of membrane fouling in a submerged membrane bioreactor with simultaneous upward and downward aeration using artificial neural network-genetic algorithm	2015	Process Safety and Environmental Protection	10.1016/j.psep.2015.03.015
147	Han I.-S., Shin H.K.	Modeling of a PEM fuel cell stack using partial least squares and artificial neural networks	2015	Korean Chemical Engineering Research	10.9713/kcer.2015.53.2.236
148	Chetehouna K., Tabach E.E., Bouazaoui L., Gascoin N.	Predicting the flame characteristics and rate of spread in fires propagating in a bed of Pinus pinaster using Artificial Neural Networks	2015	Process Safety and Environmental Protection	10.1016/j.psep.2015.06.010
149	Buenno L.H., Rocha J.C., Leme J., Caricati C.P., Tonso A., Fernández Núñez E.G.	Use of uniform designs in combination with neural networks for viral infection process development	2015	Biotechnology Progress	10.1002/btpr.2051
150	Gummadi J., Bhatt D., Adusumilli S., Devabhaktuni V., Acosta W., Kumar A.	Interpolation techniques for modeling and estimating indoor radon concentrations in Ohio: Comparative study	2015	Environmental Progress and Sustainable Energy	10.1002/ep.11937
151	Raja M.A.Z., Khan J.A., Haroon T.	Stochastic numerical treatment for thin film flow of third grade fluid using unsupervised neural networks	2015	Journal of the Taiwan Institute of Chemical Engineers	10.1016/j.jtice.2014.10.018
152	Ramazanpour Esfahani A., Hojati S., Azimi A., Farzadian M., Khataee A.	Enhanced hexavalent chromium removal from aqueous solution using a sepiolite-stabilized zero-valent iron nanocomposite: Impact of operational parameters and artificial neural network modeling	2015	Journal of the Taiwan Institute of Chemical Engineers	10.1016/j.jtice.2014.11.011
153	Hasanlou H., Abdolabadi H., Aghashahi M.	Application of factor analysis in a large-scale industrial wastewater treatment plant simulation using principal component analysis-artificial neural network hybrid approach: (Case Study: Fajr Industrial Wastewater Treatment Plant, Mahshahr, Iran)	2015	Environmental Progress and Sustainable Energy	10.1002/ep.12120
154	Saberivahidaval M., Hajjam S.	Comparison between performances of different neural networks for wind speed forecasting in Payam airport, Iran	2015	Environmental Progress and Sustainable Energy	10.1002/ep.12081
155	Halder G., Dhawane S., Barai P.K., Das A.	Optimizing chromium (VI) adsorption onto superheated steam activated granular carbon through response surface methodology and artificial neural network	2015	Environmental Progress and Sustainable Energy	10.1002/ep.12028
156	Wadi Abbas Al-Fatlawi A., Rahim N.A., Saidur R., Ward T.A.	Improving solar energy prediction in complex topography using artificial neural networks: Case study Peninsular Malaysia	2015	Environmental Progress and Sustainable Energy	10.1002/ep.12130
157	Kadiyala A., Kumar A.	Multivariate time series based back propagation neural network modeling of air quality inside a public transportation bus using available software	2015	Environmental Progress and Sustainable Energy	10.1002/ep.12199
158	Taheri M., Moghaddam M.R.A., Arami M.	Improvement of the /Taguchi/ design optimization using artificial intelligence in three acid azo dyes removal by electrocoagulation	2015	Environmental Progress and Sustainable Energy	10.1002/ep.12145
159	Bagheri M., Mirbagheri S.A., Ehteshami M., Bagheri Z.	Modeling of a sequencing batch reactor treating municipal wastewater using multi-layer perceptron and radial basis function artificial neural networks	2015	Process Safety and Environmental Protection	10.1016/j.psep.2014.04.006
160	Abbasi M., Soleymani A.R., Parsa J.B.	Degradation of Rhodamine B by an electrochemical ozone generating system consist of a Ti anode coated with nanocomposite of Sn-Sb-Ni oxide	2015	Process Safety and Environmental Protection	10.1016/j.psep.2015.01.007

Figure 8.9: Data from Figure 1.1 (continued).

	Authors	Title	Year	Source title	DOI
161	Nadian M.H., Rafiee S., Aghbashlo M., Hosseinpour S., Mohtasebi S.S.	Continuous real-time monitoring and neural network modeling of apple slices color changes during hot air drying	2015	Food and Bioproducts Processing	10.1016/j.fbp.2014.03.005
162	Ghaedi M., Ansari A., Nejad P.A., Ghaedi A., Vafaei A., Habibi M.H.	Artificial neural network and bees algorithm for removal of eosin b using cobalt oxide nanoparticle-activated carbon: Isotherm and kinetics study	2015	Environmental Progress and Sustainable Energy	10.1002/ep.11981
163	Albahri T.A.	MNLR and ANN structural group contribution methods for predicting the flash point temperature of pure compounds in the transportation fuels range	2015	Process Safety and Environmental Protection	10.1016/j.psep.2014.03.005
164	Mathew R.K., Aravind D., Begum K.M.M.S., Narayanan A.	Studies on Fluidized Beds Using Disc-type Internals and Modelling by ANN	2015	Indian Chemical Engineer	10.1080/00194506.2014.975759
165	Kamari A., Bahadori A., Mohammadi A.H.	On the determination of crude oil salt content: Application of robust modeling approaches	2015	Journal of the Taiwan Institute of Chemical Engineers	10.1016/j.jtice.2015.03.031
166	Mandal S., Mahapatra S.S., Sahu M.K., Patel R.K.	Artificial neural network modelling of As(III) removal from water by novel hybrid material	2015	Process Safety and Environmental Protection	10.1016/j.psep.2014.02.016
167	Kadiyala A., Kumar A.	Univariate time series based back propagation neural network modeling of air quality inside a public transportation bus using available software	2015	Environmental Progress and Sustainable Energy	10.1002/ep.12119
168	Ziaee H., Hosseini S.M., Sharafpoor A., Fazavi M., Ghiasi M.M., Bahadori A.	Prediction of solubility of carbon dioxide in different polymers using support vector machine algorithm	2015	Journal of the Taiwan Institute of Chemical Engineers	10.1016/j.jtice.2014.09.015
169	Kundu P., Paul V., Kumar V., Mishra I.M.	Formulation development, modeling and optimization of emulsification process using evolving RSM coupled hybrid ANN-GA framework	2015	Chemical Engineering Research and Design	10.1016/j.cherd.2015.10.025
170	Talwar S., Verma A.K., Sangal V.K.	Modeling and optimization of fixed mode dual effect (photocatalysis and photo-Fenton) assisted Metronidazole degradation using ANN coupled with genetic algorithm	2019	Journal of Environmental Management	10.1016/j.jenvman.2019.109428
171	Taherkhani S., Karimi H., Mohammadi F., Darvishmotevalli M., Bina B.	Investigation of photocatalytic activity of synthesized zinc stannate for tetracycline antibiotic degradation: Modelling and optimization through RSM, ANN and genetic algorithm	2019	Desalination and Water Treatment	10.5004/dwt.2019.24661
172	Boumahdi M., El Amrani C., Denys S.	An innovative air purification method and neural network algorithm applied to urban streets	2019	International Journal of Embedded and Real-Time Communication Systems	10.4018/IJERTCS.2019100101
173	Leila Airemlou, Behnajady M.A., Mahanpoor K.	Photocatalytic Removal of RhB by Ag and Mg Co-Doped ZnO Nanoparticles: Modeling of Operational Parameters Using ANN Based on RSM Data	2019	Russian Journal of Physical Chemistry A	10.1134/S0036024419090097
174	Aquino R.V.S., Barbosa A.A., Carvalho R.F., Silva M.G., Nascimento Júnior W.J.D., Silva T.D.D., Silva J.P., Rossiter Sá da Rocha O.	Degradation study of tris(2-butoxyethyl) phosphate with TiO2 immobilized on aluminum meshes employing artificial neural networks	2019	Water science and technology : a journal of the International Association on Water Pollution Research	10.2166/wst.2019.363
175	Mohsenzadeh M., Ahmad Mirbagheri S., Samadsabbaghi S.	Immobilized Pani-Tio2 Nano-Photocatalyst Modeling For Photocatalytic Degradation Of 1, 2-Dichloroethane Using Response Surface Methodology (Rsm) and Artificial Neural Network (Ann)	2019	International Journal of Mechanical and Production Engineering Research and Development	10.24247/ijmperdaug201973
176	Jamali Alyani S., Ebrahimian Pirbazari A., Esmaeili Khalilsaraei F., Asasian Kolur N., Gilani N.	Growing Co-doped TiO2 nanosheets on reduced graphene oxide for efficient photocatalytic removal of tetracycline antibiotic from aqueous solution and modeling the process by artificial neural network	2019	Journal of Alloys and Compounds	10.1016/j.jallcom.2019.05.175
177	Barbosa A.A., de Aquino R.V.S., da Cruz Santana Neves N.S., Dantas R.F., Duarte M.M.M.B., da Rocha O.R.S.	Kinetic study of dye removal using TiO2 supported on polyethylene terephthalate by advanced oxidation processes through neural networks	2019	Water Science and Technology	10.2166/wst.2019.111
178	Kalantary R.R., Moradi M., Pirsaheb M., Esrafili A., Jafari A.J., Gholami M., Vasseghian Y., Antolini E., Dragoi E.-N.	Enhanced photocatalytic inactivation of E. coli by natural pyrite in presence of citrate and EDTA as effective chelating agents: Experimental evaluation and kinetic and ANN models	2019	Journal of Environmental Chemical Engineering	10.1016/j.jece.2019.102906
179	[No author name available]	2nd International Conference on Sensors, Materials and Manufacturing, ICSMM 2018, International Conference on Materials Sciences and Nanomaterials, ICMSN 2018 and the 2nd International Conference on Materials and Intelligent Manufacturing, ICMIM 2018	2019	Materials Science Forum	
180	Talwar S., Sangal V.K., Verma A., Kaur P., Garg A.	Modeling, Optimization and Kinetic Study for Photocatalytic Treatment of Ornidazole Using Slurry and Fixed-Bed Approach	2018	Arabian Journal for Science and Engineering	10.1007/s13369-018-3388-7

Figure 8.10: Data from Figure 1.1 (continued).

	Authors	Title	Year	Source title	DOI
181	Hassani A., Khataee A., Fathinia M., Karaca S.	Photocatalytic ozonation of ciprofloxacin from aqueous solution using TiO2/MMT nanocomposite: Nonlinear modeling and optimization of the process via artificial neural network integrated genetic algorithm	2018	Process Safety and Environmental Protection	10.1016/j.psep.2018.03.013
182	Abdollahi Y., Sabbaghi S., Abouzari-Lotf E., Jahangirian H., Sairi N.A.	A new achievement in green degradation of aqueous organic pollutants under visible-light irradiation	2018	Water Science and Technology	10.2166/wst.2018.017
183	Bararpour S.T., Feylizadeh M.R., Delparish A., Qanbarzadeh M., Raeiszadeh M., Feilizadeh M.	Investigation of 2-nitrophenol solar degradation in the simultaneous presence of K2S2O8 and H2O2: Using experimental design and artificial neural network	2018	Journal of Cleaner Production	10.1016/j.jclepro.2017.11.191
184	Nascimento Júnior W.J.D., da Rocha O.R.S., Dantas R.F., da Silva J.P., Barbosa A.A.	Kinetic study of food dyes removal from aqueous solutions by solar heterogeneous photocatalysis with artificial neural networks and phytotoxicity assessment	2018	Desalination and Water Treatment	10.5004/dwt.2018.21841
185	Oladipo A.A., Vaziri R., Abureesh M.A.	Highly robust AgIO3/MIL-53 (Fe) nanohybrid composites for degradation of organophosphorus pesticides in single and binary systems: Application of artificial neural networks modelling	2018	Journal of the Taiwan Institute of Chemical Engineers	10.1016/j.jtice.2017.12.013
186	Jasso-Salcedo A.B., Hoppe S., Pla F., Escobar-Barrios V.A., Camargo M., Meimaroglou D.	Modeling and optimization of a photocatalytic process: Degradation of endocrine disruptor compounds by Ag/ZnO	2017	Chemical Engineering Research and Design	10.1016/j.cherd.2017.10.012
187	Seyed Dorraji M.S., Amani-Ghadim A.R., Rasoulifard M.H., Daneshvar H., Sistani Zadeh Aghdam B., Tarighati A.R., Hosseini S.F.	Photocatalytic activity of g-C3N4: An empirical kinetic model, optimization by neuro-genetic approach and identification of intermediates	2017	Chemical Engineering Research and Design	10.1016/j.cherd.2017.09.012
188	Ahmadpour A., Haghighi Asl A., Fallah N.	Synthesis and comparison of spent caustic wastewater photocatalytic treatment efficiency with zinc oxide composite	2017	Desalination and Water Treatment	10.5004/dwt.2017.21501
189	Sebti A., Souahi F., Mohellebi F., Igoud S.	Experimental study and artificial neural network modeling of tartrazine removal by photocatalytic process under solar light	2017	Water Science and Technology	10.2166/wst.2017.201
190	Dhiman N., Markandeya, Singh A., Verma N.K., Ajaria N., Patnaik S.	Statistical optimization and artificial neural network modeling for acridine orange dye degradation using in-situ synthesized polymer capped ZnO nanoparticles	2017	Journal of Colloid and Interface Science	10.1016/j.jcis.2017.01.042
191	Garg A., Sangal V.K., Bajpai P.K.	Photocatalytic Treatment of Binary Mixture of Dyes using UV/TiO2 Process: Calibration, Modeling, Optimization and Mineralization Study	2017	International Journal of Chemical Reactor Engineering	10.1515/ijcre-2015-0220
192	Rahmani E., Jafari D., Rahmani H., Kazemi F.	Prediction of photocatalytic activity of TiO2 thin films doped by SiO2 using artificial neural network and fuzzy model approach	2017	Recent Innovations in Chemical Engineering	10.2174/2405520410666170614111639
193	Expósito A.J., Monteagudo J.M., Durán A., Fernández A.	Dynamic behavior of hydroxyl radical in sono-photo-Fenton mineralization of synthetic municipal wastewater effluent containing antipyrine	2017	Ultrasonics Sonochemistry	10.1016/j.ultsonch.2016.09.017
194	Expósito A.J., Patterson D.A., Mansor W.S.W., Monteagudo J.M., Emanuelsson E., Sanmartin I., Durán A.	Antipyrine removal by TiO2 photocatalysis based on spinning disc reactor technology	2017	Journal of Environmental Management	10.1016/j.jenvman.2016.11.012
195	Estahbanati M.R.K., Feilizadeh M., Iliuta M.C.	Photocatalytic valorization of glycerol to hydrogen: Optimization of operating parameters by artificial neural network	2017	Applied Catalysis B: Environmental	10.1016/j.apcatb.2017.03.016
196	Özbay B., Genç N., Özbay İ., Bağhaki B., Zor S.	Photocatalytic activities of polyaniline-modified TiO2 and ZnO under visible light: an experimental and modeling study	2016	Clean Technologies and Environmental Policy	10.1007/s10098-016-1174-3
197	Salehi K., Daraei H., Teymouri P., Shahmoradi B., Maleki A.	Cu-doped ZnO nanoparticle for removal of reactive black 5: application of artificial neural networks and multiple linear regression for modeling and optimization	2016	Desalination and Water Treatment	10.1080/19443994.2015.1130658
198	Oladipo A.A., Abureesh M.A., Gazi M.	Bifunctional composite from spent "Cyprus coffee" for tetracycline removal and phenol degradation: Solar-Fenton process and artificial neural network	2016	International Journal of Biological Macromolecules	10.1016/j.ijbiomac.2015.08.054
199	Bennemla M., Chabani M., Amrane A.	Photocatalytic Degradation of Oxytetracycline in Aqueous Solutions with TiO2 in Suspension and Prediction by Artificial Neural Networks	2016	International Journal of Chemical Kinetics	10.1002/kin.21005
200	Eskandarloo H., Badiei A., Behnajady M.A., Mohammadi Ziarani G.	Hybrid Homogeneous and Heterogeneous Photocatalytic Processes for Removal of Triphenylmethane Dyes: Artificial Neural Network Modeling	2016	Clean - Soil, Air, Water	10.1002/clen.201400449

Figure 8.11: Data from Figure 1.1 (continued).

	Authors	Title	Year	Source title	DOI
201	Lenzi G.G., Evangelista R.F., Duarte E.R., Colpini L.M.S., Fornari A.C., Menechini Neto R., Jorge L.M.M., Santos O.A.A.	Photocatalytic degradation of textile reactive dye using artificial neural network modeling approach	2016	Desalination and Water Treatment	10.1080/19443994.2015.1064035
202	Fathinia M., Khataee A., Aber S., Naseri A.	Development of kinetic models for photocatalytic ozonation of phenazopyridine on TiO2 nanoparticles thin film in a mixed semi-batch photoreactor	2016	Applied Catalysis B: Environmental	10.1016/j.apcatb.2015.11.033
203	Shargh M., Behnajady M.A.	A high-efficient batch-recirculated photoreactor packed with immobilized TiO2-P25 nanoparticles onto glass beads for photocatalytic degradation of phenazopyridine as a pharmaceutical contaminant: Artificial neural network modeling	2016	Water Science and Technology	10.2166/wst.2016.132
204	Rasoulifard M.H., Seyed Dorraji M.S., Amani-Ghadim A.R., Keshavarz-Babaeinezhad N.	Visible-light photocatalytic activity of chitosan/polyaniline/CdS nanocomposite: Kinetic studies and artificial neural network modeling	2016	Applied Catalysis A: General	10.1016/j.apcata.2016.01.002
205	Garg A., Sangal V.K., Bajpai P.K.	Decolorization and degradation of Reactive Black 5 dye by photocatalysis: modeling, optimization and kinetic study	2016	Desalination and Water Treatment	10.1080/19443994.2015.1086697
206	Hassani A., Khataee A., Karaca S.	Photocatalytic degradation of ciprofloxacin by synthesized TiO2 nanoparticles on montmorillonite: Effect of operation parameters and artificial neural network modeling	2015	Journal of Molecular Catalysis A: Chemical	10.1016/j.molcata.2015.08.020
207	Behnajady M.A., Eskandarloo H., Eskandarloo F.	Artificial neural network modeling of the influence of sol-gel synthesis variables on the photocatalytic activity of TiO2 nanoparticles in the removal of Acid Red 27	2015	Research on Chemical Intermediates	10.1007/s11164-014-1753-z
208	David C., Arivazhagan M., Ibrahim M.	Spent wash decolourization using nano-Al2O3/kaolin photocatalyst: Taguchi and ANN approach	2015	Journal of Saudi Chemical Society	10.1016/j.jscs.2015.05.012
209	González-Campos G., Torres-Treviño L.M., Luévano-Hipólito E., Martinez-De La Cruz A.	Modeling synthesis processes of photocatalysts using symbolic regression α-β	2015	Proceedings of Special Session 2014 13th Mexican International Conference on Artificial Intelligence: Advances in Artificial Intelligence, MICAI 2014	10.1109/MICAI.2014.33
210	Kıranşan M., Khataee A., Karaca S., Sheydaei M.	Artificial neural network modeling of photocatalytic removal of a disperse dye using synthesized of ZnO nanoparticles on montmorillonite	2015	Spectrochimica Acta - Part A: Molecular and Biomolecular Spectroscopy	10.1016/j.saa.2014.12.100
211	Delnavaz M.	Application of artificial neural networks for prediction of photocatalytic reactor	2015	Water Environment Research	10.2175/WERD1400430.1
212	Amani-Ghadim A.R., Dorraji M.S.S.	Modeling of photocatalyatic process on synthesized ZnO nanoparticles: Kinetic model development and artificial neural networks	2015	Applied Catalysis B: Environmental	10.1016/j.apcatb.2014.08.020
213	Sabonian M., Behnajady M.A.	Artificial neural network modeling of Cr(VI) photocatalytic reduction with TiO2-P25 nanoparticles using the results obtained from response surface methodology optimization	2015	Desalination and Water Treatment	10.1080/19443994.2014.963161
214	Behnajady M.A., Eskandarloo H.	Preparation of TiO2 nanoparticles by the sol-gel method under different pH conditions and modeling of photocatalytic activity by artificial neural network	2015	Research on Chemical Intermediates	10.1007/s11164-013-1327-5
215	Vaez M., Omidkhah M., Alijani S., Zarringhalam Moghaddam A., Sadrameli M., Gholipour Zanjani N.	Evaluation of photocatalytic activity of immobilized titania nanoparticles by support vector machine and artificial neural network	2015	Canadian Journal of Chemical Engineering	10.1002/cjce.22171
216	Kıranşan M., Khataee A., Karaca S., Sheydaei M.	Synthesis of zinc oxide nanoparticles on montmorillonite for photocatalytic degradation of basic yellow 28: Effect of parameters and neural network modeling	2015	Current Nanoscience	10.2174/1573413711666150218002259
217	Mitschker J., Klüner T.	Adsorption and electronic excitation of water on TiO2 (110): Calculation of high-dimensional potential energy surfaces	2015	High Performance Computing in Science and Engineering '14: Transactions of the High Performance Computing Center, Stuttgart (HLRS) 2014	10.1007/978-3-319-10810-0_14
218	Diamanti M.V., Ormellese M., Pedeferri M.	Application-wise nanostructuring of anodic films on titanium: a review	2015	Journal of Experimental Nanoscience	10.1080/17458080.2014.999261

Figure 8.12: Data from Figure 1.1 (continued).

```
1    clear all; clc;
2
3    %ANN settings
4
5    hidden_layer_neurons = [4 6 8]; %Number of hidden neurons in the first layer
6    hln_size = size(hidden_layer_neurons,2);
7
8    hidden_layer_neurons_2 = [4 6 8]; %Number of hidden neurons in the second layer
9    hln_size_2 = size(hidden_layer_neurons_2,2);
10
11   hidden_layer_neurons_3 = [4 6 8]; %Number of hidden neurons in the third layer
12   hln_size_3 = size(hidden_layer_neurons_3,2);
13
14   hidden_layer_activ_func = ["tansig" "logsig"]; %Transfer functions
15   hlaf_size = size(hidden_layer_activ_func,2);
16
17   output_layer_neurons = 1; %Number of hidden neurons in the output layer
18   output_layer_activ_func = ["tansig" "purelin"]; %Output transfer functions
19   outf_size = size(output_layer_activ_func,2);
20
21   training_algorithms = ["trainlm" "trainoss" "trainbr"]; %Training algorithm
22   ta_size = size(training_algorithms,2);
23
24
25   %Data identification: Group
26   array = "BlockB_GroupSIII";
27
28   M = load('training_data.dat'); M = M';
29   N = load('test_data.dat'); N = N';
30
31   entrada = M(1:4,:);
32   saida = M(5,:);
33   in = N(1:4,:);
34   out = N(5,:);
35
36   for i = 1:ta_size           %For each training algorithm
37    for j1 = 1:hlaf_size       %For each activation function layer 1
38     for j2 = 1:hlaf_size      %For each activation function layer 2
39      for j3 = 1:hlaf_size     %For each activation function layer 3
40       for w = 1:outf_size     %For each output function
41        for k = 1:hln_size     %For each hiden layer 1 topology
42         for z1 = 1:hln_size_2 %For each hiden layer 2 topology
43          for z2 = 1:hln_size_3 %For each hiden layer 3 topology
44
45             setdemorandstream(4); %seed
46
47             %------------------ ANN TRAINING ------------------%
48             [entradan,minentrada,maxentrada,saidan,minsaida,maxsaida]=premnmx(entrada,saida);
49             %ANN type
50             net = newcf(minmax(entradan(:,:)),[hidden_layer_neurons(k),hidden_layer_neurons_2(z1),
51                 hidden_layer_neurons_3(z2),output_layer_neurons],{hidden_layer_activ_func(j1),
52                 hidden_layer_activ_func(j2),hidden_layer_activ_func(j3),output_layer_activ_func(w)},
53                 training_algorithms(i));
54
55             net.trainParam.epochs = 3000;   %steps
56             net.trainParam.goal = 1e-4;     %convergence
57             net.performFcn = 'sse';         %objective function
58             net.trainParam.min_grad = 1e-4; %gradient
59             net = init(net);
60             [net,tr] = train(net,entradan(:,:),saidan(:,:));
61             Y = sim(net,entradan(:,:));     %compare with input
62             X = postmnmx(Y,minsaida,maxsaida);
```

Figure 8.13: Matlab code implementation for ANN development.

```matlab
63
64                  %----- Figure -----%
65                  fig1 = figure(1);
66                  [m,b,r]=postreg(X(1,:),saida(1,:));
67                  fig2 = figure(2)
68                  s1=subplot(2,3,1);
69                  copyobj(allchild(get(fig1,'CurrentAxes')),s1);
70                  title(get(get(get(fig1,'CurrentAxes'),'title'),'String'))
71                  xlabel(get(get(get(fig1,'CurrentAxes'),'xlabel'),'String'))
72                  ylabel(get(get(get(fig1,'CurrentAxes'),'ylabel'),'String'))
73                  legend(get(get(get(fig1,'CurrentAxes'),'legend'),'String'),'Location','northwest')
74                  close(figure(1))
75                  subplot(2,3,[2 3]);
76                  plot(saida(1,:),'or')
77                  hold on
78                  plot(X(1,:),'-k');
79                  xlabel('Sample','FontSize',16);
80                  ylabel('Brand','FontSize',16);
81                  legend('Band gap observed','Band gap predicted','Location','southeast');
82                  title('Trainning')
83                  hold off
84
85                  %----- Saving the network -----%
86                  network_name = array + '_'+hidden_layer_activ_func(j1)+'_'+hidden_layer_neurons(k)+
87                              '_'+hidden_layer_activ_func(j2)+'_'+hidden_layer_neurons_2(z1)+'_'+
88                              hidden_layer_activ_func(j3)+'_'+hidden_layer_neurons_3(z2)+'_'+
89                              output_layer_activ_func(w)+'_'+output_layer_neurons;
90                  save ('ANNs/'+network_name,'net');
91
92                  %----------------- ANN TEST -----------------%
93                  [inn] = tramnmx(in,minentrada,maxentrada);
94                  Yt = sim(net,inn(:,:));
95                  Xt = postmnmx(Yt,minsaida,maxsaida);
96
97                  %----- Figure (cont) -----%
98                  figure(2)
99                  subplot(2,3,[5 6]);
100                 plot(out(1,:),'or')
101                 hold on
102                 plot(Xt(1,:),'-k');
103                 xlabel('Sample','FontSize',15);
104                 ylabel('Brand','FontSize',15);
105                 legend('observed','predicted','Location','southeast');
106                 colordef white;
107                 title('Test')
108                 hold off
109                 fig3 = figure(3);
110                 [a,z,f]=postreg(Xt(1,:),out(1,:));
111                 figure(2)
112                 s2=subplot(2,3,4);
113                 copyobj(allchild(get(fig3,'CurrentAxes')),s2);
114                 title(get(get(get(fig3,'CurrentAxes'),'title'),'String'))
115                 xlabel(get(get(get(fig3,'CurrentAxes'),'xlabel'),'String'))
116                 ylabel(get(get(get(fig3,'CurrentAxes'),'ylabel'),'String'))
117                 legend(get(get(get(fig3,'CurrentAxes'),'legend'),'String'),'Location','northwest')
118                 close(figure(3))
119
120                 %----------------- Saving the Figure -----------------%
121                 fig2_name = network_name;
122                 saveas(fig2,fullfile('Results/',fig2_name),'fig');
123                 close(fig2);
124
125                 %----------------- ANN TEST -----------------%
126                 results_name = 'Results/Results_Group'+network_name;
127                 hidden_weights = net.IW{1};
128                 output_weights = net.LW{2};
129                 hidden_bias = net.b{1};
130                 output_bias = net.b{2};
131                 perf_SSE = tr.best_perf;
132
133                 r2train = r^2;
134                 r2test = f^2;
135
136                 save(results_name,'perf_SSE','hidden_weights','output_weights','hidden_bias',
137                     'output_bias','r2train','r2test');
138
139         end
140       end
141      end
142    end
143   end
144  end
145 end
146 end
```

Figure 8.14: Matlab code implementation for ANN development (continued).

```
ans =

  3.4717 -10.9524   0.8855  -3.7521
 -3.7658  -0.8183  -1.4573   1.8097
 -3.0654 -13.3769  -1.7112  -2.8289
 -2.4070  -4.4112   0.3502  -4.7944
  1.0441   1.7771  -0.4585   1.6033
  4.4503   4.9527   1.8967  -1.4289
 -2.4709   4.2012  -0.6420   2.0861


ans =

  4.6567 -53.8991  -6.6189   7.6299  36.0942 -35.5902  25.83▶


ans =

                                      -13.2907
                                        3.6274
                                       -9.3527
                                       -2.0751
                                       -0.5892
                                       -0.3771
                                        6.877


ans =

                                       32.1892
```

Figure 8.15: Weights and Biases of Block A with the smallest database ANN-FF 4-7-1.